TRANSACTIONS
OF THE ASME
Series A

Journal of ENGINEERING FOR POWER

January 1960

Divisions: POWER • GAS TURBINE POWER • NUCLEAR ENGINEERING • FUELS OIL AND GAS POWER • **Research Committees:** FURNACE PERFORMANCE FACTORS CORROSION AND DEPOSITS FROM COMBUSTION GASES • BOILER FEEDWATER STUDIES • HIGH TEMPERATURE STEAM GENERATION • CONDENSER TUBES PROPERTIES OF STEAM • **Committees on:** AIR POLLUTION CONTROLS • SOLAR ENERGY APPLICATION • **And:** POWER TEST CODES COMMITTEES

Published Quarterly by
THE AMERICAN SOCIETY OF MECHANICAL ENGINEERS

TRANSACTIONS OF THE ASME
Series A

EDITORIAL DEPARTMENT

Editor, J. J. HARLITSCH, JR.
Consulting Editor, LEO BLOGGETT
Production, JEAN NORTH
Art Editor, PERRY BALFOUR

OFFICERS OF THE ASME

President, W. L. EISLER
Secretary, O. B. SCHIER, II
Treasurer, E. J. KATES
Assistant Treasurer, H. J. SAUER

PUBLICATIONS COMMITTEE

Chairman, B. G. A. SKROTZKI
HENDLEY W. BLACKMON
R. D. MINDLIN
MARTIN GOLAND
VITO L. SALERNO
Junior Representatives
A. S. GOLDSTEIN
J. W. FOLLANSBEE

REGIONAL ADVISORY BOARD

Region I, ROY L. PARSELL
Region II, GLENN R. FRYLING
Region III, F. I. HEINGE
Region IV, FRANCIS C. SMITH
Region V, M. M. CAYMER
Region VI, C. R. EARLE
Region VII, M. S. UNSENHAUER
Region VIII, LIMB MELANDER

Published quarterly by The American Society of Mechanical Engineers. Publication office at 20th and Northampton Streets, Easton, Pa. The editorial department is located at the headquarters of the Society, 29 West Thirty-Ninth Street, New York 18, N. Y. Cable address, "Mechanize," New York. Price $3.00 a copy, $10.00 annually; to members, $1.50 a copy, $5.00 annually. Add 50 cents for postage to all countries outside the United States and Canada. Changes of address must be received at Society headquarters seven weeks before they are to be effective on the mailing list. Please send old as well as new address. . . . By-Law: The Society shall not be responsible for statements or opinions advanced in papers or . . . printed in its publications (B13, Par. 4). . . . Second-class mail privileges authorized at Easton, Penna. This publication is authorized to be mailed at the special rates of postage prescribed by Section 132.122. . . . © Copyright, 1960, by The American Society of Mechanical Engineers. Reprints from this publication may be made on condition that full credit be given the Transactions of the ASME, Series A—Journal of Engineering for Power, and the author, and that date of publication be stated.

TRANSACTIONS OF THE ASME
is indexed by the Engineering Index, Inc.

Journal of
ENGINEERING FOR POWER

VOLUME 82 • SERIES A • NUMBER 1

January 1960

CONTENTS

1 **Development of a Three-Stage Liquid-Cooled Gas Turbine**
Sumner Alpert, R. E. Grey, and W. O. Flaschar

10 **Effect of Ambient and Fuel Pressure on Spray Drop Size**
S. M. DeCorso

19 **Presentation of a Blade-Design Method for Axial-Flow Turbines, Including Design and Test Results of a Typical Axial-Flow Stage**
F. Baumgartner and R. Amsler

27 **The Basic Heat Transfer and Flow Friction Characteristics of Six Compact High-Performance Heat Transfer Surfaces**
W. M. Kays

35 **Metallurgical Evaluation of Superheater-Tube Alloys After Six-Months' Exposure at Temperatures of 1100 to 1500 F**
C. L. Clark, J. J. B. Rutherford, A. B. Wilder, and M. A. Cordovi

68 **Blast-Furnace-Gas Cleaning for Iron and Ferromanganese Production**
J. S. Mackay and J. F. Kearns

73 **Influence Coefficients for Open-Crown Hemispheres**
G. D. Galletly

TRANSACTIONS
Series D

Journal of
BASIC ENGINEERING
Vol. 81 • Series D • No. 4

CONTENTS FOR DECEMBER, 1959

433 Applications of Computer and Model Studies to Problems Involving Hydraulic Transients, by I. W. McCaig and F. H. Jonker. (58—A-101)

446 Large Water-Level Displacements in the Simple Surge Tank, by A. W. Morris. (58—A-29)

455 Experience in the Use of the Gibson Method of Water Measurement for Efficiency Tests of Hydraulic Turbines, by N. R. Gibson. (58—A-78)

488 Free Discharge Through a Turbine Distributor, Case, and Draft Tube, by R. A. Sutherland. (58—A-76)

493 Symposium on Welded Spiral Cases From the Manufacturer's Viewpoint. (58—A-60)

505 Dériaz Type Reversible Pump-Turbine Installation at Sir Adam Beck-Niagara Forebay Pumped Storage Project, by A. E. Aeberli. (58—A-77)

521 Reversible Pump-Turbines for Sir Adam Beck-Niagara Pumping-Generator Station, by P. Dériaz and J. G. Warnock. (58—A-108)

534 Some Hydraulic Features of Puntledge Generating Plant, by A. W. Lash and R. E. Passmore. (58—A-100)

543 Application of Boundary-Layer Theory in Turbomachinery, by H. Schlichting.

552 Radial Equilibrium in Supersonic Compressors, by A. G. Hammitt and S. M. Bogdonoff. (58—A-110)

559 Résumé of the Supersonic-Compressor Research at NACA Lewis Laboratory, by W. W. Wilcox, R. R. Tysl, and M. J. Hartmann. (58—A-177)

569 Application and Analysis of a Computer Control System, by Irving Lefkowitz and D. P. Eckman. (58—A-281)

578 The Response of Pneumatic Transmission Lines to Step Inputs, by C. B. Schuder and R. C. Binder. (58—A-136)

585 A General Approach to the Practical Solution of Creep Problems, by A. Mendelson, M. H. Hirschberg, and S. S. Manson. (58—A-98)

599 Multiaxial Creep Studies on Inconel at 1500 F, by C. R. Kennedy, W. O. Harms, and D. A. Douglas. (58—A-193)

610 Creep-Rupture Strength of Austenitic Cr-Ni-Mo Steels in Sheet and Bar Form, by G. V. Smith, F. Garofalo, R. W. Whitmore, and R. R. Burt. (58—A-102)

617 Correlation of High Temperature Creep and Rupture Data, by Hans Conrad. (58—A-96)

629 Comparison of Parameter Methods for Extrapolating High-Temperature Data, by R. M. Goldhoff. (58—A-121)

645 Tests on Deflection of Flat Oval Bourdon Tubes, by G. Kardos. (58—A-67)

651 Bending and Stretching of Corrugated Diaphragms, by R. F. Dressler. (58—A-62)

660 Electromagnetic Flowmeter Primary Elements, by V. P. Head. (58—A-126)

669 The Distribution of Contact Pressures in the Rolling of Metals, by C. W. MacGregor and R. B. Palme. (58—A-260)

681 The Effects of Friction in the Rolling of Metals, by M. D. Stone.

TRANSACTIONS
Series E

Journal of
APPLIED MECHANICS
Vol. 81 • Series E • No. 4

CONTENTS FOR DECEMBER, 1959

TECHNICAL PAPERS

477 Boundary-Layer Solution for a Flow in a Diverging Passage Having a Swirl Component, M. A. Sinbel. (59—APMW-14)

485 Slow Rotatory Motion of a Circular Disk About One of Its Diameters in a Viscous Fluid, R. P. Kanwal. (59—APMW-6)

488 Thermal Stresses Owing to a Hot Spot in a Rectangular Strip, C. W. Nelson. (59—A-8)

491 Impact and Moving Loads on a Slightly Curved Elastic Half Space, A. C. Eringen and J. C. Samuels. (59—A-2)

499 Stability of Forced Oscillations With Nonlinear Second-Order Terms, Chi-Neng Shen. (59—A-19)

503 On Inertia Effects in a Transient Thermoelastic Problem, Eli Sternberg and J. G. Chakravorty. (59—APM-9)

510 Coupled Torsional and Longitudinal Vibrations of a Thin Bar, R. C. Di Prima. (59—A-18)

513 Production of Rotation in a Confined Liquid Through Translational Motion of the Boundaries, R. R. Berlot. (59—A-15)

517 Nonlinear Creep Deformations of Columns of Rectangular Cross Section, H. H. Bleich and O. W. Dillon, Jr. (59—A-1)

526 Forced Vibrations of a Circular Plate, Herbert Reismann. (59—A-9)

528 On the Propagation of Shock Waves in a Nonhomogeneous Elastic Medium, Eli Sternberg and J. G. Chakravorty. (59—APMW-17)

537 The Frequency of Flexural Vibration of Rectangular Orthotropic Plates With Clamped or Supported Edges, R. F. S. Hearmon. (59—APM-8)

541 Axially Symmetric Extensional Vibrations of a Circular Disk With a Concentric Hole, O. G. Gustafsson and T. R. Kane. (59—A-32)

546 Analysis of a Nonlinear Mechanical System With Three Degrees of Freedom, S. A. Hovanessian. (59—APM-29)

549 Stresses in an Ellipsoidal Rotor in a Centrifugal Force Field, M. A. Goldberg and Michael Sadowsky. (59—A-4)

553 Carrying Capacity of Elastic-Plastic Shells With Various End Conditions, Burton Paul. (59—APM-16)

561 Extensional Vibrations of Elastic Plates, R. D. Mindlin and M. A. Medick. (59—APM-4)

570 Triaxial Tension at the Head of a Rapidly Running Crack in a Plate, J. M. Frankland. (59—APM-11)

573 Viscous Flow Through Tubes of Multiply Connected Cross Sections, F. A. Gaydon and H. Nuttall. (59—APM-28)

Journal of
APPLIED MECHANICS
Volume 81 • Series E • No. 4

CONTENTS FOR DECEMBER, 1959
(continued)

577 On the Accuracy of Some Shell Solutions, G. D. Galletly and J. R. M. Radok. (59—APM-30)
584 The Drag on Spheres and Cylinders in a Stream of Dust-Laden Air, Thomas Gillespie and A. W. Gunter. (59—APM-14)
587 Elastic Flexible Cable in Plane Motion Under Tension, Wen-Hsiung Li. (59—A-6)
594 Incremental Stress-Strain Law Applied to Work-Hardening Plastic Materials, Chintsun Hwang. (59—APM-15)
599 On the Plastic Flow of Coulomb Solids Beyond Original Failure, A. W. Jenike and R. T. Shield. (59—A-7)
603 The Free Vibrations of Grillages, J. P. Ellington and H. McCallion. (59—APMW-12)
608 Piping Flexibility Analysis by Stiffness Matrix, L. H. Chen. (59—APM-24)
613 A Photoelastic Approach to Transient Stress Problems Employing Low-Modulus Materials, J. W. Dally, W. F. Riley, and A. J. Durelli. (59—A-10)
621 Rupture Characteristics of Safety Diaphragms, N. A. Weil. (59—APMW-3)
625 Bending of Isosceles Right Triangular Plates, H. J. Fletcher. (59—APMW-19)
629 Developments in the Application of the Grid Method to Dynamic Problems, A. J. Durelli, J. W. Dally, and W. F. Riley. (59—APMW-1)
635 The Solution of Elastic Stability Problems With the Electric Analog Computer, J. H. Shields and R. H. MacNeal. (59—APMW-20)
643 Symmetric Vortex Separation on Circular Cylinders and Cones, A. E. Bryson. (59—APMW-13)
649 Thermoelastic Problem for a Transversely Isotropic Hollow Sphere Embedded in an Elastic Medium, J. Nowinski. (59—APM-27)
651 Transient Analysis of Stress-Wave Penetration in Plates, Norman Davids. (59—A-16)
661 Transverse Flexure of a Semi-Infinite Thin Plate Containing an Infinite Row of Circular Holes, O. Tamate. (59—APMW-15)
666 Fundamental Frequency of a Thin, Flat Circular Plate Simply Supported Along a Circle of Abritrary Radius, R. Y. Bodine. (59—APMW-10)

669 BRIEF NOTES

689 DISCUSSION

696 BOOK REVIEWS

TRANSACTIONS OF THE ASME Series B

Journal of
ENGINEERING FOR INDUSTRY
Volume 81 • Series B • Number 4

CONTENTS FOR NOVEMBER, 1959

281 Dynamic Problems Associated With Satellite Orbit Control, by B. W. Augenstein. (59—Av-4)
289 Study of Machinability of Metals, by H. Takeyama and E. Usui. (58—A-161)
293 Four-Bar Linkages—Approximate Synthesis, by W. W. Worthley and R. T. Hinkle. (58—A-130)
301 A Theory for the Effect of Mean Stress on Fatigue of Metals Under Combined Torsion and Axial Load or Bending, by W. N. Findley. (58—A-61)
307 An Analysis of Critical Stresses and Mode of Failure of a Wire Rope, by W. L. Starkey and H. A. Cress. (58—A-63)
317 An Application of Statistics to the Dimensioning of Machine Parts, by M. F. Spotts. (58—A-44)
323 The Dynamic Analysis and Design of Relatively Flexible Cam Mechanisms Having More Than One Degree of Freedom, by R. C. Johnson. (58—A-192)
332 Power Heat Balance Considerations in Design and Operation of Industrial Plants, by J. I. Hudson. (58—A-166)
339 Influence of Hot and Cold Storage-Loads on the Refrigerated-Space Temperature of a Cooling Complex, by C. F. Kayan. (58—A-165)
348 Development and Uses of a New Line of Vibratory Feeders and Unit Vibrators, by A. F. Israelson. (59—SA-33)
353 A Mechanical Time-Delay Device Sensitive to Centrifugal Fields, by J. R. Baumgarten, R. Cohen, and A. S. Hall, Jr. (59—SA-9)

TRANSACTIONS OF THE ASME Series C

Journal of
HEAT TRANSFER
Vol. 81 • Series C • No. 4

CONTENTS FOR NOVEMBER, 1959

253 Dynamic Response of Heat Exchangers Having Internal Heat Sources—Part III, by V. S. Arpaci and J. A. Clark. (58—SA-39)
267 Heating and Cooling Air and Carbon Dioxide in the Thermal Entrance Region of a Circular Duct With Large Gas to Wall Temperature Differences, by Helmut Wolf. (59—SA-15)
280 Turbulent Fow in a Circular Tube With Arbitrary Internal Heat Sources and Wall Heat Transfer, by R. Siegel and E. M. Sparrow. (59—SA-19)
291 Laminar Condensation Heat Transfer on a Horizontal Cylinder, by E. M. Sparrow and J. L. Gregg. (59—SA-13)
297 The Use of Thin Films for Increasing Evaporation and Condensation Rates in Process Equipment, by E. L. Lustenader, R. Richter, and F. J. Neugebauer. (59—SA-30)
308 Some General Considerations of the Heating of Satellites, by A. J. Eggers, Jr., T. J. Wong, and R. E. Slye.
315 The Penetration of Planetary Atmospheres, by Carl Gazley, Jr. (59—Av-27)
323 Thermodynamic Properties of Helium at Low Temperatures and High Pressures, by D. B. Mann and R. B. Stewart. (59—HT-19)
327 Radiation Fin Efficiency for One-Dimensional Heat Flow in a Circular Fin, by R. L. Chambers and E. V Somers. (59—HT-8)

SUMNER ALPERT
Chief Technical Engineer
Mem. ASME

R. E. GREY
Senior Experimental Engineer

W. O. FLASCHAR
Application Engineer,
Solar Aircraft Company,
San Diego, Calif.

Development of a Three-Stage Liquid-Cooled Gas Turbine

A three-stage gas turbine was designed to operate at 1750-F inlet temperature with nonstrategic, low alloy components. The rotor blades are cooled with water in a closed system, and the stators are cooled with air. A practical design for the rotor was evolved and tested. Heat-transfer data correlated well with expected values.

I Introduction

THIS PAPER DESCRIBES the design and test work conducted during a program to develop a three-stage, liquid-cooled gas turbine. It is a continuation of a paper presented to the ASME three years ago [1].[1] At that time a single-stage turbine had been operated successfully over 200 hours.

The program, sponsored by the Bureau of Ships, U. S. Navy, had as its objectives the development of a gas turbine that would utilize little or none of the so-called strategic materials: Nickel, chromium, molybdenum, tungsten, cobalt, columbium, beryllium. The rotor was to be cooled with a closed cooling system. Methods of stator cooling were optional. The gas turbine was to utilize the compressor developed by Solar Aircraft Company for its 500-hp Jupiter[2] gas turbine and over-all performance was not to be sacrificed to make cooling possible.

Considerable development work had been done both in this country and abroad on the subject of liquid cooling. These efforts had been aimed primarily at solution of the theoretical problems associated with cooling. Data on internal and external heat-transfer coefficients had been obtained and detail studies of the mechanism of cooling had been conducted at the Lewis Laboratory of the NACA (now NASA). Almost all of this earlier work had been conducted with research equipment, and practical designs had not been evolved. An excellent summary of gas-turbine cooling research was presented to the ASME [2].

The program conducted at Solar was intended to produce a practical turbine based on the basic data available from NACA and others. To this end a design was selected with considerations for data taking made secondary to economical manufacture. Initial design considerations ruled out single-piece turbine construction with blade, rotor, and shaft, all produced from a single billet. Instead, a more conventional design and method of fabrication were sought that would permit blades and rotor disks to be readily changed.

II General Cycle and Cooling Considerations

A Design Point. Though the use of an existing compressor was specified, thus limiting the freedom of design point selection, turbine inlet temperature was not specified. From combined cycle and cooling considerations, the turbine inlet temperature was set at 1750 F. Cycle design data are given in Table 1.

Table 1 Turbine design data

Ambient pressure	psia	14.7
Ambient temperature	deg F	80.0
Air-flow rate	lb/sec	6.57
Compressor inlet pressure drop	in. H_2O	4.0
Compressor pressure ratio		4.87:1
Combustor pressure drop	per cent of inlet pressure	3.0
Combustion efficiency	per cent	95.0
Turbine inlet temperature	deg F	1750
Turbine inlet pressure	psia	68.8
Turbine gas flow rate	lb/sec	6.5
Turbine back pressure	in. H_2O	10.0

B Cooling Methods. Extensive studies were conducted to establish the cooling systems for the rotors and stators. For the rotors, a closed system was specified. To be established were the cooling fluid and type of system. Water was selected and a forced-convection system established.

The advantages of water were obvious: Availability, economy, good heat-transfer medium, and no special handling precautions required. Its major disadvantages were its low boiling point and its exceedingly good heat-transfer characteristics. To eliminate boiling within the cooling passages where pressure was not available, fluid temperatures had to be kept below 200 F. At this temperature, the low turbine blade temperatures resulted in an excessive amount of heat being extracted by the coolant. This negative reheat effect lowered over-all performance by about 20 per cent.

A forced-convection cooling system was selected over the free-convection or mixed systems because the mechanism of forced convection was better understood and the blind holes used in the free-convection system were considered too vulnerable to plugging.

The material limitations required the use of low alloy steels. Hence temperatures in highly stressed regions had to be maintained below 800 F, and peak metal temperatures limited to about 1100 F. The materials selected are discussed in reference [1].

The calculated variation of coolant temperature rise with flow for each of the three stages is given in Fig. 1. Also shown are the prevalent or mean blade temperatures. For the first-stage rotor blades, trailing edge tip temperatures of 1100 F were estimated.

Air cooling was selected for the stators, as it appeared that heat-transfer losses could be minimized. Water, having too good a conductivity, would over-cool the stators. Inasmuch as stress levels are lower in the stators, higher temperatures could be tolerated. Air cooling was attractive if the coolant could be used at a pressure lower than that of the gas stream; with high pressure air the penalty involved in compressing the air was too great. Accordingly, the stators were designed to use air at a pressure

[1] Numbers in brackets designate References at end of paper.

[2] Registered trade-mark.

Contributed by the Gas Turbine Power Division and presented at the Gas Turbine Power Conference and Exhibit, Cincinnati, Ohio, March 8–11, 1959, of THE AMERICAN SOCIETY OF MECHANICAL ENGINEERS.

NOTE: Statements and opinions advanced in papers are to be understood as individual expressions of their authors and not those of the Society. Manuscript received at ASME Headquarters, December 31, 1958. Paper No. 59—GTP-1.

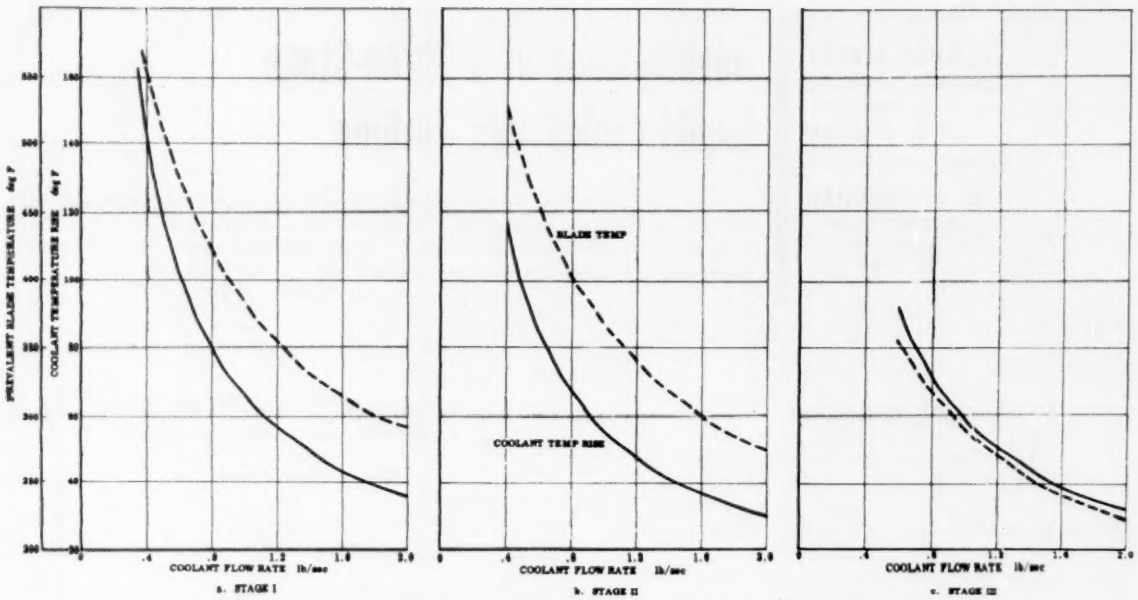

Fig. 1 Variation of coolant temperature rise and prevalent blade temperature with coolant flow rate

comparable to compressor second-stage bleed. The use of this low-pressure air required sealing to prevent leakage of the high-pressure hot gases into the cooling passages.

Using NACA data, the stator blades were designed with internal extended surfaces.

C Heat-Transfer Rates and Over-All Performance. Heat-transfer calculations were used to establish coolant flow rates and heat rejection rates. The cooling losses in the turbine were calculated as shown in Table 2.

Table 2 Turbine heat rejection rates (Btu/sec)

	Stage		
	I	II	III
Stator blades	26.2	15.0	12.8
Stator shrouds	28.7	14.4	9.0
Rotor blades	78.0	58.2	51.5
Rotor disks	14.9	10.8	7.9
Total	147.8	98.4	80.2

In computing turbine performance the following assumptions were used:

1 The total temperatures entering the rotor would be reduced by the heat transfer in the preceding stator.

2 The effective total temperature in the rotor would be further reduced by an amount equivalent to one half of the rotor-blade heat-transfer rate.

3 The total temperature entering a stage would be reduced by the total of all preceding transferred heat.

Over-all power plant performance is given in Table 3.

All the design calculations were conducted on the basis of the gas turbine used in a shaft power output configuration. During the course of the program it was found expedient to use a larger compressor and to extract power as bleed air from the compressor. This eliminated the need for a new gear box, and a Solar T-300J air-bleed compressor and accessory drive gear box were used. In this configuration, the use of air bleed lowered the turbine pressure level and thus the heat-transfer rate. The reduction was calculated to be 10 per cent in the first stage and less in the second and third.

Table 3 Design power-plant performance

Turbine power output	hp		1412
Compressor power	hp	864	
Cooling air power	hp	17	
Power consumed in bearings	hp	15	
Liquid coolant pumping	hp	5	
Oil pumps	hp	1	
			902
Shaft power available	hp		510
Gear loss	hp		10
Net power	hp		500
Fuel rate	lb/hr		479
Specific fuel consumption	lb/hp-hr		0.96
Over-all thermal efficiency	per cent		14.4

III Mechanical Design

A Rotor Blades. For high efficiency a three-stage reaction turbine was designed. For effective cooling of the rotor blade trailing edges, fairly thick trailing edges were specified. The high reaction and the low velocities in the turbine allowed these relatively thick blades to be used without excessive losses. Other than this compromise, fairly conventional design practice was used, based on free vortex flow and resulting in twisted rotor blades.

The rotor blades were fabricated from precision castings. Steps in the fabrication of rotor blades include:

1 Precision cast from low alloy steel.
2 Anneal the casting.
3 Drill coolant holes and manifold holes.
4 Chromize for corrosion protection.
5 Braze tip cap and manifold end plugs.
6 Heat treat to tensile strength of 130,000 psi.
7 Crush grind rotor-blade base.
8 Braze O-ring studs into bottom of base.
9 Pressure and flow test.

A sketch of the cooling passages in a rotor blade is shown in

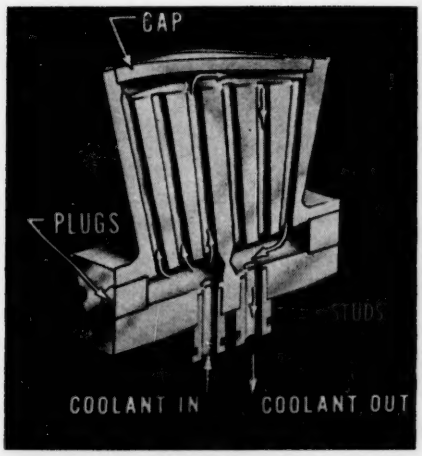

Fig. 2 Cutaway of rotor blade

Fig. 3 Section through first-stage rotor blade

Fig. 2. Six radial holes were used for the first-stage blades and four for the second and third stages. A photograph of a section through a blade is shown in Fig. 3.

During early tests, several blades were fabricated with a copper insert in the trailing edge. These were designed to provide a high conductivity path so as to reduce trailing edge temperatures as suggested in reference [3]. Slots 0.060 in. wide were milled in the trailing edge, and copper inserts were cast into these slots by induction heating in a vacuum retort. A copper insert is shown in Fig. 3.

B Rotor Assembly. As reported in reference [1], a single-stage turbine was built first. It utilized a rotor disk split in the radial plane with conventional axial fir-tree slots to retain the blade. The cooling fluid was supplied to each blade from a housing located in the center of the split wheel. To connect each blade and the housing, two $^1/_8$-in-diam tubes were brazed into the blade and sealed into the housing by O-rings. This design was tested for 100 hours at gas temperatures of 1700 F and was found to be adequate. The assembly operation, however, was difficult and a new design was sought for the three-stage turbine.

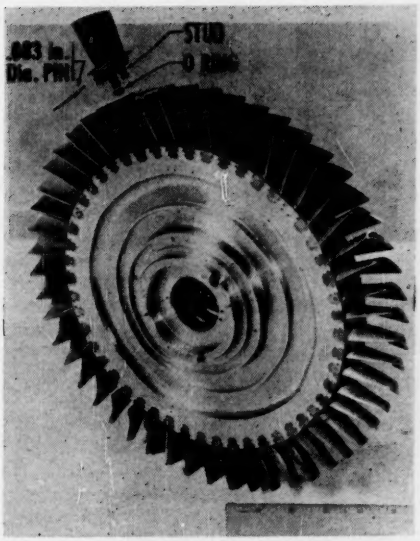

Fig. 4 Pin-mount method of rotor-blade attachment

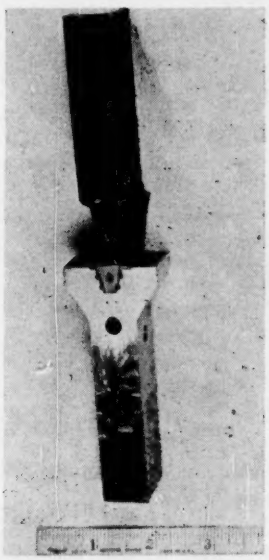

Fig. 5 Test assembly-simulated blade attachment

As finally developed, the three-stage turbine utilized separate, solid rotor disks. Blades were retained individually in the disk and the disks were stacked onto a shaft. The use of O-ring seals in the coolant passages between the blades and the disks was retained. These O-ring seals required that the blade be inserted radially into the rim of the wheel, eliminating the possible use of conventional axial fir-tree slots. In their place a simple Vee slot was used as shown in Fig. 4. The blade could be plugged in radially and retained by axial pins. Such pinned blade mounts were possible because of the effective cooling of the disk and blade base. Four pins, 0.083 inch in diameter, were used in each blade. Wheel slots were broached and blade bases crush ground, each providing one half of the cylindrical pin slots. Pull tests on a simulated blade mount indicated strength levels 3.5 times that required. A photo of the test pieces is shown in Fig. 5.

A cross section of a typical rotor assembly is shown in Fig. 6.

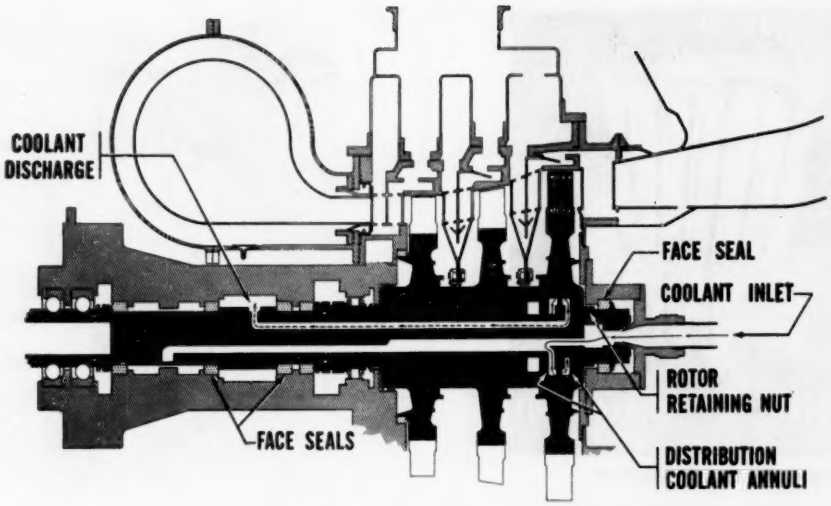

Fig. 6 Cross section of rotor assembly

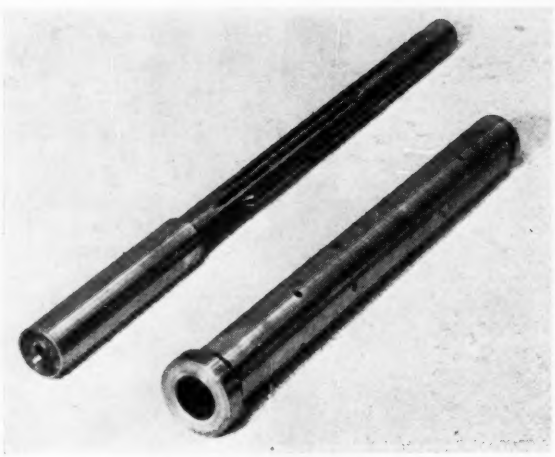

Fig. 7 Rotor shaft components—before brazing

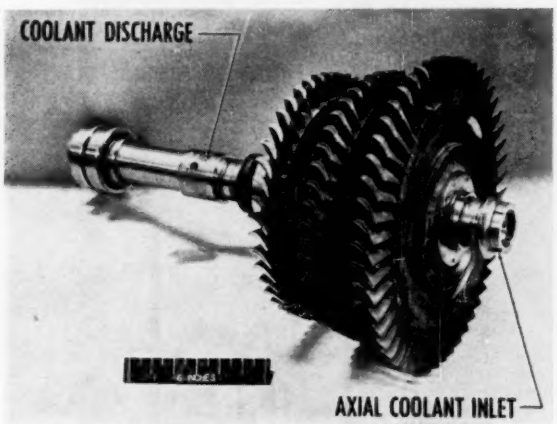

Fig. 8 Three-stage rotor assembly—axial coolant inlet

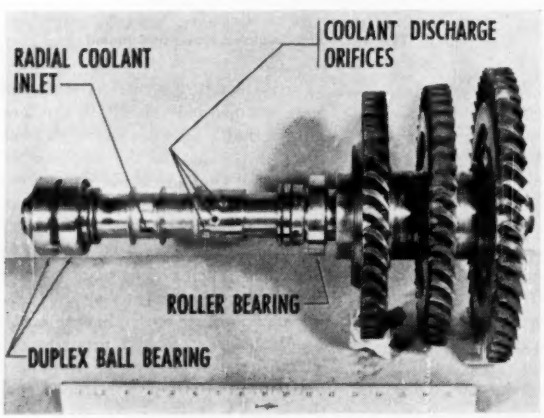

Fig. 9 Three-stage rotor assembly—radial coolant inlet

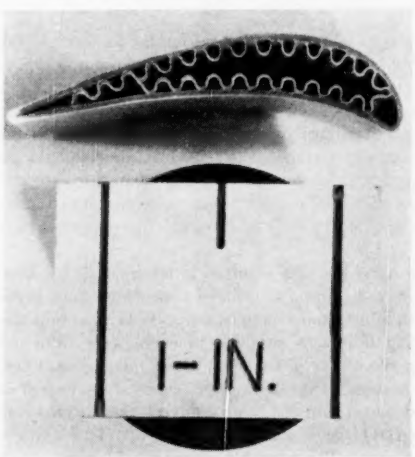

Fig. 10 Section through stator vane

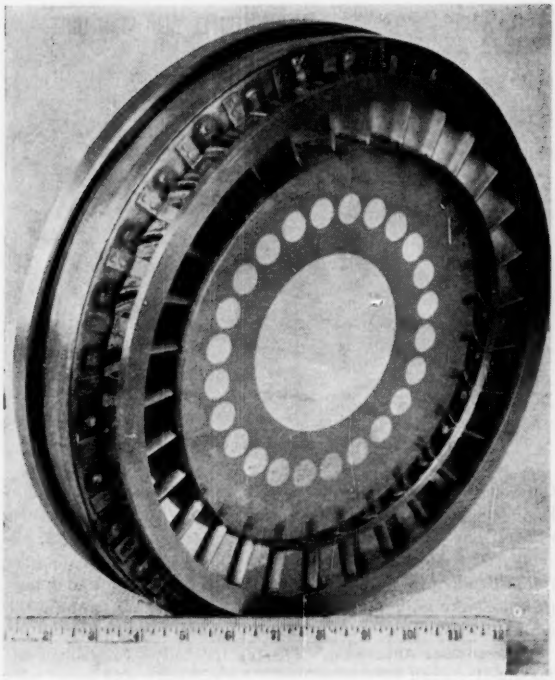

Fig. 11 Stator, Stage II—partial assembly

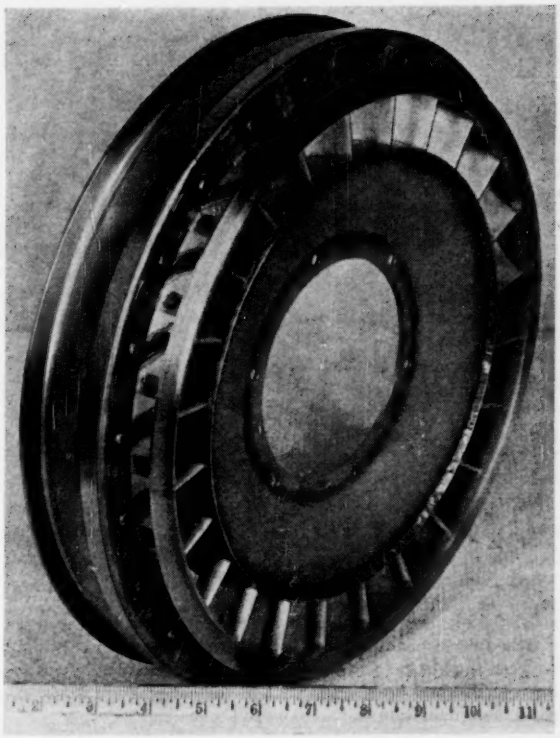

Fig. 12 Stator, Stage II—complete assembly

The disks were turned from pancake forgings. A central hole was bored, and coolant supply and return cavities were machined. After finish machining, the blade slots were broached in the rim. From the bottom of each slot, supply and return holes were drilled into the cavities. These holes were $^1/_8$ inch in diameter and were counterbored to a diameter of $^1/_4$ inch to a depth of 0.312 inch. Two studs were brazed into the base of each blade, each carrying a −1 size O-ring. The studs and counterbored portions of the coolant holes provided close dimensional control for good O-ring sealing. The fluid pressure built up in the wheel by centrifugal force is about 3000 psi in the first stage at the O-ring and about 4000 psi in the third stage.

Cooling fluid was transferred to and from each stage by the turbine shaft. This shaft was fabricated in two pieces as shown in Fig. 7. The center solid member was fluted on its outside to provide 12 slots. This center member was copper-brazed into an outer cylindrical sleeve. The passages formed between the slots and the outer sleeve were used for coolant transfer. A common coolant supply was used with six passages, three on each side of the shaft. Coolant return from each stage was separated, two passages per stage, diametrically opposed. The flutes between the adjacent supply passages were locally milled out to ensure equal flow to each passage. A photograph of the assembled three-stage rotor is shown in Fig. 8.

Initially, fluid entrance was through radial slots in the shaft at a station between the bearings, as shown in Fig. 9. The inlet was flooded and outlet throttling was used for control. Flow rates for each stage were determined from special tests in which the coolant from each stage was collected separately. In the final design, coolant flow was controlled by orifices separately sized in pairs for each stage. These can be seen in Figs. 8 and 9.

The efficiency of the radial inlet left much to be desired, and necessary flow rates could not be obtained at design speed. Accordingly, the radial inlet was abandoned and an axial inlet installed on the downstream face of the shaft. The nut that retained the three rotors to the shaft was modified to serve as a seal rub ring and coolant pickup. The rotor modified for axial inlet is shown in Fig. 8.

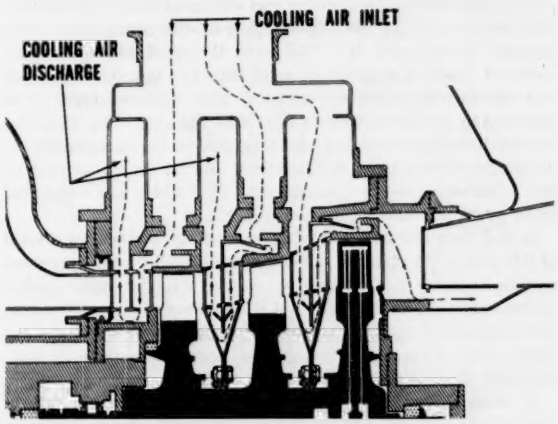

Fig. 13 Cross section of turbine—showing cooling air-flow path

C Stators. The stator vanes were fabricated of sheet metal 0.025 inch thick. The trailing edges were welded. To provide corrosion protection to the lean alloy steel, chromizing was used. The internal corrugation was rolled from 0.008-inch mild steel sheet and also chromized. A typical stator vane after brazing is shown in Fig. 10. The individual vanes were brazed into inner and outer shroud rings and baffles added to guide the cooling air. Photographs of the second stage stator in process of fabrication are shown in Figs. 11 and 12. The cooling air-flow path for each stator can be seen in Fig. 13. Air was distributed through manifolds surrounding the turbine casing. The casing was pierced to

Fig. 14 Turbine casing

allow the air flow to penetrate as shown in Fig. 14. The holes matched corresponding holes in each stator assembly. Sealing between the hot gas and the coolant air was provided by convoluted metal rings designed so that the higher pressure would expand the convolution and accomplish the sealing.

IV Test Program and Results

The liquid-cooled gas turbine was subjected to extensive tests. The 100-hour test of the single-stage split disk configuration was reported in reference [1]. To prove the feasibility of the pin-mounted blade, a single-stage solid disk was tested. The rotor was straddle-mounted and coupled to a dynamometer. The rotor setup for these tests is shown in Fig. 15. The straddle-mounted configuration was advantageous for instrumentation to determine turbine blade temperatures and for control of coolant flow. Following the component tests, the turbine was assembled as an overhung machine as shown in Fig. 8.

It had been planned to run the three-stage turbine for a total of 500 hours. Mechanical difficulties were such that the program was discontinued after 119 hours. At that time the engine needed minor repairs to be operable, but it was concluded that the general purposes of the program had been accomplished.

A review of the design features and operating experience indicate that the design is fundamentally sound.

A Rotor Blades. The early tests were plagued with a rash of rotor-blade failures. These failures occurred almost wholly in the blade tip caps. Alternate methods of brazing were studied and proof pressure tests up to three times operating level were performed. Blades in the first stage were especially prone to these failures. It was found that blade strength was impaired by a loss of braze fillet at the time the rotor tip diameter was ground. In the second stage, the cap was recessed so that generous fillets remained after the tip diameter was ground. This can be seen in Fig. 8, in which typical blade tips are shown. The major force on the blade cap is from fluid pressure, and the fact that blades passed leak and proof pressure tests was taken to indicate that the shear area was adequate. When operating in a turbine, thermal effects caused by temperature gradients could easily produce local tension loading on the braze and result in failure.

Toward the end of the program, tip caps were welded in place.

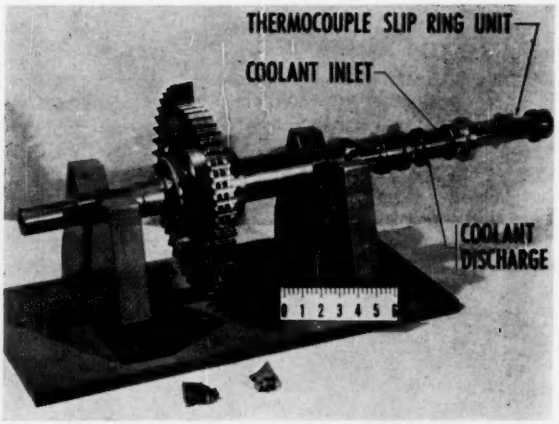

Fig. 15 Straddle-mounted Stage I rotor assembly

Careful technique was required to minimize burn-through and a loss of the airfoil profile. In addition, the alloy used in the blades was air-hardenable, and welding cracks were frequently encountered. At the conclusion of the program, blade caps were retained adequately, but fine leaks detectable only under high pressure were found in several blades. The brazed joints in the blade manifold plugs and O-ring studs caused no problems.

B Rotor-Blade Attachment. The pin method of rotor-blade attachment proved very successful. No difficulty was found with the feature. Blades were readily interchangeable, and the pin joint could withstand a large amount of abuse. Blades could be readily changed and at times were changed without rebalancing the rotor. Several pins were drilled out with a hand drill and a number of holes had drill drifts that caused uneven pin loading, but no pin failures occurred.

C Disk and Shaft Design. The separate solid disks with O-ring seals proved to be very practical. Individual rotors could be assembled, pressure tested, and then stacked onto the shaft. By removing the exhaust collector, the rotor disks could be readily removed as shown in Fig. 16. With adequate chamfers on the disk bores, the assembly could be readily made without cutting the O-rings.

Special techniques were developed for balancing the rotors. Blades were weighed individually and selected for assembly. For balancing, the entire rotor was filled with water. Filling was done by evacuating the system, and then allowing the water to be drawn in. Because of the nature of the blade fabrication, some rather large out-of-balance conditions were found, and compensation would require the removal of a considerable amount of material from the rotor. This was objectionable as it removed the nickel-plating and subjected the disk to corrosion. Since, one time, holes had been drilled through the disks just below the wheel rims for instrumentation, balancing was achieved by inserting tungsten plugs.

In almost all cases for which satisfactory machine balancing was accomplished, no vibration troubles were encountered. As was noted, blades were changed on the test stand without rebalancing and usually but not always without producing critical unbalance.

D Stators. The stators were damaged by rotor-blade tip caps coming loose. Typical damage can be seen in Fig. 17. As reported in reference [1], air cooling of the stators was generally inadequate. One major failure occurred with a rupture of the weld joining the cover plates to the inner shroud ring. This failure was attributed to overheating. New plates were welded into place after internal baffles were added to provide more effective internal cooling in that area.

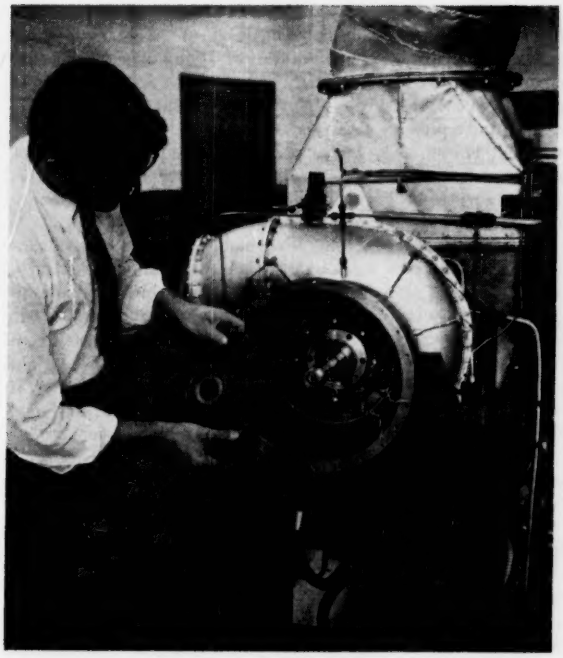

Fig. 16 Assembly of a rotor disk

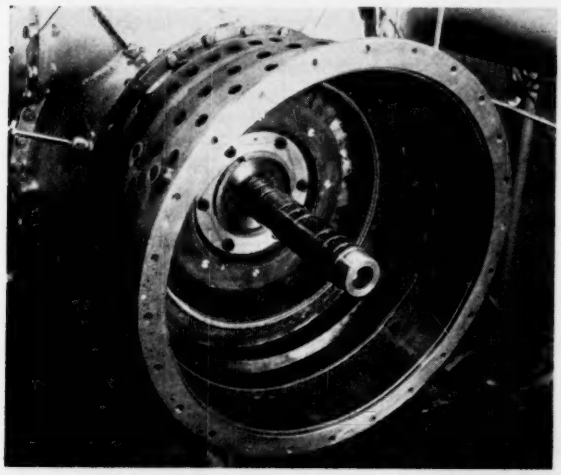

Fig. 17 Typical damage to first-stage stator

E Bearings. Conventional antifriction bearings were used with good results. Some initial difficulty was encountered with the roller bearing as a result of differential thermal expansion. With the outer race in a warm housing and the inner race in contact with a cold shaft, an increase in radial clearance would take place. This resulted in loss of one bearing, and the assembly was changed to provide for a lower initial radial clearance.

F Coolant Seals. After extensive research and testing, various types of coolant seals in the earlier part of the program, standard carbon-face Sealol seals were selected for use in the engine. A minimum diameter seal was selected to be compatible with the shaft design to minimize circumferential rubbing velocity. From the manufacturer's recommendation and the seal test rig experience, the flatness and surface quality of the rub ring mating face was found to be extremely critical in its effect on seal life.

Very close stack-up dimensions were taken on engine assembly and shims installed to assure proper seal spring compression. During actual operation many seal failures occurred. These failures were attributed either to foreign matter in the coolant, an out-of-flatness on the rub ring caused by distortion on stack-up, or excessive engine vibration. Individual seals, which were operated under ideal conditions where the mating rub ring surface was not distorted and foreign particles did not enter the system, displayed excellent wearing capabilities for long life. Because of the experimental nature of the program, seal lives of 50 hours or less were attained.

G Corrosion-Resistant Coatings. Examination of the turbine parts indicated various degrees of effectiveness of the corrosion-resistant coatings. Parts in contact with the hot gas had been chromized and generally evidences of residual surface chrome were apparent. Most of the loss in protection is believed to have resulted from excessive vapor blasting.

Machined parts that had been protected with electroless nickel plate showed similar irregular residual protection, again caused mostly by handling and cleaning.

V Performance

Extensive data were taken to confirm design performance and heat-transfer calculations. Aerodynamically, the turbine was found to yield satisfactory performance when run with reasonable tip clearances. Because of the early failure of blade tip caps, honeycomb seals with generous clearances were used except during tests to determine performance.

A Heat Transfer. Heat-transfer data for the liquid-cooled rotor indicated that design calculations were more than adequate. At the engine design point, a total heat rejection rate to the coolant of 187.7 Btu/sec had been estimated. As the measured flow rates were higher than design, the theoretical curves of rotor-blade heat transfer (Fig. 1) were used with the flow rates from the actual test to re-estimate heat-transfer rates. These results are presented in Table 4.

Table 4 Theoretical rotor heat-transfer rates for measured flow

Stage	Coolant flow, lb/sec	Blade Q, Btu/sec	Disk Q, Btu/sec
I	0.885	82.9	14.9
II	1.162	73.4	10.8
III	0.720	68.5	7.9
	Total	224.8	33.6

Thus the total theoretical rotor heat rejection rate is 261.4 Btu/sec. The measured rate was 237.0 Btu/sec, 9 per cent below the theoretical value. This difference can be explained by the fact that the theoretical values were based on the shaft-power configuration, whereas the measured values were obtained with an air-bleed configuration. The lower pressure for the air-bleed configuration would produce a lower heat rejection rate.

An over-all heat balance is presented in Table 5.

Table 5 Design point heat balance from test data

Gas flow rate	lb/sec	6.88	
Turbine inlet temperature	deg F	1750	
Turbine outlet temperature	deg F	1050	
Turbine enthalpy drop	Btu/sec		1368
Shaft power output			
Compressor enthalpy rise	Btu/sec	958	
Mechanical losses (1 per cent)		10	
		968	
Heat rejection to coolant water	Btu/sec	237	
Heat rejection to coolant air			
2.7 lb/sec			
249 F ΔT	Btu/sec	156	
Unaccounted heat losses	Btu/sec	7	
Total enthalpy drop, Btu/sec			1368

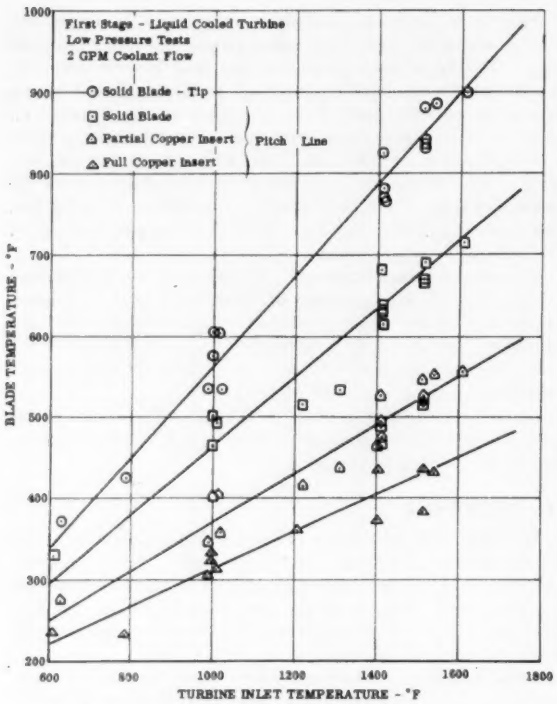

Fig. 18 Rotor-blade trailing edge temperatures

For the over-all power plant, reduction of the measured performance data to conditions comparable to design for a shaft power machine resulted in an output of 488 hp at a specific fuel consumption of 0.987 lb/hp-hr. This does not reflect the power required to cool the stators. At the design point, 2.7 lb/sec of air at 75 F and a pressure of 20 psig were supplied. This is equivalent to about 175 hp. The higher pressure was required to keep hot gas from leaking into the cooling passages. Even with this cooling air pressure, evidence of leakage was found in the sooty deposits in the cooling air collector.

D Coolant Control. A study was conducted of methods of control of coolant flow rates. Although for optimum efficiency, constant blade temperatures would be desirable, a system to provide the control was considered to be too complicated. It was decided to adopt a control system that utilized natural convection pumping for control.

As the return fluid is heated, and thus is at a lower density, it can be demonstrated analytically that a net pressure rise should occur in the rotor. This pressure rise would be proportional to the coolant temperature rise and to the square of the speed. During single-stage tests, attempts were made to measure this pressure rise. At constant speed the gas temperature was raised and the coolant flow rate adjusted to a constant value. The resulting pressure rise was plotted against temperature rise as shown in Fig. 19. Though the convection pumping effect can be seen to occur, its magnitude was only a fraction of that anticipated.

For the three-stage turbine, this convection pumping effect was used to provide coolant control. Fixed area orifices were installed in the discharge line as shown in Figs. 8 and 9. These were sized individually for each stage, but because difficulty was experienced with Stage II, it was run with a wide open discharge.

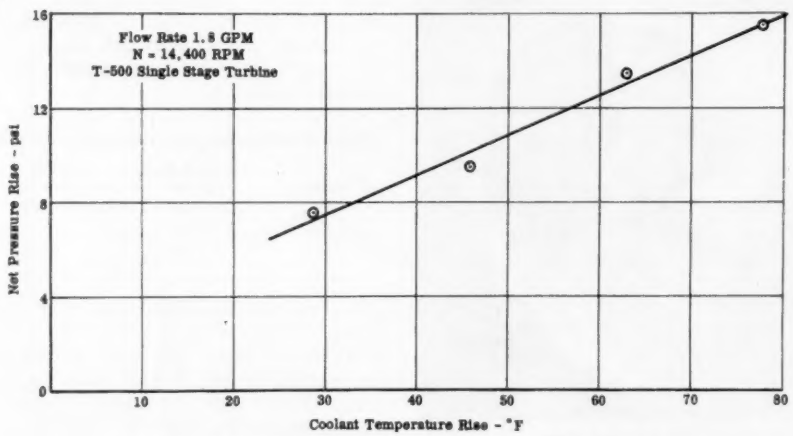

Fig. 19 Net coolant pressure rise versus temperature rise, Stage I

B Blade Temperature Measurements. Data taken during the single state tests confirmed calculated rotor-blade temperatures. A comparison of blade temperatures with and without copper inserts is shown in Fig. 18. Inasmuch as maximum temperatures even without the insert were relatively low, it was concluded that the inserts were not necessary.

C Turbine Efficiency. The turbine efficiency calculated from the total pressure ratio and the work output was 78 per cent, as compared to a design value of 82 per cent. The design value corresponded to the higher pressure ratio of the shaft-power machine. The measured value was obtained under bleed conditions. It is felt that the deterioration of the stator, due to damage, and the high heat loss were responsible for the lower efficiency.

Data taken during engine tests demonstrated that, as the gas temperature and coolant temperature were increased, the coolant flow rate automatically increased. These data are shown in Fig. 20.

The increase in coolant flow with coolant temperature rise (and gas temperature) indicates that the convection pumping effect is occurring. Again, the magnitude is less than expected theoretically. For an increase in the coolant temperature rise from 70 to 90 degrees, the actual coolant flow rates increased 7.3 per cent, as compared to a theoretical value of 16.3 per cent.

VI Conclusions

Though the test operation of the liquid-cooled gas turbine was

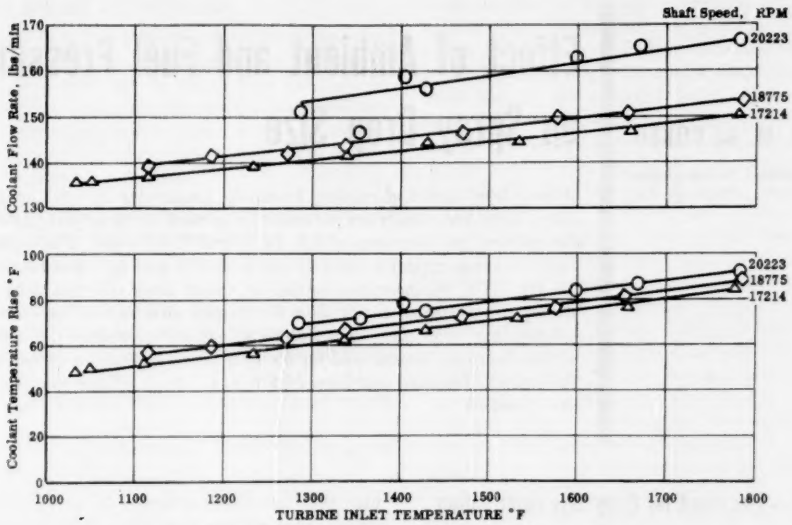

Fig. 20 Cooling system performance, liquid-cooled turbine

not carried through the scheduled number of hours, most of the design details have been adequately proved. The following conclusions are drawn both from the present paper and the earlier data of reference [1].

1 It was demonstrated that a low alloy turbine could be operated successfully at temperatures over 1700 F.

2 Adequate corrosion protection can be given to low alloy steels for use in liquid-cooled gas turbines.

3 Available data on heat-transfer coefficients are accurate for prediction of cooling losses and blade temperatures.

4 High temperature brazing can be used effectively for the fabrication of components of cooled turbines.

5 The pin method of blade attachment is effective in producing a practical design.

6 O-rings were satisfactory for coolant seals between shaft and disk and between disk and blades.

7 Natural convection effects were measured though of lesser magnitude than expected theoretically.

8 The radial coolant inlet to the shaft could not be developed satisfactorily. Additional work will be necessary to ascertain if it is feasible. The axial coolant inlet was entirely satisfactory.

9 Face-type coolant seals can be used if cleanliness, installation accuracy, and low vibration can be maintained.

10 The design tested did not wholly solve the stator cooling problem. The possible use of ceramic or liquid-cooled stators should be considered.

11 The turbine inlet scroll was never successfully cooled, as high alloy liners were used. For high temperatures, turbine inlet scrolls are undesirable unless heavy, furnace-type construction can be used. An engine arrangement with a straight-through flow path is required.

In summary, the experience with this development program supports the conclusion that liquid-cooled turbines are feasible if the added weight and complication can be tolerated. Studies of reliability of gas-turbine plants have indicated that the environmental stress resulting from high temperatures is one of the major causes of malfunctions. Liquid cooling, or any cooling, can reduce the deleterious effects of high temperatures, but with the penalty of added complexity. In the field of small gas turbines, the complexity does not appear to be warranted for most known applications. For larger, stationary machines, the picture may be different. With the use of high alloy steels, turbine inlet temperatures over 2000 F appear possible. With high inlet gas temperatures, exhaust gas temperatures are also high, and cycles utilizing exhaust heat recovery can show attractive theoretical performance.

In conclusion, the authors would like to express agreement with the statement made by Dr. von der Nuell in a recent paper [4], "In general, resort should not be taken to higher working temperatures until all other methods of improvement have been exhausted, especially when such methods mean greater safety, longer life, greater freedom in materials, and numerous other significant advantages."

References

1 S. Alpert, R. E. Grey, and D. D. Drake, "Application of Internal Liquid Cooling to Gas Turbine Rotors," TRANS. ASME, vol. 78, 1956, pp. 1257–1266.

2 J. B. Esgar, J. N. B. Livingood, and R. O. Hickel, "Research on Application of Cooling to Gas Turbines," TRANS. ASME, vol. 79, 1957, pp. 645–651.

3 John C. Freche, "A Summary of Design Information for Water-Cooled Turbines," NACA RM E 51 A 03, 1951.

4 W. T. von der Nuell, "General Design Considerations for Smaller Gas Turbines," TRANS. ASME, vol. 80, 1958, p. 941.

Effect of Ambient and Fuel Pressure on Spray Drop Size

S. M. DE CORSO

Mechanics Department, Westinghouse Research Laboratories, Pittsburgh, Pa.

After a brief review of existing knowledge concerning the effect of ambient pressure on spray drop size, results are presented for a swirl nozzle at fuel Δp's of 25 and 100 psi for ambient gas pressures of 0.5, 14.5, and 114.5 psia. The liquid sprayed is diesel fuel, the nozzle capacity being 45 gal/hr at 100 psi Δp, and the nominal spray angle, 80 deg. The photographic method by which drop size was determined is described. Curves are presented which show the spatial variation in fuel flow rate, spray-stream velocity, and drop size. The notable effects are large drop size and velocity variations across the spray stream, and for the total nozzle output, an increase in the drop size as the ambient pressure goes from 14.5 to 114.5 psia. Some ramifications of the results are discussed.

1 Introduction—The Need for Drop-Size Information

THE LACK OF KNOWLEDGE concerning the drop size distribution of nozzle sprays has long been a stumbling block in the path of progress in many fields where nozzles are used and in particular in combustion processes. This lack of knowledge about fuel spray characteristics makes it difficult to predict accurately the performance of gas turbine, jet engine, or rocket combustion chambers when the operating conditions are varied. In these fields much importance is attached to similitude studies which would enable one to test at convenient and economical engine flow conditions or with scaled-down combustion chambers; and also to scale up or down in size a successful combustion system. Here fuel atomization has an important role and successful scaling of combustion systems depends on knowing the behavior of fuel atomizers.

The effects on drop size of nozzle pressure and fluid properties have been studied by numerous investigators, but with few exceptions this work has been done at atmospheric ambient conditions. A few studies of drop size have been done at elevated ambient gas pressures. Lee [1, 2][1] reported negligible effect of ambient gas density on drop size at a fuel pressure drop (Δp) of 4120 psi at chamber air density values of 0.31, 0.94, 1.56 lb/ft³. He compares his results with those of Sass [3] who reported a decrease in drop size with increasing gas pressure at a fuel Δp of 4120 psi at chamber air densities of approximately 0.07, 0.38, 0.77 lb/ft³; and with Woltjen [4] who was unable to detect changes in the atomization due to changes in the air density. More recently, Giffen and Lamb [5] conducted experiments at a fuel Δp of 1800 psi for air densities of 0.076, 0.336, 0.597, 1.116, 2.155, and 3.20 lb/ft³. They found a decrease in drop size with increasing gas density. They compare their results with those of Lee and Sass and, in addition, Retel [6]. Retel's data show a decrease in drop size followed by an increase as air density goes from 0.25 to 2.25 lb/ft³. Thus there appear to be conflicting results concerning the effect of ambient gas pressure on drop size; and, in addition, for all the work listed, the injection pressures were so high that the resulting Sauter Mean Diameter (S.M.D.) of the sprays were all less than 50μ. This leaves unexplored a wide range of interest in the effects of gas density at lower fuel pressures, an example being the gas-turbine range at fuel pressures of 25 to 400 psi. Work has already been done at this laboratory to find the effect of ambient and fuel pressure on fuel distribution [7].

Now the objective is to study the drop size distribution of fuel sprays at fuel Δp's of 25 to 400 psi, while varying ambient gas properties. This paper reports the results so far obtained in this endeavor, namely, drop-size data for a 45-gph—80-deg nozzle at fuel Δp's of 25 and 100 psi, and ambient gas pressures of 0.5, 14.5, and 114.5 psia. The ambient gas used was nitrogen at room temperature and the fuel sprayed had the following properties: Specific gravity at 60 F = 0.84; surface tension at 77 F, 30 dynes/cm; viscosity at 77 F = 2.4 centistokes. The nozzle is of the pressure atomizing centrifugal type which has found wide usage. Fig. 1 shows the construction of such a nozzle. The evaporation rate from the spray is negligible.

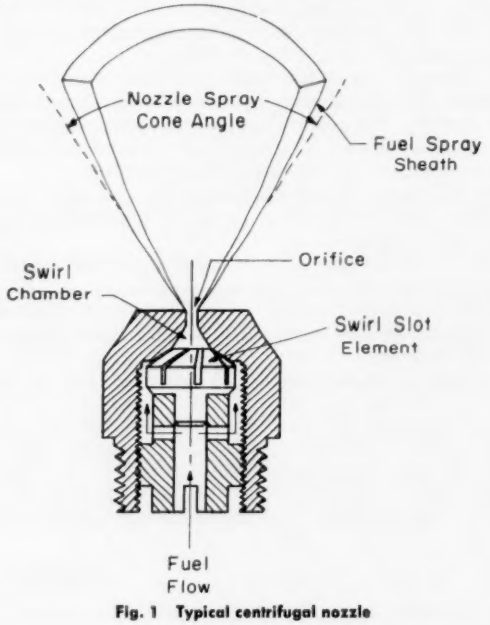

Fig. 1 Typical centrifugal nozzle

[1] Numbers in brackets designate References at end of paper.

Contributed by the Gas Turbine Power Division and presented at the Gas Turbine Power Conference and Exhibit, Cincinnati, Ohio, March 8–11, 1959, of THE AMERICAN SOCIETY OF MECHANICAL ENGINEERS.

NOTE: Statements and opinions advanced in papers are to be understood as individual expressions of their authors and not those of the Society. Manuscript received at ASME Headquarters, December 31, 1958. Paper No. 59—GTP-3.

II Description of Method and Apparatus

The method utilized to obtain drop size will be briefly described here. In reviewing the techniques that have been utilized for drop-size studies, it was seen that no one method had been developed to the point where it had overpowering advantages over other techniques. Consequently the choice of method has depended on the objective at hand. One might list a set of characteristics of an ideal method:

a Should not disturb the fuel spray pattern or atomization.
b Should provide a rapid means of sampling.
c Should provide a rapid means of counting the samples obtained.
d Should have good size distinction over the whole range of drop sizes to be measured and diameter size intervals should be small enough to provide meaningful data in the less than 50μ range.
e Should permit the variation of (*a*) liquid and (*b*) ambient gas properties.
f Should permit one to obtain drop size distribution in space, i.e., in a given volume of the spray.
g Should permit one to obtain the nozzle drop size distribution produced by the nozzle in a given time.

Since one of the prime objectives was considered to be a study of ambient gas effects, this implied spraying within a sealed tank which could be pressurized or evacuated. Because of this consideration, the photographic method was chosen as a means of extracting data (samples) without having ready access to the tank interior. Thus the primary requisites of (*b*) and (*e*) were met. This method is also strong in categories (*a*) and (*f*). Its major weak point is (*c*), speed in counting, since a manual counting procedure is used. Another weak point (*g*) is that the temporal drop size distribution for a nozzle must be obtained indirectly by consideration of local spray velocities and mass flows.

Existing photographic techniques were found to have two major weaknesses and development work was concentrated on these:

1 Fouling of optical surfaces by spray
2 Uncertainty in depth of field determination

The first problem was satisfactorily solved by developing a dual-shutter system which exposes the optical surfaces for very short intervals so that for one set of photographs (24) the surfaces are exposed a total of approximately 0.12 sec. The second problem which has long been the major drawback of photographic techniques was met by utilizing an optical system which produces diffraction patterns around the drop images on the photographic film. The diffraction theory for Fresnel patterns indicated that the width of the first diffraction ring around the drop image could be used as a criterion for determining the position of drops in the camera field. This procedure was verified experimentally so that a depth of field could be specified for any value of fringe width.

A drawing of all the essential components in the system is shown in Fig. 2. The camera, light source, light source tube, and shutters are located on a common axis. The axis of the nozzle holder is located so that the nozzle axis, with the nozzle at the vertical position (i.e., zero degrees) will pass through the camera axis at the location of the plane of best focus.

The nozzle holder has a worm and gear arrangement which allows the nozzle (A) to be rotated about an axis which passes through the nozzle tip and is perpendicular to the nozzle axis and the camera axis. With the tank under pressure, by rotating nozzle positioner (B) to a particular setting of a graduated dial the nozzle may be inclined at any desired angle between zero and 56 deg. θ is the angle between the nozzle axis and the vertical as shown in Fig. 2. The nozzle could be set at any one of several heights above the camera axis by choice of the extension (C).

The optical path may be traced along the camera axis as follows. The light originates at the Xenon flash tube (E) and proceeds through an adjacent pinhole and condensing lens (F). Thence the path is through the window (G), light tube (H), light shutter (I), shield tubes (J), and fuel spray camera shutter (K), camera window (L), lens (M), post camera grid (N), ending at photographic film (O).

The camera lens (M) is threaded into the tip of the conical section of the camera and in front of the lens is a plexiglas window which is held against a flange thus forming a pressure-tight seal. The compound lens is 1.25 in. in diameter and has a focal length of 3.5 in. At the back of the camera a wire grid is installed directly in front of the film holder. This grid is made up of 0.0005-in-diam wire and produces a fine-lined silhouette on each photograph which assists greatly in the counting procedure.

It was found that suitable photographs could not be obtained when any light-transmitting surfaces were exposed to impingement of spray particles. Allowing fuel to completely wet these optical surfaces was not satisfactory because of the variation in thickness of the fuel film as particles impinged on it. This difficulty led to the use of a shielding system consisting of two Alphax shutters, one on the camera side (K) and one on the light side (I). These shutters are of standard leaf type with strengthened spring action to overcome the surface tension forces of the fuel wetting the leaves. By setting the shutter diaphragms down to approximately 0.4 in. in diameter and for a shutter exposure time of $^1/_{200}$ second, it is possible to obtain a set of 24 or more photographs without cleaning of the exposed optical surfaces. The total exposure time of the optical surfaces for 24 photographs is then 0.12 sec. Also this allows unlimited time for steady spray conditions to be reached, while the shutters remain closed. The shutters are tripped simultaneously from outside the tank by action of a solenoid-operated valve which supplies gas pressure to a cylinder-piston arrangement, Fig. 2 (P), within the tank. The light source is flashed by the synchronizing contacts of one of the shutters, through the synchronizing cable, Fig. 2 (Q).

Under certain spray conditions the spray is so dense that additional shielding is needed to reduce the length of the illuminated path in the spray in order to obtain satisfactory photographs. Two tubes approximately $^1/_2$ in. in diameter are used for this purpose, being attached to the shutters, see (J) in Fig. 2. Between the tubes a gap remains through which the spray passes. At the end of each of these shield tubes is a thin projection which prevents particles which bounce on the tube from being carried down into the gap. In obtaining some of the earlier data this shielding was accomplished by two truncated conical sections held between the shutters. To reduce recirculation and bouncing of the fuel drops from the tank and camera walls, matting was used as shown in Fig. 2 (R).

The spray tank has an inside diameter of 18 inches and the height of the portion shown in Fig. 2 from flange to flange is 30 inches. Below the section shown in Fig. 2 is additional tank volume. The optical effects of distortion of the plexiglas camera and light windows, Fig. 2 (G), (L), due to varying tank pressure, were found to be negligible in the range of 0.5 to 114.5 psia. This was checked by examining photographs of a ronchi grating taken at various tank pressures. The camera, light source, and nozzle holder flanges are all doweled to the tank to insure that proper alignment is maintained.

The fuel system and gas system for pressurizing the tank are essentially the same as described in reference [7].

In taking photographs of the spray it is desirable to know the fuel flow-rate distribution in space as a function of θ (nozzle angle) and R (the distance between nozzle tip and camera axis). To obtain this distribution an open-end sampling tube is placed

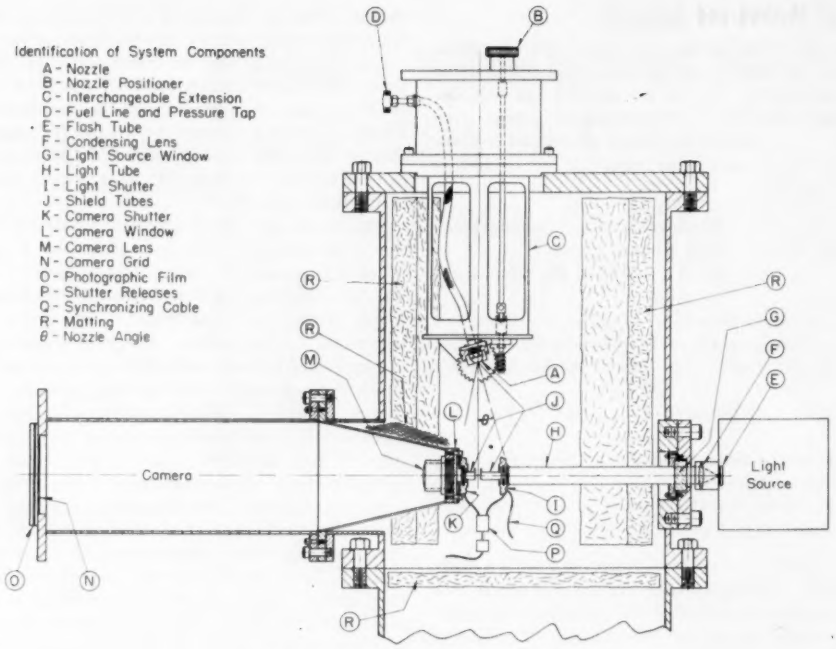

Fig. 2 Drawing of drop-size apparatus

vertically directly below the nozzle with its tip at the camera axis. The flow distribution is then obtained by rotating the nozzle (varying θ) and recording the flow into the sampling tube for timed intervals in the manner described in reference [7]. Once the flow-rate distribution is known, considerable time is saved by photographing only regions where the flow rates are not negligible. The flow-rate distribution is also required in order to obtain values of spray-stream velocity which are necessary for converting the space drop-size distribution into a temporal value, that is, the distribution produced by the nozzle in a given interval of time.

Eastman Kodak Contrast Process Ortho film in the 4 × 5-in-sheet size is used to obtain the drop photographs. For this film the manufacturer gives a resolving power of 145 lines/mm. On the basis of a camera magnification of 9.12 this resolving power in relation to the object photographed is 1320 lines/mm or 1.32 lines/μ. The film has a light sensitivity only in a fairly narrow band in the blue-green region of the spectrum.

The illumination for the photographs is produced by the discharge of capacitors across a Xenon-filled quartz tube. The light source was adapted to give either of two duration times, 2 or 5μ-sec, with the shorter flash having less intensity.

Drop sizes were tabulated by an operator who examined the negatives on an optical comparator at a magnification of 20/1, thus providing an over-all magnification of 182/1. A vexing problem which arises in the counting procedure is the question of how many drops must be counted before one can be assured that he has an accurate representation of the drop-size distribution for any given set of physical conditions. The procedure used was to apply the t-test familiar in statistics considering each negative as an individual sample of the spray drop population. The application of the t-test to obtain confidence limits is similar to the technique using the standard normal distribution but is applicable for small samples. The t-test is applied to obtain confidence limits on the mean of the drop volume found in each sample (i.e., each negative). The drop volume is the pertinent quantity of interest which is most sensitive to changes in drop diameter determination and hence it was chosen as the quantity to be used in the t-test. It occurs in the determination of the Sauter Mean Diameter (S.M.D.) which is of interest in combustion applications. The S.M.D. $= \Sigma n_i d_i^3 / \Sigma n_i d_i^2$ where d_i refers to the drop diameter and n_i is the number of drops found of that size. The drop count from each negative is tabulated in histogram form, the size intervals being 5μ. From these histograms, then, any required characteristic diameter can be calculated and cumulative volume or number curves can be plotted.

The operator who does the drop counting in any photographic method has to make decisions on which drops to count, i.e., decide which drops are outside a predetermined depth of field. It is known that an operator counting drop images that appear to have the same degree of sharpness will count large drops over a greater depth of field than will be covered for the count of smaller drops, thus giving a count biased toward the large drops. Manson, et al., [8], carried out a calibration to correct this effect and found that in going from drop diameters of 12.5 to 150μ the depth of field over which drops were counted varied from 3.7 to 8 mm. York and Stubbs [9] compensated for this effect by the use of images of varying diameter having standard sharpness which an operator could compare with the drop images being counted. In our development work it was found that the formation of Fresnel rings or fringes around a drop image could be utilized to provide a measure of the location of the drop in the field. The width of the first fringe was then used as a criterion for deciding whether the drop should be counted. The essential elements needed to produce Fresnel diffraction patterns are a point source of monochromatic light, an obstacle, and a screen; or, if white light is used, the screen must be receptive only in a narrow band of the spectrum. The latter is the case with the system used here. The receiving screen, which is actually the film, receives the image formed at the plane of best focus. When an obstacle is located on the light-source side of this plane, a real fringe pattern is formed at the plane; when the obstacle is located between the plane and camera, a virtual pattern is formed at the plane. By use of diffraction theory the Fresnel diffraction patterns were calculated for several cases of interest. In addition, comprehensive calibration

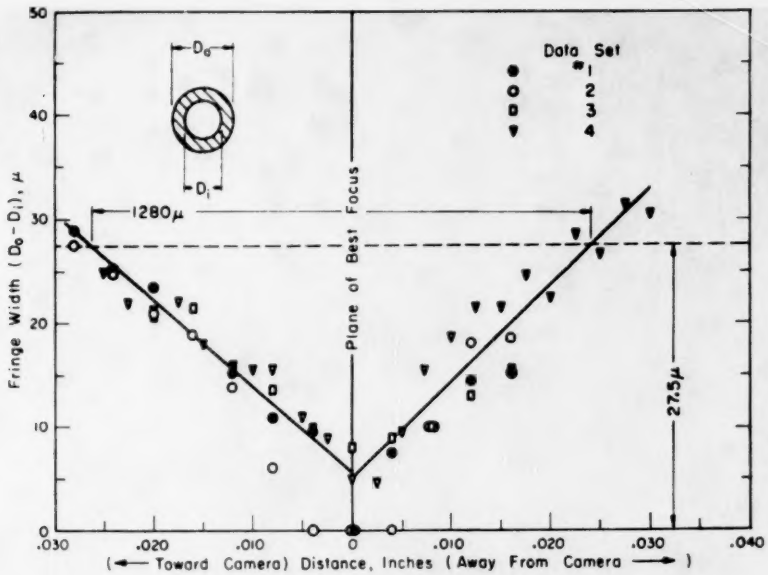

Fig. 3 Fringe width versus drop location in field

work was done over a drop size range of 35 to 500μ using opaque circular spots and fuel droplets suspended on fine wire. This calibration work resulted in the curve of Fig. 3 which shows the fringe width as a function of distance from the plane of best focus. If it is desired to count drops over a depth of field of 1280μ, for example, then all drops having a fringe width of 27.5μ or less would be counted. Fig. 4 is a print of a negative taken of an actual spray, with the fringes clearly visible around the drops.

The Rayleigh limit of resolution for the shutter-camera system was calculated to be 3.1μ. This is a limit imposed by diffraction at the lens aperture. Calibration work with fine-lined reticles and diffraction gratings indicated an actual resolution limit of 3 to 4μ. One should be mindful of this limit in assessing the accuracy of the system.

On the calibration work which preceded the spray photography, it was found that the camera magnification factor for droplet or spot photographs was greater than the nominal value of 9.12 by amounts which ranged from 10 per cent for 5–10μ size to 0.5 per cent for the 500μ size. While this represented small absolute changes in measured drop size, corrections could be easily incorporated into the counting procedure, and this was done.

III Results of Drop-Size Experiments

The system used to identify a particular spraying condition can be illustrated by this example. The notation 45/80°|25|14.5|35° denotes the following situation: A nozzle rated at 45 gal/hr flow (on diesel fuel at 100 psi Δp) and of nominal spray angle equal to 80 deg, spraying at a fuel pressure drop of 25 psi into gas which is at a pressure of 14.5 psia, with the nozzle inclined at an angle θ = 35 deg. Fig. 2 shows the angle θ.

The quantities of interest (m, $\bar{a}_v$, u, S.M.D., N) are tabulated for various values of θ in Table 1. In addition, m, u, and S.M.D. are plotted versus θ in Fig. 5 and Fig. 6. Some explanation of these quantities is needed. The quantity m represents the volumetric fuel flow rate at some point in the spray stream and is obtained by the sampling tube procedure previously described. The quantity $\bar{a}_v$ represents the average over the photographs counted of the total volume of fuel drops in a photograph of standardized size (10 in.^{2}), for some given spraying condition. Since the depth of field is known and the area of the photograph is fixed (10 in.^{2}), this represents the fuel volume in a given space volume (obtained essentially instantaneously) at some chosen point in the spray. The quantity u is the velocity of the droplet stream. This can be obtained once the following four quantities are determined: m; $\bar{a}_v$; A_T = cross-sectional area of sampling tube = 0.170 cm^2; V_s = space volume represented by one standard photograph. This latter quantity, V_s = area of photograph × depth of field/(camera magn)^2. The depth of field is 1280μ, camera magnification is 9.12, and photograph area = 10 in^2. Thus V_s is found to be 0.0993 cc. From these:

$$u = 0.000547 \frac{V_s}{A_T} \frac{m}{\bar{a}_v} \text{ (ft/sec)}$$

or

$$u = 32.0 \times 10^{-6} \frac{m}{\bar{a}_v}$$

where m is in cc/min and $\bar{a}_v$ is in cc. The next quantity in Table 1, S.M.D., refers to the Sauter Mean Diameter of the spray, a characteristic diameter of special value in combustion applications. The S.M.D. is the diameter of a drop which has the same ratio of volume to surface area as that of the actual spray itself. It is determined from the drop count and is equal to a summation over the spray of $\Sigma n_i d_i^3 / \Sigma n_i d_i^2$, where d_i refers to the drop diameter and n_i is the number of drops found of that size. As shown in Table 1 and in Figs. 5 and 6, S.M.D. represents an instantaneous or space distribution of fuel drop size without regard to the mass flow of fuel at any point. The distance between the nozzle tip and the camera axis for the data presented is 7.24 inches. The last quantity shown in Table 1 is N, the drop number density, given in number of drops/in^3.

Several points of interest appear in Figs. 5 and 6: (1) The shift of fuel flow distribution with changing ambient pressure is again evident as was pointed out in reference [7]; (2) except for the 45/80°|100|114.5 case, there is a decided decrease in drop size at the inner portions of the spray. Thus a segregation of particles appears to be taking place. This process may be attributed to the same induced ambient gas crossflow which causes the

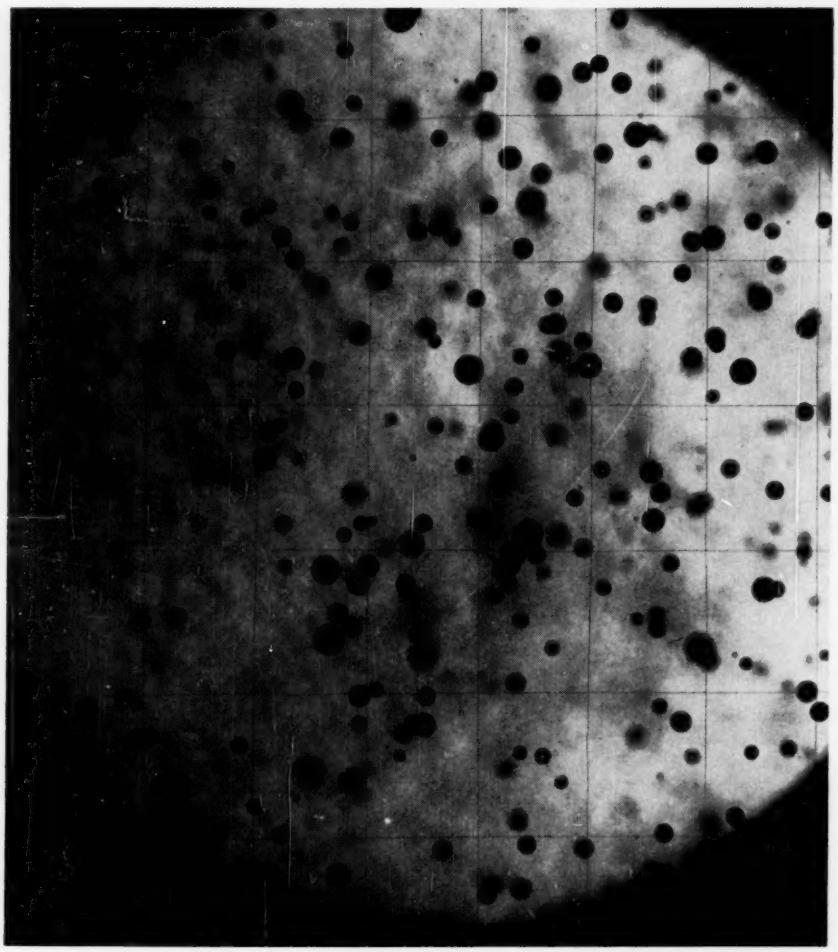

Fig. 4 Print of spray photograph

Table 1 Spray variables

45/80° nozzle, 25 psi, fuel Δp

Tank pressure, psia	0.5	14.5			114.5			
θ, deg	44.5	28.5	35	41.5	3.75	11.25	18.75	26.25
m^*, cc/min	1.95	0.334	0.835	0.366	0.47	0.9	1.29	0.5
$\bar{a}_s$, cc $\times 10^{-4}$	0.563	0.0753	0.144	0.855	0.80	1.51	6.26	3.85
u, ft/sec	11.1	14.2	18.5	1.37	1.88	1.91	0.66	0.42
S.M.D., μ	206.5	90.8	164.5	196.5	101	170	229	247
N, no. drops/in.^{3}	25820	31550	10940	4600	2130	3330	1860	1520

45/80° nozzle, 100 psi, fuel Δp

Tank pressure, psia	0.5			14.5					114.5		
θ, deg	38.5	41.5	44.5	12	24	30.5	35.5	40.5	2.5	7.5	12.5
m^*, cc/min	1.10	3.8	1.5	0.4	0.6	1.05	2.6	0.65	19.0	12.0	2.65
$\bar{a}_s$, cc $\times 10^{-4}$	0.0865	0.395	0.260	0.22	0.468	0.553	0.639	0.218	1.70	1.875	2.50
u, ft/sec	40.6	30.8	18.45	5.8	4.1	6.1	13.02	0.954	35.8	20.5	3.39
S.M.D., μ	57.0	149.6	104.5	40.7	54.0	80.7	94.9	72.3	103	114	108.4
N, no. drops/in.^{3}	131800	228000	96200	48900	51000	32270	75520	6370	18990	26550	11650

* m values obtained from m versus θ curve.

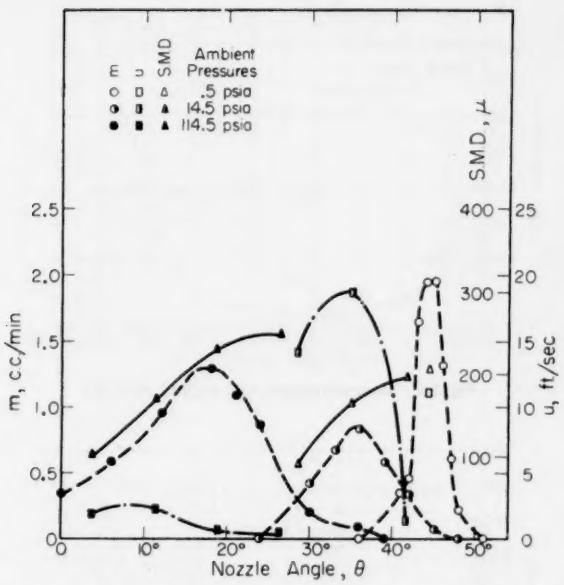

Fig. 5 S.M.D., m, u versus nozzle angle, θ, (25 psi Δp)

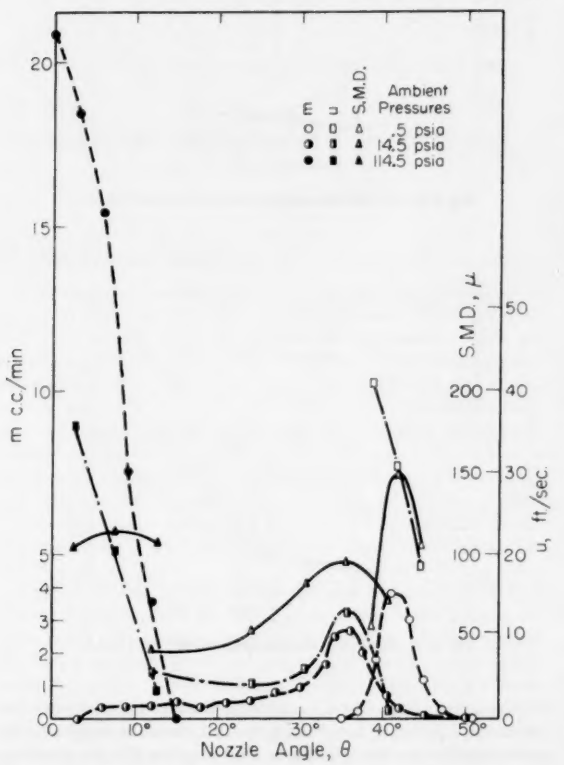

Fig. 6 S.M.D., m, u versus nozzle angle, θ, (100 psi Δp)

spray flow pattern to close in as tank pressure is increased. This segregation of particles was also noted by Manson, et al. [8]; (3) there is considerable variation of stream velocity across the spray. In particular note the increase in velocity at the 114.5 tank pressure condition as θ decreases, i.e., as one moves toward the center of the spray. At the atmospheric condition (14.5 psia) the maximum velocity values coincide with the peaks in the flow-rate curves. The maximum velocity for the 45/80°|100|0.5 case would appear to be located inside the flow-rate peak. Since photographs were obtained for only one value of θ, no u or S.M.D. curves can be drawn for the 45/80°|25|0.5 condition.

The S.M.D. values of Table 1 and Figs. 5 and 6, as stated previously, represent measures of the drop size existing at various points in the spray. As opposed to this, a second type of S.M.D. value may be obtained which represents the total drop output of the nozzle, for any given spraying condition. This is obtained from the data on hand by weighting the numerator and denominator of the spatial S.M.D. values by the stream velocity at the sampling point and by a representative stream-flow area for that sampling point. If we denote the spatial S.M.D. value for a particular spraying condition and value of θ, as

$$\text{S.M.D.} = \frac{\bar{a}}{\bar{b}}$$

then the "nozzle" S.M.D. is

$$(\text{S.M.D.})_N = \Sigma u_i A_i \bar{a}_i / \Sigma u_i A_i \bar{b}_i$$

which is summed up for the number of sampling points (i.e., θ — values) at any spray condition. A_i is the representative flow area at θ_i. The u-weighting accounts for the velocity variation in the spray stream and the A-weighting the variation of flow area as different rings or bands of the spray stream are considered. The flow areas, A_i, are taken to be ring-shaped portions of a sphere of radius R (where R = distance from nozzle tip to camera axis). The area which includes the $\theta = 0$ point would be a spherical segment. When these calculations are carried out the following values of $(\text{S.M.D.})_N$ result:

Table 2 $(\text{S.M.D.})_N$ values

Tank pressure (psia)	0.5	14.5	114.5
Fuel Δp, 25 psi	206.5μ	150μ	213μ
Fuel Δp, 100 psi	106.6μ	75.2μ	109.9μ

These values are plotted in Fig. 7. The striking thing here is the increase in size indicated in going from 14.5 to 114.5 psia ambient pressure. From the aspects of spray breakup a continuing decrease in drop size with increasing ambient pressure would be expected, since the drag force on a drop increases with increasing density. Thus as ambient pressure rises, a decrease would be expected in the critical drop size, i.e., the maximum size that can withstand breakup as is indicated by Hinze [10] and Lane [11]. The explanation for the anomalous increase in drop size of Fig. 7 may lie in increased coalescence of the spray droplets as the ambient pressure is increased.

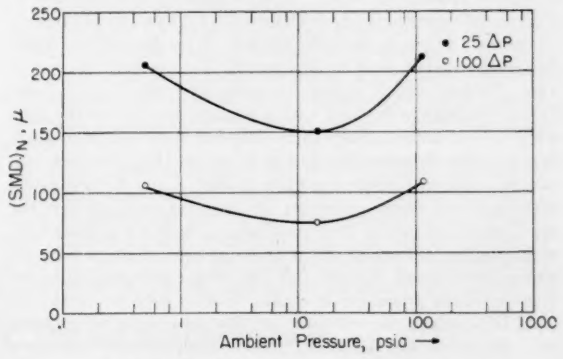

Fig. 7 $(\text{S.M.D.})_N$ versus ambient pressure

It can be seen from the flow distribution curves of Figs. 5 and 6 and from the curves of reference [7] that the action of the induced gas flow is such as to increase the probability of drop collisions especially at the higher ambient pressures where the fuel spray has been collapsed into a small volume. It appears reasonable to postulate that the curve shapes in Fig. 7 result from the following processes operating simultaneously. In the breakup process, increased ambient pressure tends to produce smaller drops. But the coalescence of drops also is increasing and becomes dominant in going from 14.5 to 114.5 psia in pressure.

A considerable effect of drop coalescence is reported by Dunskii [12] for the case of an air-atomizing nozzle. He also finds analytically the change in drop size distribution for orthokinetic motion of a system of drops which move through a gas with different velocities. Turbulence or crosswise gas flow is not considered.

The accelerating force necessary to make a drop travel along a circular arc toward the center of the spray is

$$F_a = \frac{\pi}{6} d^3 \rho \frac{u^2}{r}$$

and the drag force exerted by induced gas flow, in the same direction as F_a, is

$$F_d = \frac{1}{2} C_d \rho_g u_g^2 \left(\frac{\pi d^2}{4}\right)$$

Here d = drop diam, ρ = fluid and ρ_g gas density, u = drop velocity, r = radius of curvature of path, u_g = gas velocity relative to drop in direction of F_a, C_d = drag coefficient based on u_g. Then

$$F_d/F_a = \frac{3}{4} \frac{\rho_g}{\rho} C_d \left(\frac{u_g}{u}\right)^2 \frac{r}{d}$$

From this it can be seen that the dependency of this ratio on d will vary essentially from $1/d^2$ to $1/d$ depending on whether C_d is evaluated for laminar or turbulent flow. Thus the smaller the drop the more susceptible it is to entrainment toward the nozzle axis, which is borne out by the data obtained.

Various experiments have fitted data to the expression $(\text{S.M.D.})_N = KP^x$ at some constant value of ambient pressure (usually atmospheric). Here K = a nozzle constant and P is the fuel pressure drop. Although only two points are available at each tank pressure yet it is of interest to find the values of x for the data of Fig. 7. These are, for tank pressures of 0.5, 14.5, and 114.5 psia, $x = -0.48$, -0.50, and -0.45, respectively.

The data in this paper are based on a count of 31,375 drops. The drop size distributions obtained are presented in the form of curves of cumulative per cent under size by number plotted on arithmetic probability paper. These are shown in Figs. 8 and 9. A normal distribution of drop size would plot as a straight line on this paper. Attempts were also made to fit the data to the Rosin-Rammler equation and the log-normal distribution, but curves were obtained which varied considerably from straight lines. The advantages of working with a straight-line plot of the data are great but unfortunately spray drop-size data seldom conform to any of the drop-size distribution functions that have been advanced. For each spray condition in Figs. 8 and 9, a combined curve is shown which represents the drop-size distribution of the total nozzle output at that condition. These are obtained by weighting the individual distributions at each value of θ by the appropriate stream velocity and flow area corresponding to the θ-value. This procedure is similar to that used to obtain the $(\text{S.M.D.})_N$ values, the velocities and flow areas used being identical. Of course, for the 45/80°|25|0.5 condition only one curve appears because only one sampling point was used. Many of the

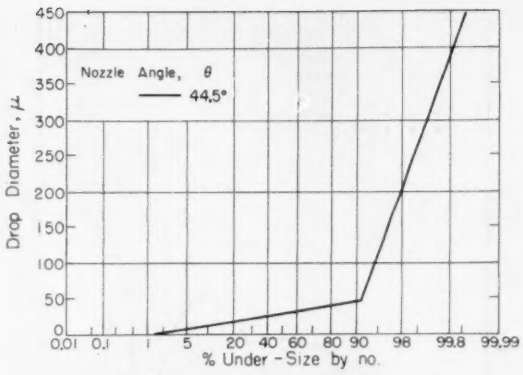

Fig. 8(a) Drop-size distributions 45/80°|25|0.5

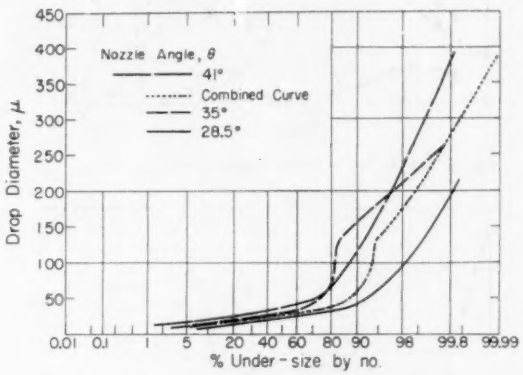

Fig. 8(b) Drop-size distributions 45/80°|25|14.5

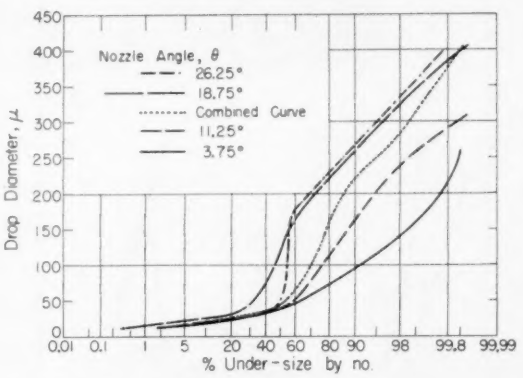

Fig. 8(c) Drop-size distributions 45/80°|25|114.5

distributions in Figs. 8 and 9 and, in particular, the combined distributions, appear to be of the type that could be satisfactorily represented by two straight lines. This suggests that the atomization process is occurring in such a way as to produce the sum of two distinct distributions. Fig. 10 is drawn to show how curves of the type seen in Figs. 8 and 9 can occur as the sum of two normal distributions, possibly added in varying proportions. The normal distributions used in Fig. 10 are one of mean = 30, standard deviation = 10, and one of mean = 100, and standard deviation = 100. These are designated as (30, 10) and (100, 100).

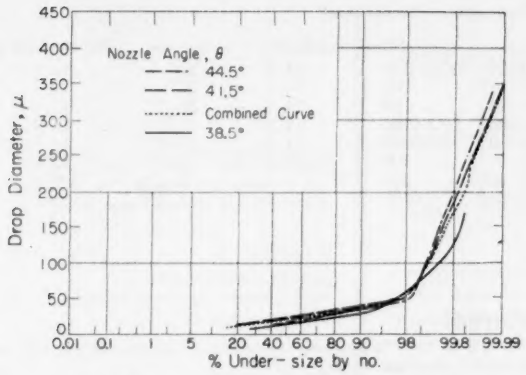

Fig. 9(a) Drop-size distributions 45/80° | 100 | 0.5

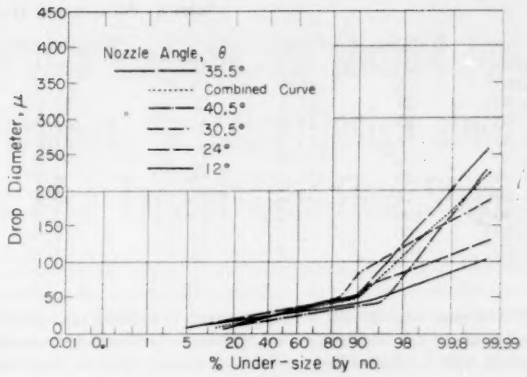

Fig. 9(b) Drop-size distributions 45/80° | 100 | 14.5

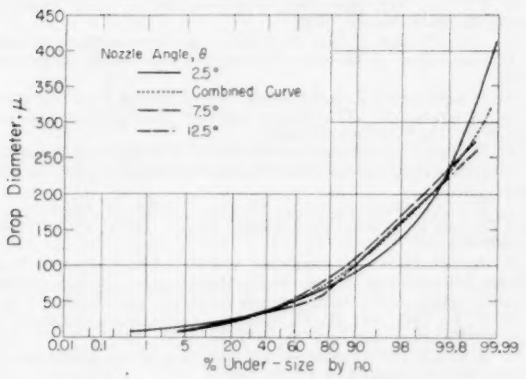

Fig. 9(c) Drop-size distributions 45/80° | 100 | 114.5

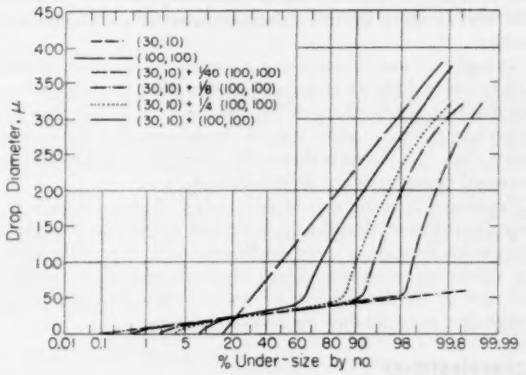

Fig. 10 Combined normal distributions

IV Discussion of Errors

A discussion of possible errors in the results presented is in order. When sampling from a particle stream is attempted there exists the danger that the sample will be biased. Here the sampling structure can be considered as a cylinder with a section sliced out so that the sample passes down through the cutout section, see (J) Fig. 2. The available information dealing with flow around solid objects indicates that a decrease in sampling efficiency occurs as: (1) Flow velocity decreases; (2) sampling structure size increases; (3) as drop size decreases. Of secondary importance is the decrease in sampling efficiency as the ambient pressure increases. Keeping these effects in mind, no trend in the drop size results was discerned which could be attributed to sampling error.

A second source of error arises in the calculation of the fuel volume per spatial volume, which in turn affects the stream velocity value. This is due to an "edge effect" arising from the fact that drops at the edge of the sample volume (i.e., just barely within the depth of field) will have a varying amount of volume projecting outside what is considered to be the sample space or sample volume. Since all the drops counted are considered to be within the sample space, it is seen that an error is present which would increase as the drop size encountered increases and as the depth of field is decreased. This error has been found to be a linear function of depth of field and drop diameter. For the depth of field of 1280μ, the calculated error goes from zero at drop diameter = 0 to 7 per cent at 500μ. Because application of this correction would be rather difficult and because of its limited size, the correction was not applied in the calculation of stream velocity. However, it is essential to establish its magnitude and, if a smaller depth of field is specified, the correction might have to be considered.

For any given spray condition, $\bar{a}_v$ represents the mean of the total drop volumes per sample (negative). $\bar{a}_v$ figures in the calculation of stream-velocity and thus in the $(S.M.D.)_N$ values. The deviation of the sample mean $\bar{a}_v$ from the actual mean volume can only be estimated. The statistical procedure is first to assume some distribution function for the quantity to be evaluated, which in this case is the drop volume per negative. For the t-test a normal distribution is assumed. The expected error at any chosen confidence level is then a function of the size of the sample and the scatter of the individual a_v values. In our case the size of sample refers to the number of negatives counted. The S.M.D. accuracy also depends on the magnitude of the drop count but to a lesser extent than $\bar{a}_v$ since the S.M.D. value is not as sensitive to variations in the number of drops occurring in individual negatives. The percentage errors in the $\bar{a}_v$ or $\bar{a}$ figures are listed in Table 3, calculated at the 95 per cent confidence level, according to the t-test.

A review of the change in per cent error at each condition as the sample size was increased indicates that the figures of Table 3 are on the pessimistic side. The stream velocity figures would be most affected by any variations in $\bar{a}_v$. In the calculation of $(S.M.D.)_N$ any variation in $\bar{a}_v$ would be partially compensated by a corresponding opposite variation of the local S.M.D. value.

V Additional Discussion of Results

Some implications of this work will be presented here. From

Table 3 Per cent error in $\bar{a}_r$ at 95 per cent confidence level

Spray condition				Per cent error	Spray condition				Per cent error
45/80°	25	0.5	44.5°	21.8	45/80°	100	14.5	12°	18.2
45/80°	25	14.5	28.5°	39.5	45/80°	100	14.5	24°	32.2
45/80°	25	14.5	35°	29.0	45/80°	100	14.5	30.5°	11.3
45/80°	25	14.5	41.5°	42.0	45/80°	100	14.5	35.5°	14.7
45/80°	25	114.5	3.75°	31.8	45/80°	100	14.5	40.5°	16.8
45/80°	25	114.5	11.25°	46.5	45/80°	100	114.5	2.5°	15.6
45/80°	25	114.5	18.75°	8.7	45/80°	100	114.5	7.5°	29.4
45/80°	25	114.5	26.25°	15.4	45/80°	100	114.5	12.5°	20.3
45/80°	100	0.5	38.5°	42.3					
45/80°	100	0.5	41.5°	40.0					
45/80°	100	0.5	44.5°	42.2					

the drop-size segregation which occurs it is evident that photographs of a spray which show only the outer portions of the spray stream will be misleading and will generally give a drop size measure larger than the actual. An appreciable coalescence of drops has been postulated to occur in these sprays. If this is the case then any drop-measuring methods which prevent or hinder this effect (such as the molten-wax method) should be used with caution.

At high fuel and ambient gas pressures the coalescence effect appears to be fully as important as the spray breakup process and deserves increased study. For example, this effect may help to explain the well-known increase in drop size as the nominal spray angle of a nozzle is decreased, since this decrease provides increased opportunity for drop collisions.

Translated into the area of combustion chamber design, it is hoped that this work will help to explain anomalous behavior of combustion systems as spray conditions vary. Also with increasing knowledge of environmental effects on sprays, the designer will have at hand additional necessary tools for rational design and scaling of liquid-fired combustion systems.

Acknowledgment

I wish to acknowledge the assistance of Mr. A. T. Pieczynski who performed the photographic and darkroom work and assisted on other aspects of this study. I am also indebted to Mr. A. Montali who assisted with the drop counts and calculations.

References

1 D. W. Lee, "Fuel-Spray Formation," TRANS. ASME, vol. 54, 1932, OGP-54-4, pp. 63–73.

2 D. W. Lee, "The Effect of Nozzle Design and Operating Conditions on the Atomization and Distribution of Fuel Sprays," NACA Report No. 425, 1932.

3 F. Sass, "Kompressorlose Dieselmaschinen," Julius Springer Verlag, Berlin, Germany, 1929.

4 Alfred Woltjen, "Über die Feinheit der Brennstoffzerstaubund in Oelmaschinen" Technische Hochschule, Darmstadt, Germany, 1925.

5 E. Giffen and T. A. J. Lamb, "The Effect of Air Density on Spray Atomization," The Motor Industry Research Association Report No. 1953/5 (Great Britain).

6 R. Retel, "Contributions à l'Etude de l'Injection Dans les Moteurs Diesel," Min. de l'Air (France) Bull. Serv. Techn. No. 81, 1938.

7 S. M. DeCorso and G. A. Kemeny, "Effect of Ambient and Fuel Pressure on Nozzle Spray Angle," TRANS. ASME, vol. 79, 1957, pp. 607–615.

8 N. Manson, S. K. Banerjea, and R. Eddi, "Dispositif Pour l'Etude Microphotographique de la Pulvérisation de Combustible Liquide," *Revue de l'Institute Français du Pétrole*, vol. X, June, 1955.

9 J. L. York and H. E. Stubbs, "Photographic Analysis of Sprays," TRANS. ASME, vol. 74, 1952, pp. 1157–1162.

10 J. O. Hinze, "Critical Speeds and Sizes of Liquid Globules," *Applied Science Research*, A-1, 273, 1948.

11 W. R. Lane, "Shatter of Drops in Streams of Air," *Industrial and Engineering Chemistry*, vol. 43, p. 1312, 1951.

12 V. F. Dunskii, "On Coagulation During Atomization of a Liquid," *Zhurnal Tekhnicheskoi Fiziki*, vol. 26, 1956, translated in *Soviet Physics-Technical Physics*, vol. 1, 1956, p. 1232.

Presentation of a Blade-Design Method for Axial-Flow Turbines, Including Design and Test Results of a Typical Axial-Flow Stage

F. BAUMGARTNER
Research Engineer, Boeing Airplane Company, Seattle, Wash.

R. AMSLER
Group Engineer, Boeing Airplane Company, Seattle, Wash.
Assoc. Mem. ASME

A method is presented to determine the shape of stationary nozzle blades and rotor blades for an axial-flow-type turbine in a generally consistent manner based on the concept of aerodynamic blade loading. The mean blade load is a typical design parameter which predominantly determines the blade curvature. It depends in particular on the rate of change of momentum across the blade row. By applying the design method, airfoil shapes are obtained which satisfy the momentum requirements regardless of what blade-load distribution is assumed as long as the mean blade load remains constant. A specific application of the design method is described and test data are presented which show that good agreement between design goal and test results was achieved.

EARLY IN THE DEVELOPMENT PROGRAM for small gas turbines, undertaken by the authors' company, the need was recognized for a consistent method to determine the blade shapes in turbines and compressors of axial and radial-flow type. The method had to be complete enough to define the correct blade shape uniquely for any given application, yet it had to be clear and simple enough to permit the average turbine designer to evaluate the basic problems involved without applying complicated mathematical procedures or incomprehensible experience factors. It appeared to be desirable to combine experimentally determined blade-design information with a simple mathematical formulation of the flow problem to obtain a clear picture of the flow pattern.

Extensive testing by the authors' company on airfoil cascades furnished some basic information on pertinent design parameters such as blade loadings, angles of incidence, blade-overturn angles, pitch-chord ratios, aspect ratios, and so on. The flow problem was formulated according to the classical fluid-dynamics theory. The derivation of the basic flow equations is given in Appendix II. These equations, together with empirically established design parameters, may be used to calculate the blade profiles for turbines and compressors of either axial or radial-flow type. Detailed procedures to cover all these specific applications of the same basic theory have been worked out and used successfully by the authors' company. Applying such a strict mathematical treatment to the three-dimensional compressible-flow pattern of a radial-type turbine or compressor involves, of course, a more complicated procedure than applying it to a two-dimensional flow pattern of axial-flow-type turbines and compressors.

It should be mentioned here that the same analytical approach to blade-shape calculations has been used by other designers. A notable example is presented in a paper by Concordia and Dowell,[1] where development work on impellers for centrifugal air compressors is described.

In the following discussion we shall limit ourselves to the case of the axial-flow-type turbine.

Description of Method

Before the blading design for any particular turbine stage can be started the basic design parameters must be established. First, the flow rate must be determined, based on power output, turbine-inlet conditions, turbine-exit conditions, and expected over-all stage efficiency. Next, an appropriate flow pattern is selected. For theoretical considerations, a free-vortex flow pattern is usually selected because it requires the least amount of kinetic energy for a given flow rate and therefore represents the most stable flow condition. In a free vortex the tangential-velocity components of the stream particles are inversely proportional to their radial distance from the center line and the axial-velocity components are constant across the whole flow area. A free-vortex flow pattern is maintained across the rotor if equal amounts of work are taken out at any radius station.

Contributed by the Gas Turbine Power Division and presented at the Gas Turbine Power Conference, Cincinnati, Ohio, March 8–11, 1959, of THE AMERICAN SOCIETY OF MECHANICAL ENGINEERS.

NOTE: Statements and opinions advanced in papers are to be understood as individual expressions of their authors and not those of the Society. Manuscript received at ASME Headquarters, December 31, 1958. Paper No. 59—GTP-4.

[1] C. Concordia and M. F. Dowell, "Analytical Design of Centrifugal Air Compressors," *Journal of Applied Mechanics*, vol. 13, TRANS. ASME, vol. 68, 1946, p. A-271.

Nomenclature

r = radial co-ordinate, ft
z = axial co-ordinate, ft
ϕ = angular co-ordinate, radians
y = $r\phi$, circumferential co-ordinate, ft
ω = $d\phi/dt$, angular velocity, radians per sec
V_u = $r\omega$, circumferential velocity, ft/sec
α = $d\omega/dt$, angular acceleration, radians/sec^2
$r\alpha$ = dVu/dt, circumferential acceleration, ft/sec^2
U = circumferential velocity of rotor blades, ft/sec
V = absolute flow velocity, ft/sec
W = flow velocity relative to moving blade, ft/sec
p = pressure, lb/ft^2
γ = specific weight, lb/ft^3
ρ = γ/g, specific mass, slugs/ft^3
g = 32.2, gravity acceleration, ft/sec^2
J = 778, work-heat-equivalent, ft-lb/Btu

Subscripts

0 = nozzle inlet
1 = nozzle exit—also rotor inlet
2 = rotor exit
s = static pressure
t = total pressure
rel = relative to moving blades
r = radial direction
u = circumferential direction
z = axial direction

The degree of reaction that can be built into the turbine stage is dictated to a large extent by stress considerations. A high degree of reaction is desirable if the highest possible efficiencies are to be attained. A high degree of reaction, however, requires high blade speeds and causes high rotor stresses. In addition to this, the blade temperatures in the rotor increase with increasing degrees of reaction for any given turbine-inlet temperature. This further aggravates the material requirements. If a maximum power output per stage is desired, then it is necessary to design the blading for zero reaction at the blade-root station to keep the stresses within acceptable limits. Under these conditions about 20 to 30 per cent reaction is obtained at the tip station of a typical small gas-turbine wheel. The best compromise between high power output per stage and high efficiency is usually obtained by designing for about 15 to 20 per cent reaction at the blade-root station, whereby about 50 per cent reaction at the blade-tip station is obtained.

A typical velocity diagram, a corresponding entropy diagram, and definitions of the most commonly used performance parameters for axial-flow turbines are shown in Appendix I.

After the basic design parameters are established, aerodynamic design of the blading can be started. It should be noted that velocity diagrams usually apply to a mean streamline, located about halfway between two adjacent blades. In the immediate vicinity of the blades, the flow directions will vary to some extent from those of the mean streamline. The deviations of the concave side of the flow boundary from the mean streamline at entrance and exit are defined, respectively, as angle of incidence and angle of overturn. Design information about these angles must be obtained from cascade tests. Fig. 1 gives typical design values as function of pitch-chord ratio.

For practical purposes, it is convenient to arrange the velocity diagram as shown in Fig. 2, where the total velocity change in the tangential direction across the rotor blades is represented by a single vector B. Vector B together with the flow rate determines the momentum change in the rotor and fixes the torque which the gas exerts on the rotor.

If the velocity diagram, Fig. 2, were used directly to determine the shape of the rotor blades, a blade would result that would provide neither an incidence angle at the inlet nor an overturn angle at the exit. The gas would not be turned enough by the blades, the required velocity changes would not be obtained and, as a result, the power output of the turbine stage would fall short of the requirements. To remedy the situation, a corrected velocity diagram is drawn up that takes into account an overturn angle. By doing this, the vector B is increased which means that a larger momentum change is used for the blade design than is needed to satisfy the required power output. This correction would be sufficient for obtaining a blade profile that turns the gas an adequate amount. The gas now would enter the blades without any incidence and the blade load would increase gradually as the gas is turned by the blade. Cascade tests have shown, however, that any given blade chord can be utilized most effectively if the blade loadings are increased fairly rapidly near the inlet by means of a certain incidence angle. This practice results in more uniform blade loadings across the whole blade chord. Fig. 3 shows a desirable blade-load distribution for an axial-flow-type blade which can be obtained by proper selection of basic profile and angle of incidence. Thus the ideal velocity diagram is subjected to a second modification which takes into account a certain incidence angle at the inlet. Figs. 4 and 5 show modified velocity diagrams for nozzles and rotor blades, respectively.

To determine the airfoil shapes of the blades, the general differential equations for the three-dimensional compressible flow

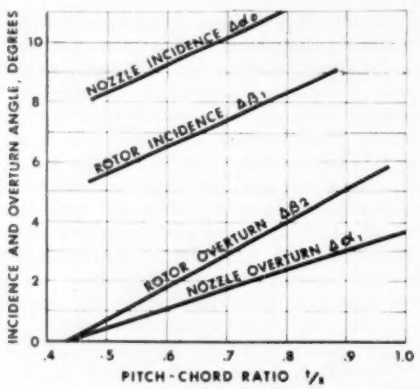

Fig. 1 Typical design values for incidence angle and overturn angle of nozzles and rotor blades, based on cascade tests by authors' company

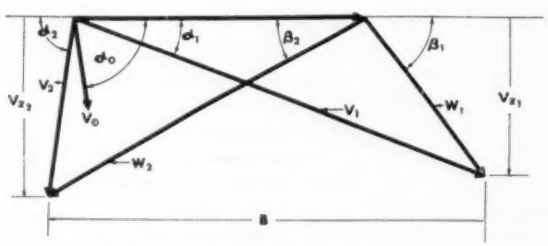

Fig. 2 Typical velocity diagram for axial-flow turbine stage

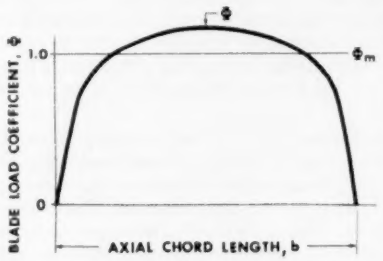

Fig. 3 Typical blade-load distribution for axial-flow turbine blades

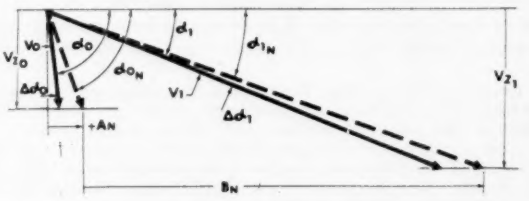

Fig. 4 Nozzle-velocity diagram modified for incidence and overturn

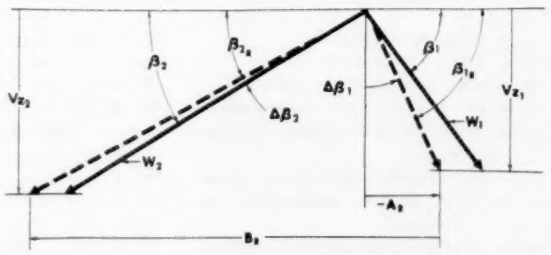

Fig. 5 Rotor-blade velocity diagram modified for incidence and overturn

are used. The derivation of these equations is shown in Appendix II. For convenience these equations are repeated here:

$$-\frac{\partial p}{\partial r} = \rho\left(\frac{dV_r}{dt} - r\omega^2\right)$$

$$-\frac{\partial p}{r\partial\phi} = \rho\left(\frac{d\omega}{dt}r + 2\omega V_r\right)$$

$$-\frac{\partial p}{\partial z} = \rho\frac{dV_z}{dt}$$

For axial-flow turbines the radial velocity V_r may be neglected and the equations can be simplified as follows:

$$\frac{\partial p}{\partial r} = \rho r\omega^2 \tag{1}$$

$$-\frac{\partial p}{r\partial\phi} = \rho\frac{d\omega}{dt}r \tag{2}$$

$$-\frac{\partial p}{\partial z} = \rho\frac{dV_z}{dt} \tag{3}$$

Equation (1) expresses radial equilibrium and may be used to calculate the fluid density at any radius station. Equation (2) is used to calculate the blade shape as explained later, while equation (3) in conjunction with (1) and (2) provides a means for checking the density changes of the gas as it passes through the blades.

Flow rate, gas densities, and velocity pattern determine the required flow areas. Based on the peripheral blade velocities and the flow areas, a first approximation of flow-annulus dimensions and wheel configuration can be made as shown in Fig. 6. The blade-chord length is selected so that satisfactory wheel proportions are obtained and the blade spacing is selected such that pitch-chord ratios below 1.0 are obtained at the outer diameter of the flow annulus. The main feature of the present blade-design method now consists of selecting a suitable airfoil and shaping it into a blade profile such that momentum requirements are satisfied, together with requirements of optimum blade-load distribution, flow rate, and stress. At first sight, this looks like an almost endless task based on trial and error. However, after the method has been applied a few times and the designer has developed a certain feeling for proper blade proportions, the method proves to be quite straightforward, and trial-and-error solutions can be avoided almost completely.

It has been found most convenient to start by selecting a basic airfoil suitable for operation at high subsonic velocities. This airfoil is then shaped into a blade profile such that the tangents to the concave face of the blade satisfy the modified velocity diagram. Fig. 7 shows a typical rotor-blade profile that is obtained with this approximation method. Then the preliminary wheel configuration should be used for a careful stress study to avoid the need for major changes later, after the blade profiles have been calculated in detail

The concave side of the blade profile is now checked according to equation (2), which can be rewritten as follows:

$$-\frac{\partial p}{\rho r\partial\phi} = \frac{d\omega}{dt}r = \frac{dV_u}{dt} = \frac{dV_u}{dz}\frac{dz}{dt} = V_z\frac{dV_u}{dz}$$

The pressure gradient $-\partial p/(r\partial\phi)$ between two adjacent blade surfaces may be assumed to be constant. Therefore, it can be replaced by a constant q/c, where q represents the blade load or the pressure difference between the two blade surfaces, and c is the distance between the two blade surfaces. Solving for dV_u we find

$$dV_u = \frac{qdz}{c\rho V_z} \tag{4}$$

This is the differential velocity increase in circumferential direction over a blade length increment dz measured in axial direction for a given blade load q.

The blade load q must now be determined from the momentum changes as shown in the velocity diagrams Figs. 4 and 5. The total momentum force on the blade area bh, Figs. 6 and 7, can be expressed as

$$Q = \frac{f_m B}{g}$$

where f_m is the mean flow rate for one blade passage of height h. The velocity change B may be obtained from Fig. 4 for the nozzles and from Fig. 5 for the rotor.

The mean flow rate f_m can be calculated from the inlet and exit conditions of the blade. Due to centrifugal forces the flow lines are crowded toward the outside in regions of high circumferential absolute gas velocities. When the gas flows in purely axial direction, the flow lines are uniformly spaced. Because of this slight radial displacement of the streamlines which is caused by changes in flow direction, the flow rate f varies as the gas flows through the blades. For instance, in a nozzle diaphragm which imparts to the gas a considerable amount of whirl, f increases from inlet to exit at the outer shroud, it decreases from inlet to exit at the inner shroud, and remains constant at some intermediate radius station. In the turbine wheel these conditions are reversed because the whirl of the gas stream is reduced to obtain usable work at the rotor shaft. Since the change of f is small from blade inlet to

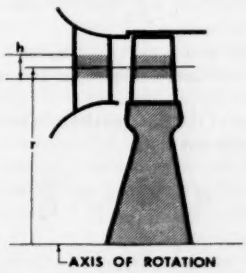

Fig. 6 Typical blading configuration of axial turbine stage

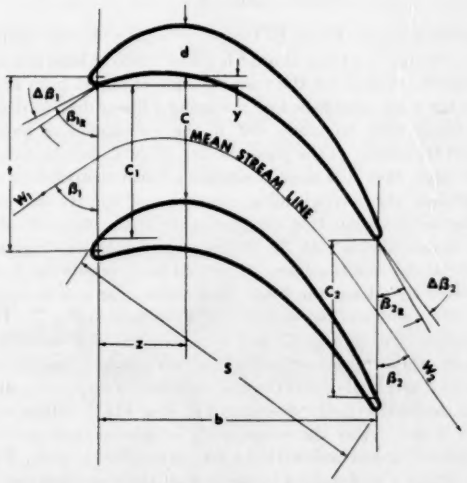

Fig. 7 Typical rotor-blade profiles developed into a flat pattern

blade exit, a linear function may be assumed to establish intermediate values and a mean value of f for any given radius station can be calculated as follows:

$$f_m = \frac{f_1 + f_2}{2}$$

where $$f_1 = V_{u1}\gamma_1 c_1 h$$

and $$f_2 = V_{u2}\gamma_2 c_2 h$$

The mean blade load for a given radius station can be expressed as

$$q_m = \frac{Q}{bh} = \frac{f_m B}{gbh} \tag{5}$$

With the mean blade load fixed, the actual design blade-load distribution can now be established as desired, for example, according to Fig. 3

$$q = q_m \Phi \tag{6}$$

such that the total area under the blade load curve is equal to $q_m b$.

Combining equations (4), (5), and (6), we find

$$dV_u = \frac{f_m \Phi B}{bhc\gamma V_a} dz = \frac{f_m \Phi B}{fb} dz$$

The tangential velocity V_u at any point along the blade chord is obtained by integration:

$$V_u = \frac{f_m B}{b} \int_0^z \frac{\Phi}{f} dz + V_{u0} \tag{7}$$

The initial velocity component V_{u0} is given in the velocity diagrams Figs. 4 and 5 for nozzle diaphragm and rotor as $+ A_N$ and $- A_R$, respectively.

The displacement of the flow particles in the tangential direction within a time element dt is

$$dy = V_u dt = V_u \frac{dz}{V_a}$$

where $$V_a = f/(\gamma ch)$$

and $$y = h \int_0^z \frac{V_u \gamma c}{f} dz \tag{8}$$

Equations (7) and (8) can be integrated with sufficient accuracy in finite steps if the blade chord b is divided into at least ten equal increments. Values for the variable c are obtained from Fig. 7; values for γ are established by assuming a linear drop in density from blade inlet to blade exit if the corresponding pressure changes are small. If the pressure drop from blade inlet to blade exit is large, then it is safer to assume a linear temperature drop to calculate the corresponding pressure and density decrease.

Integration of equation (8) produces the concave side of the blade in accordance with the corresponding velocity diagram at any particular radius station. The final blade profile can now be completed by adding the blade thicknesses d as well as leading-edge radius and trailing-edge radius as assumed in Fig. 7. If the integration of equations (7) and (8) is carried out with sufficient accuracy, then the tangents of the concave side of the blade at blade inlet and blade exit will agree with the corresponding angles of the modified velocity diagrams Fig. 4 or Fig. 5 within a fraction of 1 deg. Also, the value of V_u integrated over the whole blade chord, must check with the vector B_N, Fig. 4, or B_R, Fig. 5.

To obtain a well-defined blade at least three sections per inch of radial height should be calculated. The station closest to the hub should be located above the blade-root fillet so that the blade section can be checked dimensionally. The blade sections, calculated for the various radius stations, may be stacked up along any convenient radial line as long as a continuous blade shape can be obtained by smooth fairing between the calculated sections. For nozzle blades, it is usually advantageous to select as stacking points the centers of all trailing-edge radii. This way, a nozzle blade is obtained with a straight radial trailing edge. For rotor blades, it is most common to select as stacking points the centers of gravity of all sections. With this type of blade construction, blade stresses and danger of vibration are minimized and bending stresses due to centrifugal forces are completely eliminated.

After the general blade shape has been essentially completed, a final stress check is made. If some minor changes in blade thickness are required to satisfy stress requirements, the changes should be made on the convex side of the blade. As a final step it may then be necessary to make some adjustments in over-all radial blade height in order to satisfy flow-area requirements.

It is obvious from the foregoing discussion that a close initial approximation of the final blade shape is essential for successful application of the design method. It was found that even a relatively inexperienced designer was able to obtain a satisfactory blade according to this method after not more than three attempts. An experienced designer usually obtains the best possible blading arrangement in the first attempt with only minor adjustments being required between the initially assumed and the final blade shape.

Application of Method to a Specific Case

The blade-design method just described has been used at the authors' company for many years to design the blading of axial-flow-type turbines. The most recent application was the power output stage of a 400-hp, two-shaft, gas-turbine engine. To present a clearer concept of what can be accomplished with the blade-design method, a more detailed account is given of the design features of this turbine stage.

An ideal free-vortex-flow pattern was selected for the blading. The nozzles were designed for constant pitch-chord ratio at all radius stations. These assumptions resulted in a blade with very little twist and with very similar blade sections from root to tip. Hence it was only necessary to calculate the exact blade contour for the mean radius station. The blade profiles at root and tip stations were obtained by changing all principal dimensions of the calculated blade contour, by the ratio of the respective station radii. The three principal sections were stacked on a radial line connecting the centers of the trailing-edge radii in order to obtain a straight radial trailing edge. The positions of the sections with respect to the turbine axis were determined from velocity diagrams suitably corrected to obtain the desired overturn angles.

Fig. 8 shows a scale view of the three principal sections stacked up as described. The discharge flow area between the nozzles was made about 5 per cent larger than required ideally to account for boundary-layer effects and to assure that the basic design assumption of an unchoked nozzle diaphragm would be achieved.

The rotor blades needed considerably more cross-sectional area change from root to tip to satisfy aerodynamic as well as structural requirements. Safe stresses demanded a considerable area taper from root to tip which resulted in higher pitch-chord ratios and higher overturn angles for the tip station than for the root station. Aerodynamic requirements called for a blade with a considerable amount of twist. With such drastic profile changes it became necessary to calculate the exact blade contour for three radius stations. Blade contours for two additional radius stations were obtained by interpolation. All five blade sections were stacked on a radial line connecting the centers of gravity of the sections. Again the sections were positioned with respect to the

Fig. 8 Principal sections of nozzle for a 400-hp turbine stage

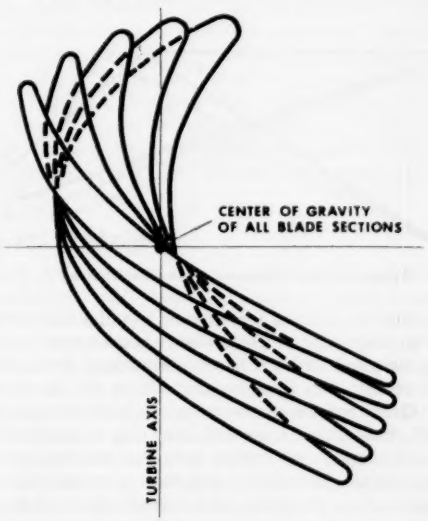

Fig. 9 Principal sections of a rotor blade for a 400-hp turbine stage

axis of rotation according to velocity diagrams suitably corrected for angles of incidence and overturn.

Fig. 9 shows a scale view of all five principal sections stacked in their relative positions. The effective discharge flow area in this case was estimated to be 96 per cent of the physical area. It should be emphasized here that an accurate prediction of the effective flow areas of nozzle diaphragm and rotor is indispensable if the desired degree of reaction in the turbine stage is to be obtained. A high degree of reaction at the tip was desired in this case requiring near sonic gas velocities relative to the blade, yet no choking effect at the blade exit could be tolerated. The physical flow area at the blade inlet proved to be about 10 per cent larger than the required effective area. This may appear to be somewhat too large, but considering that the inflow conditions to the rotor blade are somewhat undetermined because of the wakes from the nozzles, an ample inlet flow area was considered desirable. Moreover, slightly too much area at the blade inlet is not expected to impair the turbine stage efficiency.

The stage efficiency was predicted to be at least 80 per cent on a total-to-static basis and 90 per cent on a total-to-total basis. Enough energy was left in the exhaust gases leaving the stage to raise the total-to-static efficiency to 84 per cent by means of a properly designed exhaust diffuser.

Blade sections and reference co-ordinate systems, established by the aerodynamic designer, were transferred directly to production drawings. The engine designer only had to concern himself with actual manufacturing problems, such as shrink allowances for cast blades, tooling techniques, and methods of attaching the blades to rotor hub or nozzle shrouds. All fairing between the principal stations shown on the production drawings was left up to the pattern maker without further help from Engineering. Very satisfactory blade shapes were obtained with this procedure.

Test Results

A turbine stage according to the design just described was fabricated for performance evaluation in a test rig. Fig. 10 shows the assembled turbine wheel.

The turbine was tested over as wide an operating range as available test facilities permitted. Expansion ratios and velocity ratios ranged from 1.6 to 2.7 and from 0.40 to 0.80, respectively. The design point with an expansion ratio of 2.10 and a velocity ratio of 0.57 lay just about in the center of the whole test range. No exhaust diffuser was used for the test. Figs. 11 and 12 are performance maps calculated from the test data. U_m is the blade speed at the mean radius station between hub and tip.

Fig. 11 shows that the predicted total-to-static stage efficiency of 80 per cent at the design point was exceeded by about 3 per cent. This fact indicates that an aerodynamically very clean blade configuration had been obtained which provided higher flow coefficients in the rotor passages than expected. The larger than predicted effective flow area resulted in lower discharge velocities and correspondingly higher total-to-static stage efficiencies. It still would be possible to raise the total-to-static efficiency an additional 2 or 3 per cent by using a properly designed exhaust diffuser. The possible gain that could be expected must be weighed carefully, however, against the additional size and weight of the required duct work.

The predicted total-to-total efficiency of 90 per cent was achieved or even slightly exceeded as shown in Fig. 12. Again there is a clear indication that the effective flow area of the rotor was larger than expected. This resulted in more pressure drop across the nozzles and less pressure drop across the rotor compared to design conditions. The degree of reaction thus was lower than intended, as borne out by a slight shift of the optimum velocity ratios toward lower than design values. To establish a reference for typical values of optimum velocity ratios, it is helpful to remember that for a pure impulse stage, having a total-to-static efficiency of 81 per cent, the optimum velocity ratio is 0.45 by definition. The corresponding value for a 50 per cent reaction stage is 0.63.

Theoretically, then, the throat area of the rotor should have been reduced a certain amount to obtain the intended amount of reaction and therefore highest possible efficiency. In practice,

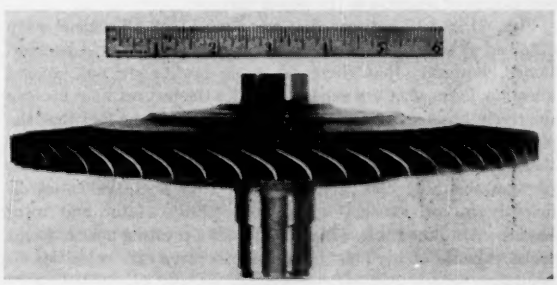

Fig. 10 Assembled rotor for a 400-hp turbine stage

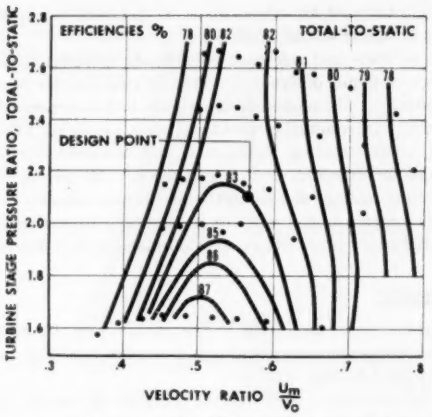

Fig. 11 Test performance of 400-hp turbine stage. Total-to-static efficiencies.

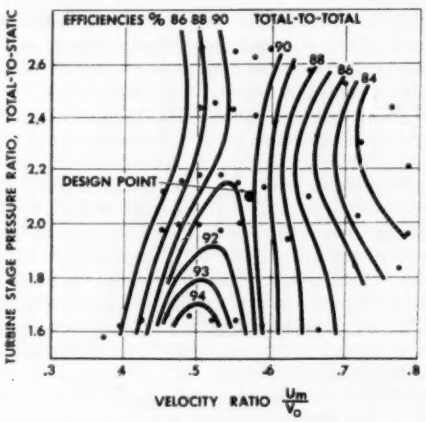

Fig. 12 Test performance of 400-hp turbine stage. Total-to-total efficiencies

however, the obvious remedy was to run the wheel slightly slower than planned because only a minor improvement could have been expected from a modified wheel. A further justification for accepting the wheel without modifications was found in the intended application of the turbine as a power-output stage of a free-turbine engine. In order to obtain the desired gas-producer turbine-inlet temperature in such an engine, it is often necessary to make certain final flow-area adjustments in the nozzles because of unavoidable manufacturing discrepancies. A slight increase in the nozzle flow area of the power turbine will reduce the inlet temperature of the gas-producer turbine. At the same time, such a flow-area change would have the tendency to restore the correct degree of reaction in the power turbine.

Figs. 11 and 12 indicate that some very high efficiencies were obtained at lower than design expansion ratios. It must be mentioned, however, that these favorable results are not beyond question, because at low expansion ratios the test readings become relatively less accurate. Of more significance is the fact that the efficiencies do not decrease at expansion ratios considerably higher than design. This means that the oblique nozzles of the diaphragm assembly can produce higher than sonic velocities efficiently in the vaneless space between the stator and rotor blades. Also, the rotor, which in effect is a rotating nozzle, seems to be capable of producing transonic relative exit velocities efficiently.

Transonic velocities are obtained behind any set of oblique

RAD	U	V_1	V_2	W_1	W_2	α_1	α_2	β_1	β_2
r_1	769	1480	505	791	912	18.1°	90.7°	36.1°	33.6°
r_2	875	1318	467	580	1007	20.3°	88.6°	52.5°	27.6°
r_3	982	1150	448	452	1038	22.7°	96°	81.4°	25.2°

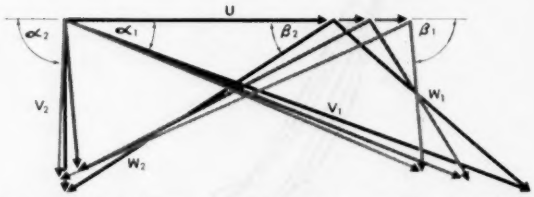

Fig. 13 Velocity diagrams for radius stations r_1, r_2, and r_3, calculated from test data.

RAD	U	V_1	V_2	W_1	W_2	α_1	α_2	β_1	β_2
r_1	769	1344	517	655	929	18.1°	90°	39.5°	34.1°
r_2	875	1200	517	485	1019	20.3°	90°	58.8°	30.6°
r_3	982	1083	517	415	1112	22.7°	90°	87.5°	27.8°

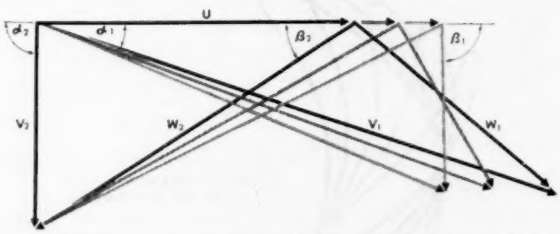

Fig. 14 Design-velocity diagrams for radius stations r_1, r_2, and r_3

annular nozzles, designed for subsonic flow if a high enough expansion head is available. The velocity at the nozzle throat then becomes sonic and further expansion takes place downstream because more flow area becomes available as the gas leaves the throat. Overexpansion can be utilized to good advantage in the design of axial-turbine stages with very high expansion ratios.

The performance maps further show that the stage efficiencies are more sensitive to underspeeding than to overspeeding. This effect also can be explained quite logically by considering the varying flow conditions, set up at off-design speeds by the fixed flow-passage configuration. However, a thorough discussion of off-design operating conditions is beyond the scope of this paper. Instead, it is considered more appropriate here to discuss briefly the flow pattern that was obtained at the test point closest to the design point.

To provide a clear idea of the flow pattern, the following information was recorded: Static pressure, total pressure, and total temperature ahead of the nozzles; static pressures at inner and outer shroud at nozzle exit; total pressure and flow direction at three different radius stations about 2 in. downstream from the rotor blades; static pressure and total temperature in the discharge chamber; air flow rates by means of a standard flow nozzle in the discharge duct. No attempt was made to measure total pressure and flow direction at the nozzle exit because previous experience had shown that such readings, to be reliable, must be taken at least 2 in. downstream from the blades. Even the static pressure readings at the nozzle exit are sometimes difficult to interpret because of prevailing transonic-flow conditions. With no flow-direction readings at the nozzle exit available, the assumption was made that the gas was leaving the nozzles exactly according to design calculations. This assumption was justified because the nozzle overturn angles had been established very carefully in earlier cascade tests.

The assumed nozzle-exit flow directions, together with the measured test data, permitted construction of velocity diagrams for the three radial stations where turbine-exit flow-directions readings were available. Fig. 13 shows these calculated velocity diagrams. For comparison, the design velocity diagrams are shown in Fig. 14 for the same three radius stations. Evidently a very close approximation of the design flow pattern was obtained in the test. The absolute discharge velocities were nearly equal in magnitude and parallel to the axis of rotation as planned. The incidence angles at the rotor inlet were somewhat larger than intended; about 3 deg larger near the root and 6 deg larger near the tip. No loss in efficiency was experienced, however, because the relative rotor-inlet velocities were low, especially near the tip where the incidence angle was a maximum. Well-rounded rotor leading edges also helped, preventing a serious loss. Significantly, the rotor turned the air more than expected; about $^1/_2$ deg more near the root and $2^1/_2$ deg more near the tip. These test results furnish evidence that an increase in rotor efficiency not only provides an increase in effective rotor flow area but also reduces the required amount of blade overturn.

Close examination of Fig. 13 reveals that the work output at the mean station is about 5 per cent and 10 per cent higher than at the hub station and tip station, respectively. Theoretically, the work output should have been equal at all radius stations because the blading design was based on an ideal free-vortex flow pattern. It cannot be expected, of course, that in any actual test perfect free-vortex velocity diagrams will be obtained because the accuracy of any test data is never perfect, and the flow pattern of a compressible gas always shows some unpredictable irregularities.

Review and Conclusions

A blade-design method has been developed that takes into consideration the basic theoretical concepts of fluid dynamics as well as experimentally established design parameters. The method can be applied by the average turbine designer after a short period of special training. No special computing equipment is required to establish the blade profiles unless a comprehensive study is undertaken to show how the blade profiles change for given variations of aerodynamic blade loadings. The integrations necessary to calculate the blade profiles can be carried out with sufficient accuracy in finite steps according to conventional methods if the blade chord is divided into at least ten equal increments. By applying the method to a specific case, it is explained how well-proportioned blades can be obtained that satisfy aerodynamic as well as structural requirements. The basic blade profile is fully determined from aerodynamic considerations, while experience factors are utilized only for refinements. The blade shapes are defined in a co-ordinate system that lends itself readily to manufacturing purposes. Test data, obtained from a turbine, designed according to this method, show that a very close approximation of the design flow pattern can be obtained. Specifically, it was demonstrated that nearly ideal free-vortex flow can be maintained across the blading with suitably designed blade profiles. Aerodynamic performance of the turbine stage exceeded expectations.

Success of any specific blade design, of course, still depends to a very large extent on the good judgment of the designer, but the described method provides him with a powerful design tool which virtually eliminates all guesswork.

APPENDIX I

Definition of Performance Parameters for Axial-Flow-Type Turbine Stage

Generally used performance parameters for an axial-flow-turbine stage are most conveniently defined by referring to a typical enthalpy-entropy diagram and a corresponding velocity diagram as shown in Fig. 15. Each velocity, indicated in the velocity diagram, has its corresponding enthalpy head in the entropy diagram. The dimensionless performance parameters—nozzle efficiency, rotor efficiency, over-all stage efficiency, degree of reaction, and velocity ratio—are defined as follows:

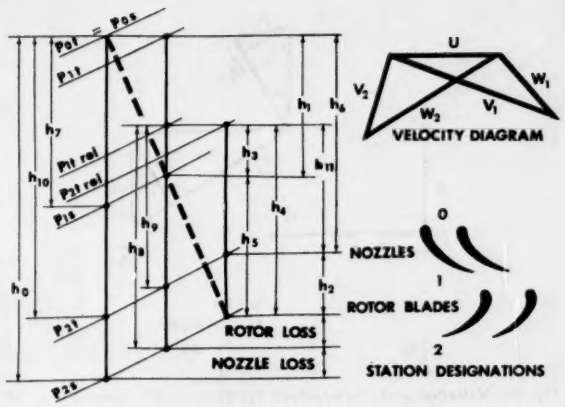

Fig. 15 Typical enthalpy-entropy diagram for axial-flow turbine stage

h_1/h_7 = nozzle efficiency, total-to-static
h_{11}/h_8 = rotor efficiency, total-to-static
h_{11}/h_9 = rotor efficiency, total-to-total
h_8/h_0 = stage efficiency, total-to-static
h_8/h_{10} = stage efficiency, total-to-total
$h_8/(h_2 + h_8)$ = degree of reaction
U/V_0 = velocity ratio

where $h_0 = \dfrac{V_0^2}{2gJ}$, total available expansion head

$h_1 = \dfrac{V_1^2}{2gJ}$, nozzle-exit, absolute-velocity head

$h_2 = \dfrac{V_2^2}{2gJ}$, rotor-exit, absolute-velocity head

$h_3 = \dfrac{W_1^2}{2gJ}$, rotor-inlet, relative-velocity head

$h_4 = \dfrac{W_2^2}{2gJ}$, rotor-exit, relative-velocity head

$h_8 = \dfrac{W_2^2 - W_1^2}{2gJ}$, stage-reaction head

$h_6 = \dfrac{V_1^2 - V_2^2 + W_2^2 - W_1^2}{2gJ}$, expansion work

Symbols for velocities and station designations, indicated by subscripts, are defined in Fig. 15.

APPENDIX II

Derivation of Differential Equations for Three-Dimensional Compressible Flow

For the aerodynamic design of turbomachinery, it is most convenient to set up the basic flow equations in terms of cylindrical co-ordinates. To simplify the problem, the case of a mass element moving at a constant radial velocity V_r along a radial beam, which

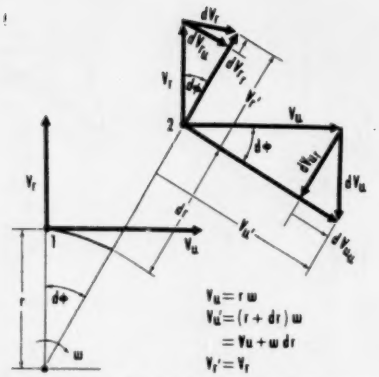

Fig. 16 Velocities and displacements for uniform differential motion of a mass element from point 1 to point 2

rotates at constant angular velocity ω around a fixed center, is considered first. Acceleration forces created by these uniform motions are calculated. In the second step, forces caused by accelerations in radial, tangential, and axial direction are superimposed to make the equations applicable to any type of three-dimensional flow pattern.

Fig. 16 shows the velocities and displacements to be considered if a mass element moves from point 1 to point 2 at constant V_r and constant ω.

The velocity increments in the tangential direction which are caused by the velocity V_r and by the radial displacement dr, dV_{r_u} and dV_{u_u}, respectively, can be calculated as follows:

$$\begin{aligned} dV_{r_u} &= V_r \sin d\phi \\ dV_{u_u} &= V_u' - V_u \cos d\phi \\ &= V_u + \omega dr - V_u \cos d\phi \\ &= \omega dr + V_u(1 - \cos d\phi) \end{aligned}$$

The velocity increments in the radial direction caused by V_r and dr, dV_{r_r} and dV_{u_r}, are

$$\begin{aligned} dV_{r_r} &= V_r' - V_r \cos d\phi = V_r(1 - \cos d\phi) \\ dV_{u_r} &= -V_u \sin d\phi \end{aligned}$$

For an infinitely small $d\phi$ these expressions can be simplified as follows:

$$\begin{aligned} dV_{r_u} &= V_r d\phi \\ dV_{u_u} &= \omega dr \\ dV_{r_r} &= 0 \\ dV_{u_r} &= -V_u d\phi \end{aligned}$$

The acceleration in the tangential direction can now be written

$$a_u = \frac{dV_{r_u}}{dt} + \frac{dV_{u_u}}{dt} = V_r \frac{d\phi}{dt} + \omega \frac{dr}{dt}$$

$$a_u = V_r\omega + \omega V_r = 2\omega V_r \tag{9}$$

This is the Cariolis acceleration.

The acceleration in radial direction is

$$a_r = \frac{dV_{u_r}}{dt} = -V_u \frac{d\phi}{dt} = -V_u\omega = -r\omega^2 \tag{10}$$

This is the centripetal acceleration.

If, in addition to the accelerations just described, the mass element has linear accelerations a_R in the direction of the beam and a_z in the direction of the axis while the beam itself has an angular acceleration α in the tangential direction, then the resulting accelerations in the three principal directions become

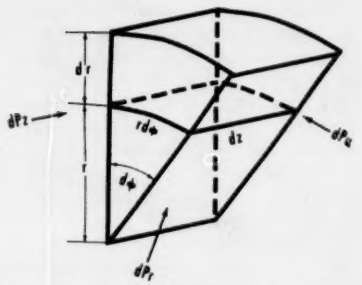

Fig. 17 Mass element and differential forces in the three principal directions

$$\left.\begin{aligned} a_r &= a_R - r\omega^2 = \frac{dV_r}{dt} - r\omega^2 \\ a_u &= \alpha r + 2\omega V_r = \frac{d\omega}{dt} r + 2\omega V_r \\ a_z &= \frac{dV_z}{dt} \end{aligned}\right\} \tag{11}$$

With the accelerations known, the forces dP acting on a mass element dm can be expressed according to Newton's first law:

$$\left.\begin{aligned} dP_r &= dma_r \\ dP_u &= dma_u \\ dP_z &= dma_z \end{aligned}\right\} \tag{12}$$

where

$$dm = rd\phi\, dr\, dz\, \rho \tag{13}$$

Fig. 17 shows a mass element in cylindrical co-ordinates with differential forces acting in the three principal directions. The forces dP also may be expressed in terms of pressure gradients:

$$\left.\begin{aligned} dP_r &= -\frac{\partial p}{\partial r} dr\, rd\phi\, dz \\ dP_u &= -\frac{\partial p}{r\partial\phi} rd\phi\, dr\, dz \\ dP_z &= -\frac{\partial p}{\partial z} dz\, rd\phi\, dr \end{aligned}\right\} \tag{14}$$

By substituting expressions (11) and (13) in (12) and equating to (14), we find:

$$rd\phi\, dr\, dz\rho \left(\frac{dV_r}{dt} - r\omega^2\right) = -\frac{\partial p}{\partial r} dr\, rd\phi\, dz$$

$$r\, d\phi\, dr\, dz\rho \left(\frac{d\omega}{dt} r + 2\omega V_r\right) = -\frac{\partial p}{r\partial\phi} rd\phi\, dr\, dz$$

$$rd\phi\, dr\, dz\rho \frac{dV_z}{dt} = -\frac{\partial p}{\partial z} dz\, rd\phi\, dr$$

Cancelling common factors, we find the general differential equations for three-dimensional compressible flow:

$$-\frac{\partial p}{\partial r} = \rho\left(\frac{dV_r}{dt} - r\omega^2\right) \tag{15}$$

$$-\frac{\partial p}{r\partial\phi} = \rho\left(\frac{d\omega}{dt} r + 2\omega V_r\right) \tag{16}$$

$$-\frac{\partial p}{\partial z} = \rho \frac{dV_z}{dt} \tag{17}$$

The Basic Heat Transfer and Flow Friction Characteristics of Six Compact High-Performance Heat Transfer Surfaces

W. M. KAYS

Professor of Mechanical Engineering, Stanford University, Stanford, Calif. Mem. ASME

In this paper the basic characteristics of six new compact high-performance surfaces are presented. Four are of the strip-fin type, including three stacked in a unique multiple sandwich arrangement. One of the surfaces has perforated fins formed by punching circular holes through the fins, and one has wavy fins. The basic characteristics are presented in terms of $N_{St}N_{Pr}^{2/3}$ *and* f *versus Reynolds number. A sufficient geometrical description is provided so that the data are readily usable in heat exchanger design analysis. The triple-sandwich surface introduces some new complications in the analysis of the effectiveness of the fins, and this problem is considered in an Appendix.*

Introduction and Objectives

In 1947 a research program was established at Stanford University, under the sponsorship of the Office of Naval Research, the Bureau of Ships, and the Bureau of Aeronautics, for the purpose of investigating the basis heat transfer and flow friction characteristics of compact high-performance heat transfer surfaces. The original impetus for this work came from the advent of the gas turbine as a promising transportation-type prime mover, and the further promise offered by inclusion of heat exchangers in the cycle. The shell-and-tube heat exchanger, while perhaps satisfactory for a stationary power plant, looms very large and bulky for the transportation application, and it was felt worth while to investigate some of the much more compact heat exchanger surfaces, especially of the extended-surface variety, that have been used extensively in aircraft intercoolers, air-conditioning systems, and many other primarily low temperature applications.

The objectives of the program were to first determine by direct test the basic characteristics of a large variety of different surfaces and, secondly, to investigate the flow and heat transfer mechanisms so as to form a rational basis for the design of new surfaces of superior characteristics. Most of the surfaces tested were of low temperature construction, usually aluminum, but the

Contributed by the Gas Turbine Power Division and presented at the Gas Turbine Power Conference and Exhibit, Cincinnati, Ohio, March 8–11, 1959, of The American Society of Mechanical Engineers.

Note: Statements and opinions advanced in papers are to be understood as individual expressions of their authors and not those of the Society. Manuscript received at ASME Headquarters, December 31, 1958. Paper No. 59—GTP-2.

Nomenclature

English Letter Symbols

- A = total heat transfer surface area, ft²
- A_c = free-flow area on one side of a heat exchanger core, ft²
- A_f = surface area of the fins, ft²
- a = a fin element length, ft, see Fig. 8
- b = plate spacing, ft; also a fin element length, ft, see Fig. 8
- c_p = specific heat at constant pressure, Btu/(lb$_M$ deg F)
- F = total drag force, lb$_F$
- G = core mass velocity based on A_c, lb$_M$/(hr ft²)
- g_c = proportionality factor in Newton's Second Law, 32.2 (lb$_M$ft)/(lb$_F$-sec²)
- h = convection heat transfer conductance, Btu/(hr ft² deg F)
- k = thermal conductivity, Btu/(hr ft² deg F/ft)
- L = total flow length through heat exchanger core, ft; also a fin element length, ft, see Fig. 8
- M = a fin element length, ft, see Fig. 8
- r_h = hydraulic radius, ft, defined as A_cL/A
- U = over-all unit conductance, based on A, Btu/(hr ft² deg F)
- V = velocity, ft/sec
- w = flow rate, lb/hr

Greek Letter Symbols

- α = thickness of a fin element, ft, see Fig. 8
- β = surface area density, surface area per unit of volume between the plates of one side of the heat exchanger, ft²/ft³; also thickness of a fin element, ft, see Fig. 8
- γ = thickness of a fin element, ft, see Fig. 8
- δ = thickness of a fin element, ft, see Fig. 8
- μ = viscosity coefficient, lb$_M$/(hr ft)
- η_f = fin effectiveness, dimensionless
- η_o = over-all surface effectiveness, dimensionless, see Equation (2)
- ρ = fluid density, lb$_M$/ft³
- τ_0 = equivalent shear stress at the surface, F/A, lb$_F$/ft²

Nondimensional Groupings

- $N_{St}N_{Pr}^{2/3}$ = convective heat transfer parameter, $(h/Gc_p)(\mu c_p/k)^{2/3}$, Stanton number times the two-thirds power of the Prandtl number
- N_R = Reynolds number, $4r_hG/\mu$
- f = friction factor, $\tau_0/(\rho V^2/2g_c)$
- NTU = number of transfer units, $(AU)/(wc_p)$

surface characteristics have nothing to do with the material of construction, and it was felt that if such surfaces showed sufficient promise for the gas turbine application there would be incentive to develop methods of construction using high-temperature materials.

As the program progressed, and the performance data became available in a form useful to heat exchanger designers, and to those making feasibility studies for various applications, it became apparent that such data would be useful in a far wider variety of applications than merely in the gas turbine. Thus the program was broadened to include surfaces that might not be of direct interest to the gas turbine application. Subsequently the AEC joined in sponsorship of the program.

The test results and the various conclusions that have been reached relative to the basic mechanisms and the ultimate possibilities of compact high-performance surfaces have been published in a number of papers in the ASME TRANSACTIONS. In 1954 the characteristics of 88 surface configurations were summarized in a report that has subsequently been made available in book form [1].[1] This summary includes not only all of the data obtained as a part of this project, but also a substantial quantity of similar data obtained elsewhere.

Since 1954 a number of new and interesting surfaces have been introduced by various manufacturers, and it was decided to reinstitute the test program on a modest scale. To date six additional surfaces have been tested, and it is the objective of this paper to present these new data so as to make them generally available for heat exchanger design and feasibility studies, and to supplement and augment conclusions previously reached.

Experimental Apparatus and Reduction of Data

Each of the test surfaces are built into steam-to-air test cores, $8^3/_4 \times 9^3/_4$ in. frontal dimensions, with the surface under consideration on the air side. The test apparatus consists of an induced-draft air duct in which air flow rate can be accurately controlled and metered, and in which air temperature can be accurately determined. Slightly superheated steam is supplied to the steam-side of the test cores and condenses on the steam-side surface. A considerable excess of steam is passed through the core to prevent the build-up of a thick condensate layer. Instrumentation is provided to measure air, condensate, and blow-steam rates, air entering and leaving state, and steam entering and leaving state. A complete and detailed description of this apparatus is given in reference [2] and thus will not be elaborated upon here. It will suffice to say that provision is made to establish an energy balance between the steam and air sides of the test cores, and the energy unbalance for the test cores considered here was consistently less than 3 per cent. An estimate of the experimental uncertainty is also given in reference [2], with uncertainty intervals established at ±5 per cent for the friction factor f and the heat grouping $N_{St}N_{Pr}^{2/3}$. The uncertainty interval in the Reynolds number is ±2 per cent.

The details of the method of reduction of data are presented in reference [2]. It should be noted here that the steam-side heat transfer resistance and the ineffectiveness of the extended surfaces (fins) are taken into account so that the reported results pertain to the surface geometry alone and are independent of the steam-side and the material of the fins.

Method of Presentation of the Results

The heat transfer and flow friction characteristics, respectively, are presented using the dimensionless correlations, $N_{St}N_{Pr}^{2/3}$ versus N_R and f (Fanning friction factor) versus N_R. These results are given in tabular form in the Tables and also in graphical form, Figs. 1 to 6. Two sets of tests are run for each test core. One is called a hot-core test, in which heat transfer takes place and both heat transfer and friction measurements are made; the other is an isothermal test in which only friction measurements are made. On Figs. 1 to 6 the curves representing the best interpretation of the friction factor data are drawn through the

[1] Numbers in brackets designate References at end of paper.

Tables Summary of basic heat transfer and friction data $(h/Gc_p)N_{Pr}^{2/3}$, f versus N_R from smoothed curves

Surface 1/4-15.4(D)

N_R	$(h/Gc_p)N_{Pr}^{2/3}$	f
6000	.00510	.0167
5000	.00537	.0175
4000	.00570	.0186
3000	.00617	.0202
2500	.00650	.0213
2000	.00692	.0228
1500	.00756	.0255
1200	.00809	.0283
1000	.00864	.0314
800	.00952	.0362
600	.01107	.0443
500	.01227	.0507
400	.01407	.0601
300	.0169	.0757

Surface 1/8-16.12(D)

N_R	$(h/Gc_p)N_{Pr}^{2/3}$	f
5000	.00721	.0310
4000	.00764	.0315
3000	.00822	.0334
2500	.00859	.0357
2000	.00908	.0379
1500	.00987	.0400
1200	.01060	.0429
1000	.01123	.0464
800	.01205	.0517
600	.01352	.0607
500	.0150	.0679
400	.0176	.0781
300	.0226	.0937

Surface 1/8-16.12(T)

N_R	$(h/Gc_p)N_{Pr}^{2/3}$	f
5000	-	.0358
4000	.00705	.0370
3000	.00773	.0386
2500	.00820	.0397
2000	.00880	.0416
1500	.00967	.0440
1200	.01045	.0464
1000	.01122	.0496
800	.01225	.0552
600	.01395	.0644
500	.0155	.0721
400	.0179	.0830
300	.0219	.1003

Surface 13.95(P)

N_R	$(h/Gc_p)N_{Pr}^{2/3}$	f
12000	-	.01168
10000	.00503	.01220
8000	.00547	.01285
6000	.00600	.01386
5000	.00631	.0146
4000	.00660	.0155
3000	.00695	.0169
2500	.00708	.0178
2000	.00700	.0187
1500	.00736	.0207
1200	.00817	.0232
1000	.00893	.0257
800	.01010	.0295
600	.01180	.0357
500	.0132	.0407

Tables (continued)

Surface 1/8-13.95

N_R	$(h/Gc_p)N_{Pr}^{2/3}$	f
8000	-	.0628
6000	.0110	.0650
5000	.01170	.0664
4000	.01250	.0684
3000	.0137	.0712
2500	.0144	.0733
2000	.0155	.0765
1500	.0168	.0817
1200	.0181	.0870
1000	.0192	.0927
800	.0204	.1020
600	.0223	.1170
500	.0233	.131
400	.0247	.154

Surface 11.5-3/8(W)

10000	.00686	.0331
8000	.00746	.0357
6000	.00831	.0398
5000	.00890	.0427
4000	.00970	.0467
3000	.01077	.0525
2500	.01155	.0567
2000	.0126	.0625
1500	.0140	.0704
1200	.0150	.0779
1000	.0158	.0845
800	.0167	.0926
600	.0178	.1035
500	.0185	.111
400	.0194	.118

test points for the isothermal flow tests, since for these there is no question of the effects, if any, of the temperature varying fluid properties. The curves representing the best interpretation of the heat transfer data lie somewhat above the actual test points due to an allowance for an estimate of the steam-side heat transfer resistance. This method of presentation has been arbitrarily adopted simply because the uncertainty in the steam-side estimate is much greater than for any of the other quantities, and it is possible to see at a glance the effect of this uncertainty.

The Reynolds number $N_R = (4r_hG/\mu)$ is evaluated on the basis of the flow passage hydraulic radius and a viscosity evaluated at the logarithmic mean temperature, which is essentially the mean of the bulk air temperature with respect to flow length. This temperature is also used to evaluate Prandtl number in the heat transfer correlation. The hydraulic radius is defined as follows:

$$r_h/L = A_c/A$$
$$r_h = A_cL/A$$

For cylindrical tubes of any cross-section geometry, A_cL/A is identical with the flow cross section divided by the wetted perimeter, which is the conventional definition of hydraulic radius.

The friction factor is evaluated on the basis of an equivalent shear stress on the heat transfer surface area A which is in turn simply defined as the total drag forces opposing the flow divided by the heat transfer area. Thus,

$$\tau_0 = F/A = f\rho V^2/2g_c$$

This pseudo shear stress can be made up of both true shear and pressure forces acting on elements of surface not parallel to the flow direction.

The tabular "Summary of basic heat transfer and friction data" is taken directly from the curves representing the best interpretation of the data.

Description of the Test Surfaces

The six surfaces to be considered here are all of the plate-fin variety, i.e., fins are bonded between parallel plates to form continuous flow passages. The plates can then be stacked sandwich-type to form crossflow or counterflow heat exchangers with each of the two fluids flowing between alternate pairs of plates. A virtue of the plate-fin arrangement lies in the great flexibility afforded the designer who can employ entirely different fin arrangements and configurations, and different plate spacing, on the two fluid sizes of the heat exchanger. But more important, this arrangement lends itself to very great area compactness (heat transfer area per unit of volume), and it becomes a simple matter to substantially increase the heat transfer conductance by the use of various methods of boundary layer interruption and turbulence promotion. When high heat transfer conductances are obtained by such methods the surface is often termed a *high-performance surface*. High performance is generally bought at the expense of increased friction factors, but it can be readily demonstrated that in terms of over-all heat exchanger weight and volume, a very substantial increase in friction factor can be tolerated as the price for a modest increase in the heat transfer parameter $N_{St}N_{Pr}^{2/3}$.

Diagrams of the surfaces considered here are shown in the upper right-hand corner of Figs. 1 to 6. All six can be classed as high-performance surfaces in that they all incorporate methods of boundary layer interruption to increase the convective heat transfer conductance. The surfaces shown on Figs. 1, 2, 3, and 4 will be referred to as *strip-fin* surfaces. The fins are formed from a continuous sheet of material that is folded to form flow passages, cut and offset at intervals in the flow direction to provide boundary layer interruption, and then is brazed between parallel plates. The surface shown on Fig. 4 is the more conventional type of strip-fin surface with a single set of fins between the base or prime surface. The characteristics of a number of surfaces of this type are presented in reference [1].

The surfaces shown on Figs. 1, 2, and 3 are unique in that they are multiple sandwich arrangements. Two and, in the case of Fig. 3, three sets of fins are brazed between a single pair of base plates. The sets of fins are separated by splitter plates to which they are also brazed. The splitter plates provide additional extended or fin surface, and in the case of the triple sandwich, Fig. 3, the heat to the center passage fins must first be conducted through the splitter plates. The idea behind the multiple sandwich arrangement is the greater flexibility allowed the designer and manufacturer. In a gas-to-gas heat exchanger where there is a large disparity in gas density on the two sides of the heat exchanger, a balanced design will usually call for more surface area and more flow area on the low density gas side. With the multiple sandwich arrangement, a triple sandwich might be used on the low density side while a single sandwich could be used on the high density side. The actual fin material on each side could be identical, which has obvious advantages to the manufacturer in terms of the number of dies which must be stocked and maintained. The gas turbine regenerator is a classic example of a gas-to-gas heat exchanger with a large density difference on each side, and this scheme, which has so far been employed only for low temperature applications, is offered for consideration in the gas turbine application.

The individual flow passages in a multiple sandwich surface are identical, so one would expect the same basic characteristics, $N_{St}N_{Pr}^{2/3}$ and f versus N_R, regardless of whether the arrangement is of the single, double, or triple-sandwich type, provided the same fin material is used. However, the fin effectiveness analysis is more complex for the double and triple sandwich than for the single sandwich (see Appendix), and the triple sandwich appears to introduce other difficulties to be discussed later. The double and triple sandwich surfaces shown on Figs. 2 and 3 have identical

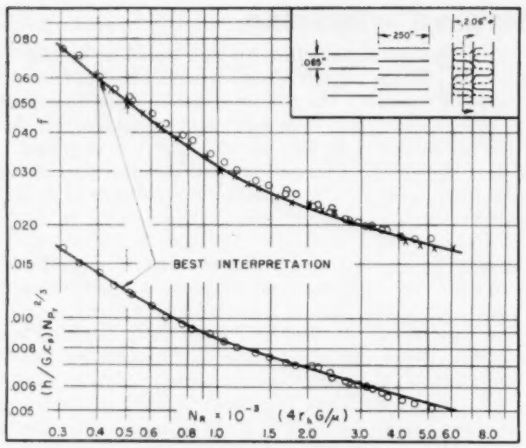

Fig. 1 Heat transfer and friction data, surface 1/4–15.4(D)

Surface Data, Air Side:

Fin pitch, 15.4 fins per inch
Plate spacing, $b = 0.206$ in.
Splitter symmetrically located
Fin length (flow direction), 0.250 in.
Flow passage hydraulic diameter, $4r_h = 0.00527$ ft
Fin metal thickness, 0.006 in.
Total heat transfer area/volume between plates, $\beta = 642$ ft^2/ft^3
Fin area (including splitter)/total area, 0.816

o, Hot core test points. Heat-transfer data evaluated on the basis of zero steam-side resistance.
x, Cold core friction factors.
Best interpretation of friction data based on cold core data.
Best interpretation of heat-transfer data based on an allowance for steam-side resistance.

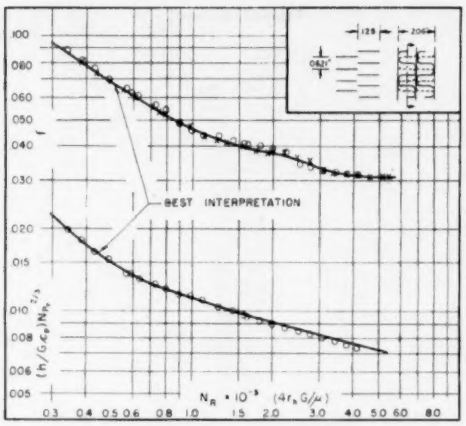

Fig. 2 Heat transfer and friction data, surface 1/8–16.12(D)

Surface Data, Air Side:

Fin pitch, 16.12 fins per inch
Plate spacing, $b = 0.206$ in.
Splitter symmetrically located
Fin length (flow direction), 0.125 in.
Flow passage hydraulic diameter, $4r_h = 0.00509$ ft
Fin metal thickness, 0.006 in.
Total heat transfer area/volume between plates, $\beta = 660$ ft^2/ft^3
Fin area (including splitter)/total area, 0.823

o, Hot core test points. Heat-transfer data evaluated on the basis of zero steam-side resistance.
x, Cold core friction factors.
Best interpretation of friction data based on cold core data.
Best interpretation of heat-transfer data based on an allowance for steam-side resistance.

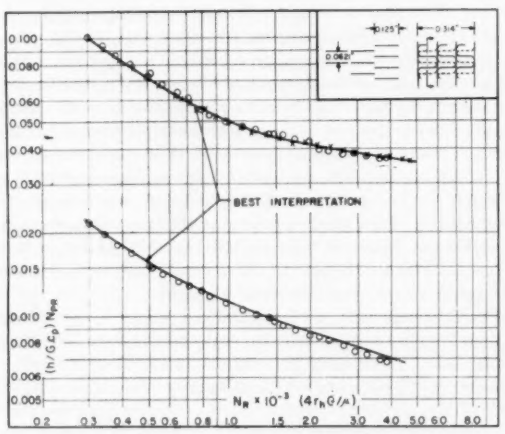

Fig. 3 Heat transfer and friction data, surface 1/8–16.12(T)

Surface Data, Air Side:

Fin pitch, 16.12 fins per inch
Plate spacing, $b = 0.314$ in.
Splitters symmetrically located for three even passages
Fin length (flow direction), 0.125 in.
Flow passage hydraulic diameter, $4r_h = 0.00514$ ft
Fin metal thickness, 0.006 in.
Total heat transfer area/volume between plates, $\beta = 650$ ft^2/ft^3
Fin area (including splitters)/total area, 0.882

o, Hot core test points. Heat-transfer data evaluated on the basis of zero steam-side resistance.
x, Cold core friction factors.
Best interpretation of friction data based on cold core data.
Best interpretation of heat-transfer data based on an allowance for steam-side resistance.

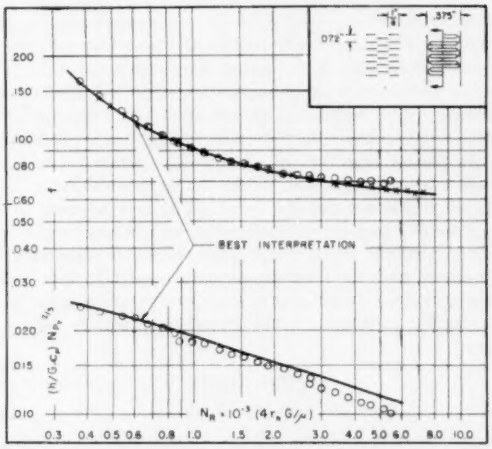

Fig. 4 Heat transfer and friction data, surface 1/8–13.95

Surface Data, Air Side:

Fin pitch, 13.95 fins per inch
Plate spacing, $b = 0.375$ in.
Fin length (flow direction), 0.125 in.
Flow passage hydraulic diameter, $4r_h = 0.00879$ ft
Fin metal thickness, 0.010 in.
Total heat transfer area/volume between plates, $\beta = 381$
Fin area/total area, 0.840
Note: The fin surface area on the leading and trailing edges of the fins has *not* been included in computations.

o, Hot core test points. Heat-transfer data evaluated on the basis of zero steam-side resistance.
x, Cold core friction factors.
Best interpretation of friction data based on cold core data.
Best interpretation of heat-transfer data based on an allowance for steam-side resistance.

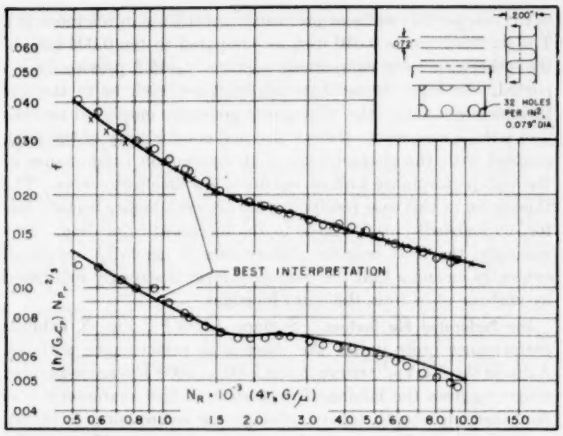

Fig. 5 Heat transfer and friction data, surface 13.95(P)

Surface Data, Air Side:

Fin pitch, 13.95 fins per inch
Plate spacing, $b = 0.200$ in.
Fin center material perforated with 0.079-in-diam holes spaced 32 per square inch in square pattern (16 per cent open). Position of holes in walls of various passages differs.
Flow passage hydraulic diameter, $4r_h = 0.00822$ ft
Fin metal thickness, 0.012 in
Total heat transfer area/volume between plates, $\beta = 381$ ft²/ft³
Fin area/total area, 0.705
Note: Because of the very thick fins the surface area in the rim of the holes has been included in computations.

o, Hot core test points. Heat-transfer data evaluated on the basis of zero steam-side resistance.
x, Cold core friction factors.
Best interpretation of friction data based on cold core data.
Best interpretation of heat-transfer data based on an allowance for steam-side resistance.

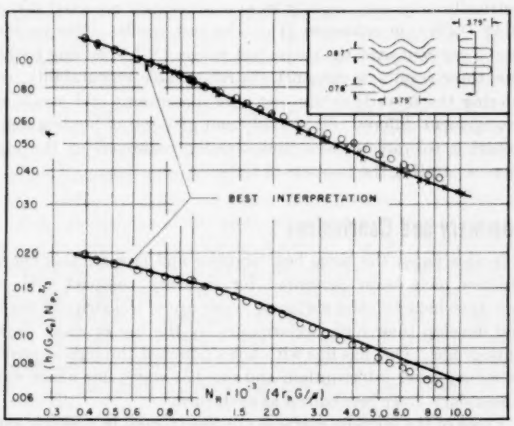

Fig. 6 Heat transfer and friction data, surface 11.5–3/8(W)

Surface Data, Air Side:

Fin pitch, 11.5 fins per inch
Plate spacing, $b = 0.375$ in.
Flow passage hydraulic diameter, $4r_h = 0.00993$ ft
Fin metal thickness, 0.010 in.
Total heat transfer area/volume between plates, $\beta = 347$ ft²/ft³
Fin area/total area, 0.822

o, Hot core test points. Heat-transfer data evaluated on the basis of zero steam-side resistance.
x, Cold core friction factors.
Best interpretation of friction data based on cold core data.
Best interpretation of heat-transfer data based on an allowance for steam-side resistance.

flow passages in all respects, the difference being only in the sandwich arrangement. The purpose in testing these two was to determine what, if any, new problems would be encountered in the triple sandwich arrangement. The double sandwich surfaces shown on Figs. 1 and 2 differ materially in that the uninterrupted fin-flow lengths are respectively 1/4 and 1/8 inch.

The surface shown on Fig. 5 employs a novel system of boundary layer interruption. The fin material is perforated with holes before being folded and brazed between the plates. The surface shown on Fig. 6 has fins bent in the flow direction to form wavy passages. Boundary layer separation apparently occurs at the turns to provide a high conductance, so this is also a high-performance surface. Other examples of this type of surface are presented in reference [1]; in fact, this particular surface differs only in a minor way from the surface designated 11.44–3/8(W) in that reference.

A semidescriptive method of surface designation is employed, consistent with the designations used in reference [1]. For the strip-fin surfaces the first number refers to the fin-flow-length in the flow direction, e.g., 1/8 inch or 1/4 inch. The second number refers to the number of fins per inch transverse to the flow direction. The letter in parenthesis refers to the double or triple sandwich construction. Thus the strip-fin surfaces shown on Figs. 1, 2, 3, and 4 are designated, respectively,

1/4–15.4(D)

1/8–16.12(D)

1/8–16.12(T)

1/8–13.95

The perforated fin surface shown on Fig. 5 is designated by the number of fins per inch with the letter P referring to the perforated fins. Thus this surface is designated,

13.95(P)

The wavy fin surface shown on Fig. 6 is designated by the number of fins per inch, the wave length, and the letter W to designate the wavy fin construction. Thus this surface is designated,

11.5–3/8(W)

The captions to Figs. 1 to 6 contain the complete dimensional data for each of the surfaces, including the hydraulic diameter and the surface area density.

Discussion of the Test Results

The Strip-Fin Surfaces. All of the strip-fin surfaces, Figs. 1 to 4, exhibit the general characteristics of such surfaces noted previously. The heat transfer mechanism is primarily conduction through a laminar boundary layer that originates and grows on each individual fin. Turbulence appears to play a relatively minor part, although there is some evidence that the very high heat transfer performance of surface 1/8–13.95 is in part attributable to a disturbance of the otherwise laminar boundary layer by turbulent eddies shed from the blunt leading and trailing edges of the relatively thick (0.010 inch) fins. All of these surfaces have rather high friction factors attributable to the form or pressure drag offered by the blunt leading and trailing edges of the fins.

On Fig. 7 the test results for the three multiple sandwich surfaces are compared. Comparing the two double sandwich surfaces, it will be noted that cutting and separating the fins every 1/8 inch rather than every 1/4 inch (this is the only major difference between the surfaces) results in a substantial increase in $N_{St}N_{Pr}^{2/3}$ and a very large increase in f. The increase in heat transfer performance is a result of the thinner boundary layer. The increase in friction factor is attributable to both the thinner

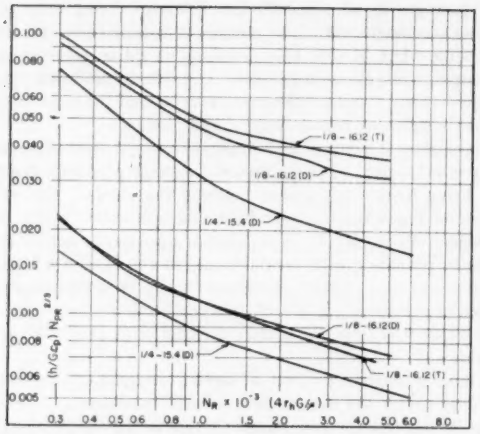

Fig. 7 Comparison of the test results for the multiple sandwich surfaces

boundary layer with its larger average shear stress, and to a greater degree the increased form drag resulting from there being twice as many fin edges.

Surfaces $^1/_8$–16.12(D) and $^1/_8$–16.12(T) are identical save that one is in a double sandwich and the other is in a triple sandwich. Close to identical performance should be expected. At Reynolds numbers less than 1000 this is certainly the case, and the discrepancies noted can be easily attributed to manufacturing tolerances. These are compact surfaces and a 0.001-inch variation in fin spacing or plate spacing can have a rather large effect, especially on the friction factor. However, the 15 per cent difference in friction factor at the higher Reynolds numbers is more than one would like to charge to dimensional tolerances, and the triple sandwich surface tends to yield lower heat transfer than its double-sandwich counterpart. The fin conduction problem in the case of the triple sandwich is considerably more complex than for the double sandwich, but this has been taken into consideration. The results of an analysis of the fin effectiveness in a triple sandwich surface are presented in the Appendix. Besides which, the conduction problem can have nothing to do with the friction factors. One possible explanation could be a flow mal-distribution resulting in a disproportionate share of the flow going through the center of the three passages. Such a flow distribution could be caused by the abrupt contraction entrance to the test core where a two-dimensional vena-contracta undoubtedly occurs, resulting in a higher total pressure at the entrance to the center section than at the entrance to the two outside sections. Calculations based on an assumed contraction ratio indicate that a very large increase in apparent friction factor could occur, but that the apparent $N_{St}N_{Pr}^{2/3}$ remains virtually unchanged. However, the higher flow velocity in the center section would result in a higher conductance, and this in turn would decrease the fin effectiveness. This latter possibility has not been investigated, but still remains the most plausible explanation. If poor flow distribution is truly the explanation of the differences noted, then it should be further noted that the air flow length of the test cores was only $2^3/_8$ inches. In applications where flow length is substantially greater than $2^3/_8$ inches the flow distribution for the triple sandwich would be expected to be better, and performance approaching that of the comparable double sandwich should be anticipated. Also some form of flow distribution control could be provided, such as a nozzle entrance. At any rate, this is a problem that should be considered in application of the triple sandwich arrangement to heat exchanger design.

The results for surface $^1/_8$–13.95, Fig. 4, are of interest primarily in that they show the effect of a substantially thicker fin than any of the comparable surfaces previously considered in reference [1]. The fin thickness is 0.010 inch as compared to the 0.006 inch of the otherwise very comparable surface $^1/_8$-15.2 previously reported. In high temperature applications, such as in the gas turbine regenerator, the alloy steels generally employed necessitate a thick fin because the low thermal conductivity of the steel, coupled with the characteristic high convection conductance of the high-performance surface, results in low fin effectiveness. The thicker fin in this case results in a 25 per cent higher friction factor, undoubtedly attributable to the increased form drag. Surprisingly, the heat transfer performance is similarly improved, evidently meaning that the boundary layer is strongly influenced by vortexes shed from the blunt fin edges.

The Perforated Fin Surface. Surface 13.95(P), Fig. 5, exhibits performance quite unlike the other high performance surfaces. A dip in the $N_{St}N_{Pr}^{2/3}$ curve in the 1500 to 3000 Reynolds-number range suggests the laminar flow–turbulent flow characteristic of flow through smooth tubes, although the entire curve is shifted upward at least 50 per cent above a smooth tube. The most interesting feature of the performance of this surface is the friction factor curve. The friction factors in the "turbulent" region are only a little more than twice the $N_{St}N_{Pr}^{2/3}$, indicating little if any form drag. Such a characteristic is very desirable in heat exchanger design, for it results in a minimum heat exchanger core frontal area, a particularly bothersome problem in many applications of very compact high-performance surfaces, and most especially in the gas turbine regenerator application. The holes apparently accomplish an effective interruption of the turbulent sublayers without the high velocity part of the stream impinging upon blunt edges normal to the flow direction. Part of the surface area is of course lost by this expedient, nullifying part of the gain as far as heat exchanger volume is concerned, although the weight advantage remains. From the results of these tests alone it is not possible to tell whether an optimum has been achieved with respect to size of hole and frequency of hole.

The Wavy-Fin Surface. Surface $11.5–^3/_8$(W), Fig. 6, differs geometrically only very slightly from a previously reported surface, $11.44–^3/_8$(W), in reference [1]. The test results differ no more than 5 per cent over the entire test range. While adding nothing new, these results do demonstrate remarkable repeatability, considering the facts that the test core dimensions and steam-side arrangement differed considerably and methods of holding manufacturing tolerances have undoubtedly improved in the eight years separating the two sets of tests.

Summary and Conclusions

In this paper the basic heat transfer and flow friction characteristics have been presented for six very compact high-performance heat transfer surfaces. Four are of the strip-fin variety and develop their high performance by the use of short discontinuous fins. One has fins with holes punched through to provide boundary layer interruption, and one has wavy fins which cause a boundary layer breakdown at each turn.

Three of the strip-fin surfaces are constructed in multiple sandwiches, and the tests indicate that flow distribution difficulties may be encountered in a triple sandwich arrangement, especially if an abrupt contraction entrance is used and the total flow length is small. In the Appendix the special problem of the fin effectiveness of a triple sandwich is considered.

One of the strip-fin surfaces demonstrates the results of relatively thick fins, which tend to substantially increase friction factor, but which also materially increase heat transfer performance.

The perforated fin surface results indicate a distinct advantage in this type of boundary layer interruption, for a substantial increase in heat transfer performance is attained without

introducing an additional form-drag component to the friction factor.

The results for the wavy fin surface serve primarily to demonstrate the repeatability of the data contained in reference [1].

Acknowledgments

The work reported in this paper was supported by the Office of Naval Research, Contract Nonr 225(23), at Stanford University.

The bulk of the test work was carried out by Mr. D. C. Briggs, graduate student in mechanical engineering and holder of a Trane Company Fellowship, Mr. O. A. Buchmann, graduate student in mechanical engineering and holder of an AiResearch Company Fellowship, and Lt. D. M. Hennessee, graduate student in mechanical engineering. Mr. Buchmann was also responsible for the analysis of the fin effectiveness problem arising in the triple sandwich surface.

References

1 W. M. Kays and A. L. London, "Compact Heat Exchangers," McGraw-Hill Book Company, New York, N. Y.

2 W. M. Kays and A. L. London, "Heat-Transfer and Flow-Friction Characteristics of Some Compact Heat-Exchanger Surfaces, Part I, Test System and Procedure," TRANS. ASME, vol. 72, 1950, pp. 1075–1085.

APPENDIX

The Fin Effectiveness. The effectiveness of a fin is defined as the ratio of the heat actually transferred through the base of the fin to what that transfer rate would be if the entire fin surface were at the base temperature. In any actual fin the effectiveness is some number less than unity because of the temperature drop along the fin due to conduction resistance. Thus only with a fin material thermal conductivity of infinity could the fin effectiveness be unity.

For simple fins the effectiveness is a function of the fin length and thickness, the thermal conductivity of the fin material, and the convection conductance along the fin surface. These relationships are well known and will not be repeated here. However, the double and triple sandwich surfaces present a complex fin geometry which requires its own special solution. In this Appendix a general solution applicable to any double or triple sandwich arrangement will be presented, and then further consideration will be given to a fin effectiveness problem peculiar to the triple sandwich alone.

Any double or triple sandwich finned surface, symmetrical about the center line of the passage, can be represented for purposes of analysis by the diagram shown in Fig. 8. To maintain generality each of the fin elements are considered to be of different length and thickness. The analysis of this system for the fin effectiveness follows precisely the same procedures as are employed for analysis of simple fins; the problem is simply more complex, and the resulting expression for effectiveness is more complex. If the fluid surrounding the fin is considered to be everywhere at the *same temperature*, if the surface convection conductance is considered to everywhere be the same, and if fin temperature is a function only of fin length (thin fins), the following expression for the effectiveness results:

$$\eta_f = \frac{1}{m_1(L + M + a + b)} \left\{ \frac{[\alpha m_1 + (B + D + E)]e^{m_1 L}}{[\alpha m_1 + (B + D + E)\tanh(m_1 L)]\cosh(m_1 L)} - 1 \right\} \quad (1)$$

where

$$B = \beta m_2 \tanh(m_2 a)$$

$$D = \gamma m_3 \tanh(m_3 b)$$

$$E = \delta m_4 \tanh(m_4 M)$$

$$m_1 = \sqrt{2h/k\alpha}$$

$$m_2 = \sqrt{2h/k\beta}$$

$$m_3 = \sqrt{2h/k\gamma}$$

$$m_4 = \sqrt{2h/k\delta}$$

This solution can be reduced to the simple fin solution if a, b, and M are set equal to zero, or to the case of the double sandwich surface if M is set equal to zero.

Since a part of the total heat transfer surface area is a base or prime area (not extended area), an over-all surface effectiveness, η_o, is defined as,

$$\eta_o = 1 - (1 - \eta_f)(A_f/A) \quad (2)$$

η_o then expresses the ratio of actual heat transferred by the entire surface, A, to what this rate would be if η_f were 1.00. Note that $\eta_f < \eta_o < 1$.

Equation (1), together with (2), is probably an adequate solution for most double sandwich surface applications, but for a triple sandwich arrangement a new problem arises. An idealization basic to the analysis was that the fluid temperature is the same along the entire fin surface. If in a triple sandwich ar-

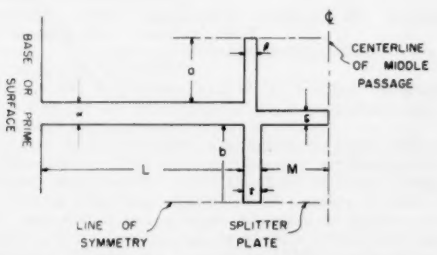

Fig. 8 Idealization of the fins in a multiple sandwich surface

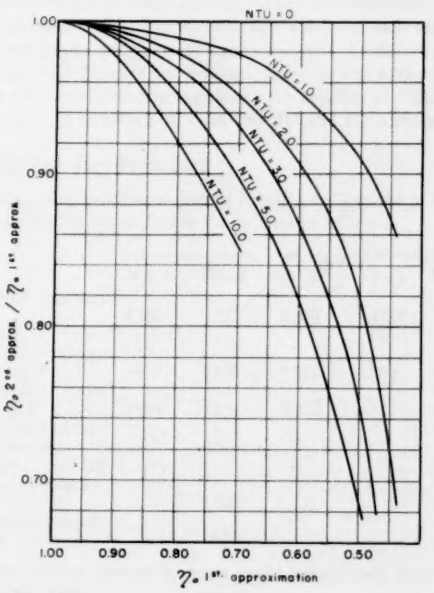

Fig. 9 Effect of the heat exchanger NTU on a triple sandwich over-all surface effectiveness

rangement the fin effectiveness tends to be low the fluid temperatures in the center and outer passages will only be close to equal near the entrance to the heat exchanger. At points removed from the entrance there will be less heat transfer to the fluid in the center passage, and a temperature difference between the fluid in the center passage and in the outer passages will be established. This solution no longer applies, and it is easy to see that the apparent fin effectiveness will be lower than given by this solution.

An approximate analysis for this effect has been carried out for the case of a heat exchanger with the base surface at a uniform temperature. A triple sandwich surface was chosen and was simplified such that (referring to Fig. 8) $M = L/2$, $a = b = L/4$, and $\alpha = \beta = \delta = \gamma$. This corresponds approximately to the proportions of the triple sandwich surface shown on Fig. 3. The details of this analysis are too lengthy to present here, but the results are of interest. The over-all performance of the heat exchanger was evaluated, taking into consideration the different behavior of the center passage as compared to the two outer passages. From this, working backward, an over-all surface effectiveness η_o was evaluated such that the simple heat exchanger solution would be applicable. Labeling this new effectiveness $\eta_{o2nd\ approx}$, and the over-all effectiveness from Equations (1) and (2) as $\eta_{o1st\ approx}$, the ratio of the second approximation to the first approximation is plotted on Fig. 9 as a function of the first approximation, with the heat exchanger NTU as a parameter. As expected, the triple sandwich surface will have a lower surface effectiveness than the more simple solution, Equations (1) and (2) would indicate, and this effect will be more pronounced for low surface effectiveness and for high NTU. The worst condition met in the tests of surface 1/8–16.12(T) is a surface effectiveness of about 0.90 at an NTU of about 1.0. From Fig. 9 the correction factor is 0.996, which is hardly worth worrying about. However, in an application of a triple sandwich surface where low conductivity high temperature materials must be used, as say in a gas turbine regenerator, $\eta_{o1st\ approx}$ might be in the range of 0.70 and NTU around 3.0. In this case the surface effectiveness as evaluated from simple theory would be about 7 per cent too high, and the true surface effectiveness would be nearer to 0.93×0.70 or 0.65. Note, on the other hand, that this analysis has been based on a heat exchanger with one fluid side at a constant temperature (or at least the base surface at a constant temperature) as in a condenser or evaporator. Somewhat different behavior would be expected of a counter or crossflow heat exchanger with equal capacity rates, but it is expected that Fig. 9 can still be used as a good approximation to the effect.

C. L. CLARK[1]
J. J. B. RUTHERFORD[2]
A. B. WILDER[3]
M. A. CORDOVI[4]

Metallurgical Evaluation of Superheater-Tube Alloys After Six-Months' Exposure at Temperatures of 1100 to 1500 F

THE ASME RESEARCH COMMITTEE on High Temperature Steam Generation has a program in progress to determine the performance characteristics of selected ferritic and austenitic tube materials when exposed to the action of steam at high temperatures and under pressure. The test units for this program are installed at the Philip Sporn Station of American Electric Power Service Corporation near Pomeroy, Ohio. In this research, selected materials in tubular form are subjected to high-pressure steam (2000-psi) at temperatures of 1100 to 1500 F for time periods up to 36 months to determine the resistance to corrosion and creep, the effects of oxide films on thermal conductivity, the metallurgical stability, and the resistance to thermal shock. The test tubes are exposed to air on the outside and there is no temperature gradient across the tube wall. The present paper is concerned with the metallurgical aspects of this program.

Two papers have already been presented before The American Society of Mechanical Engineers on certain phases of the ASME Research Committee on High Temperature Steam Generation program to determine the performance characteristics of selected ferritic and austenitic tube materials when exposed to the action of steam at high temperatures and under pressure. At the 1951 Annual Meeting,[5] the apparatus constructed for this program was described in detail,[6] while at the 1955 Annual Meeting, results of tests on the first prototype unit were given.[6] A schematic arrangement of the test installation and a typical section of a test rack are reproduced in Figs. 1 and 2. Five units are involved with the two containing the ferritic tube materials operating at 1100 and 1200 F, and the three with the austenitic tubes at 1200, 1350, and 1500 F. The steam pressure in each unit is approximately 2000 psi and the tubes are 2-in. OD × 1/8-in. wall × 42-in. long. The internal and external surfaces were as would be normally supplied to ASTM Specification A213. The type of steels tested and their arrangement within the unit are shown in Fig. 3.

The tube dimensions were arbitrarily selected. The size was considered representative of that generally used in superheaters; and all specimens were made identical to facilitate the final scale analyses.

As a result of this arbitrary selection, it is evident that all tubes are subject to the same stress and, thus depending upon the materials selected and the operating temperatures, the expected life of the specimens will vary considerably.

The pressure stress was established on the basis of the Barlow formula

$$s = \frac{PD}{2t}$$

where

s = stress, psi
P = pressure, psi
D = inside diameter, in.
t = tube-wall thickness, in.

Thus for the steam pressure of 2000 psi established for this research, the tubular specimens are subjected to a stress of 2000 psi.

The long-time strength properties of the materials were based on data published by The Babcock & Wilcox Company, The Timken Roller Bearing Company, and The United States Steel Corporation. Two criteria were used in selecting the materials for the test rack. First, the expected stress of 2000 psi was compared with the stress required to produce a creep rate of 0.02 per cent in 1000 hr and, secondly, the expected stress was compared with 80 per cent of the stress necessary to produce rupture in 25,000 hr. However, in the final selection, some of the materials selected did not meet these criteria, and a calculated risk was taken in the decision to include such materials in the test racks.

After the first six-months' operation, the first set of tubes, designated as Selection A of Fig. 3, was removed from each unit and the present paper compares the metallurgical characteristics of these tubes with those of the original materials and also presents findings with respect to the degree of tube swelling and the magnitude and type of attack on both the OD and ID surfaces.

Operating and Test Procedure

The operating conditions during the first six months of operation at the Philip Sporn Power Plant were as follows:

	Test units				
	No. 1	No. 2	No. 2A	No. 3	No. 4
Inlet-probe reading, deg F	1106	1201	1206	1353	1497
[a]Average tube-metal temperature, deg F	1093	1197	1194	1350	1494
Outlet-probe reading, deg F	1099	1194	1202	1341	1485
Average inlet steam pressure, psig		2005			
[b]Average outlet steam pressure, psig		1500			
Average flow rate, lb per hr		830			

[a] In soot-blower section, average metal-temperature drop 45 F during 10-sec blow.

[b] The pressure in the 1500-F unit is between 1500 and 2000 psi, because of the pressure drop through the test assembly.

---

[1] Staff Metallurgical Engineer, Steel and Tube Division, The Timken Roller Bearing Company, Canton, Ohio. Mem. ASME.

[2] Chief Metallurgist, Tubular Products Division, The Babcock & Wilcox Company, Beaver Falls, Pa. Mem. ASME.

[3] Chief Metallurgist, National Tube Division, United States Steel Corporation, Pittsburgh, Pa.

[4] Supervisor, Power Applications Section, The International Nickel Company, Inc., New York, N. Y.

[5] B. Ronay, "Evaluation of Superheater Tube Materials for Steam Generation at 1100 to 1500 F."

[6] B. Ronay, W. E. Clautice, and W. F. Erskine, "Evaluation of Prototype Unit for the ASME High-Temperature Steam Generation Investigation," ASME Paper No. 55—A-63.

Contributed by the Research Committee on High Temperature Steam Generation of THE AMERICAN SOCIETY OF MECHANICAL ENGINEERS and presented at the ASME-AIEE National Power Conference, Kansas City, Mo., September 28–October 1, 1959.

NOTE: Statements and opinions advanced in papers are to be understood as individual expressions of their authors and not those of the Society. Manuscript received at ASME Headquarters, June 24, 1959. Paper No. 59—Pwr-1.

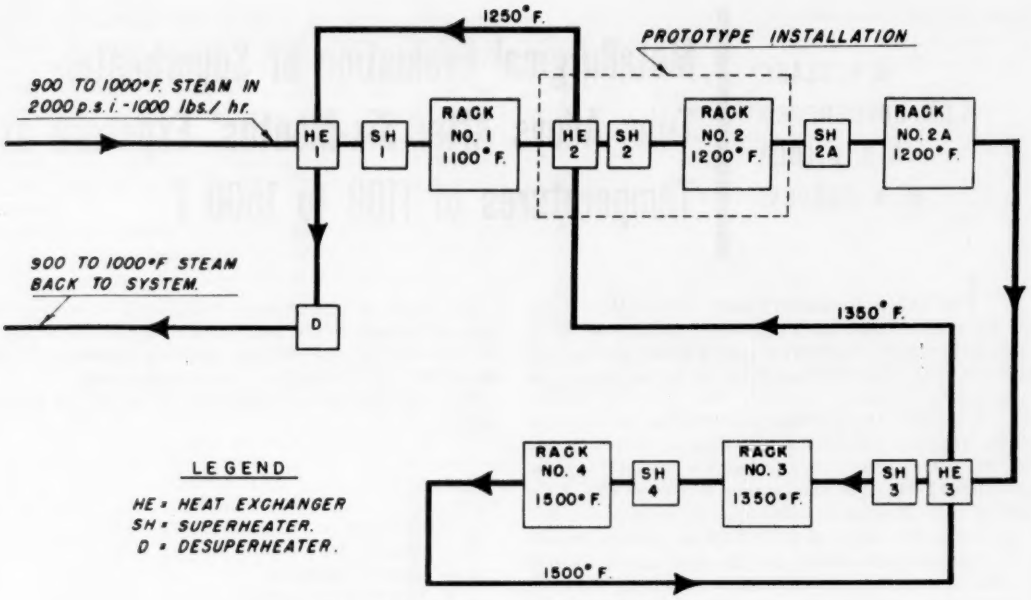

Fig. 1 Schematic arrangement of test installation

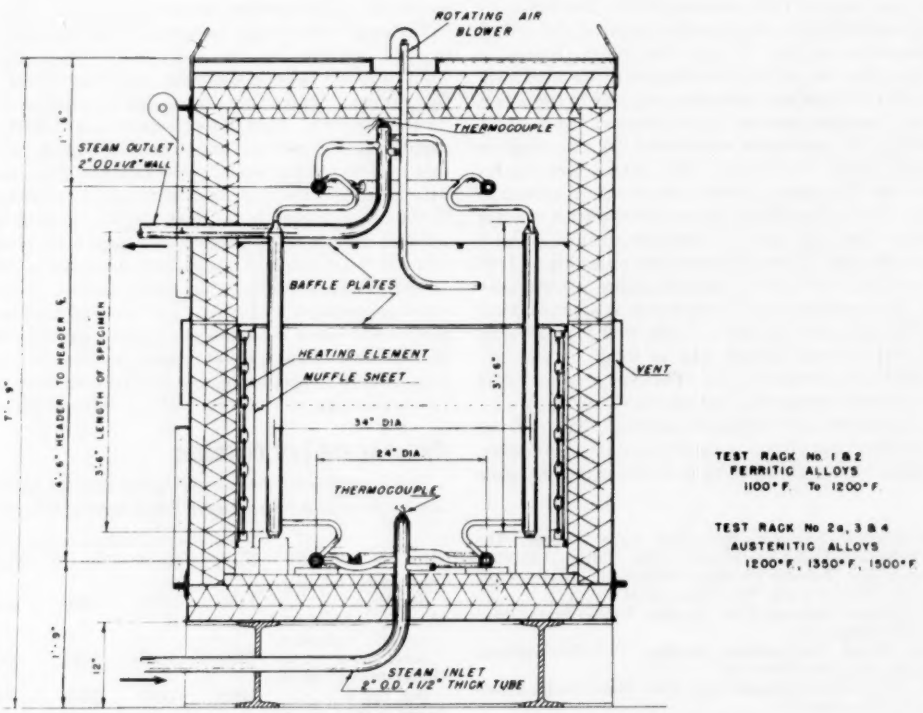

Fig. 2 Typical section of test rack

As would be expected for a program of this type, the operation for the first six months was not continuous. The boiler furnishing steam was out of service part of the time, for various reasons. There also were failures in the 1500-F test unit. These failures will be discussed later.

The metallurgical examination of the tubes removed was under the supervision of the metallurgical subgroup of the committee and was done on a co-operative basis. The testing program undertaken on the tubes before and after exposure is given in Table 1. This table also lists the co-operating laboratories and shows the type of steel assigned to each. All testing details were in accordance with ASTM Specification A370.

Fig. 4 shows a photograph of one of the tube elements with the end connections and the section exposed to the soot-blower

A) Type Steels Tested In Experimental Units

Unit No. 1	Unit No. 2	Unit No. 2A	Unit No. 3	Unit No. 4
1100°F	1200°F	1200°F	1350°F	1500°F
1. Cr-Mo-V			TP 304 (18 Cr - 8 Ni)	
2. 2-1/4 Cr - 1 Mo			TP 347 (304+Cb)	
3. 5 Cr Mo + Ti			TP 321 (304+Ti)	
4. 2-1/4 Cr - 1 Mo*			TP 316 (16 Cr - 13 Ni+Mo)	
5. 5 Cr Mo			TP 310 (25 Cr - 20 Ni)	
6. 9 Cr Mo			16 Cr - 25 Ni - 6 Mo	
7. 5 Cr Mo*			17 Cr - 14 Ni + Cu + Mo	
8. 3 Cr - 1 Mo			15 Cr - 15 Ni + Nitrogen	
9. 5 Cr Mo + Si			Inconel (15 Cr - 78 Ni)	
10. 5 Cr Mo + Ti*			Incoloy (20 Cr - 32 Ni)	

*Welded at center of length with manual deposit.

Note: 1) Complete chemical analyses and details with respect to heat treatment and mechanical properties given in Figures ( ) through ( ) of the Appendix.

2) Tubes are 2.000" OD by 0.500" wall and were produced in accordance with ASTM Specification A213 (SA 213)

B) Arrangement Of Tubes In Unit

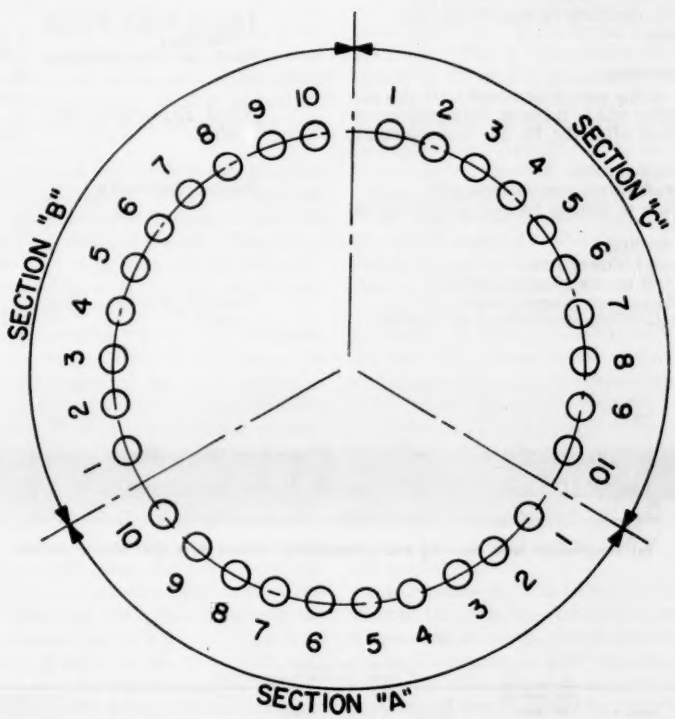

Fig. 3 Type steels tested and arrangement in the test units

action; and a schematic diagram for the location of the specimens required for the metallurgical examination. The particular tube element shown contains a center weld, and from Fig. 3, it will be noted that three tubes with center welds were installed in the ferritic-tube units.

Test Results

The results obtained from the metallurgical examination before and after the six-months' exposure at the designated temperatures are summarized for each of the individual steels in Tables 4 through 20 of the Appendix. Similar data with reference to each of the individual failures to date are given in Figs. 12 to 16, inclusive of the Appendix

Visual Examination. Representative outside surface appearances of two ferritic tubes after the exposure in air at 1100 and 1200 F are shown in Fig. 5 and of two austenitic steels after exposure at 1200, 1350, and 1500 F in Fig. 6. Unfortunately, surface details can not be shown too clearly by photographs and accordingly the following comments as to the conditions are included.

Visual inspection at the outer surface of the 1100-F test unit indicated the titanium and silicon modifications of the 5-Cr Mo steel scaled the least amount while the 9-Cr 1-Mo steel was second best. The most heavily scaled appeared to be the $2^1/_4$-Cr 1-Mo and the Cr-Mo-V tubes. However, in no case was the scaling very heavy and subsequent microscopic examination revealed it to be of the order of 0.005 in.

Inspection of the 1200-F ferritic test unit again indicated the titanium modification of 5-Cr Mo steel scaled the least amount but the 9-Cr 1-Mo steel appeared to be slightly superior to 5-Cr

Table 1 Outline of tests conducted on tubes before and after exposure

I Tests on original tubes
- A Tensile tests (duplicate 0.357-in. diam × $1^1/_2$-in. gage from tube wall)
  - 1 Room temperature
  - 2 Proposed operating temperatures (1100, 1200, 1300, 1500 F)
- B Charpy impact tests (0.394-in-sq V notch)
  - 1 Room temperature
  - 2 Proposed operating temperature
- C Hardness (Brinell on cross section)
- D Microexamination
  - 1 Structure
  - 2 Decarburization
  - 3 Grain size (structural and McQuaid-Ehn)
- E Flattening test (to complete flatness) (1-in. ring)
- F Size measurements

II Tests on tubes after exposure

Based upon a review of the results obtained after the six-month period, a decision will be made on the completeness of the testing required after the 18, 24, and 36-month periods.
- A All tests as for original tubes
- B Examination of racks after removal from unit
- C Visual examination of general surface conditions—4-in. length
  - 1 Incipient cracking
  - 2 Scaling at soot-blower area
- D Scale thickness and nature of attack (micro)
  - 1 Intergranular versus general attack
- E Heat-transfer tests—Professor Solberg at Purdue

III Assignment of work to co-operating laboratories

International Nickel Company, Inc.	Inconel	—3 tubes
	Incoloy	—3 tubes
	Type 304	—3 tubes
	Type 310	—3 tubes
Babcock & Wilcox Company	$2^1/_4$-Cr 1-Mo	—2 tubes
	9-Cr 1-Mo	—2 tubes
	15-15N	—3 tubes
	Type 321	—3 tubes
National Tube Division United States Steel Corporation	5-Cr $^1/_2$-Mo	—2 tubes
	3-Cr 1-Mo	—2 tubes
	Type 347	—3 tubes
	Type 316	—3 tubes
	Cr-Mo-V	—1 tube
Timken Roller Bearing Company Steel and Tube Division	5 Cr-Mo-Ti	—2 tubes
	5 Cr-Mo-Si	—2 tubes
	16-25-6	—3 tubes
	Armco 17-14 Cu-Mo	—3 tubes
Naval Experiment Station	All welds (seven tubes plus goosenecks and header welds)	
Purdue University	All tubes to be tested for heat-transfer properties. 24-in. piece required. These will then be available to the above laboratories for tensile, impact, and other tests.	
General Electric Company	Analysis of scale	

(a) Superheater tube showing end connections; section A is soot blower section

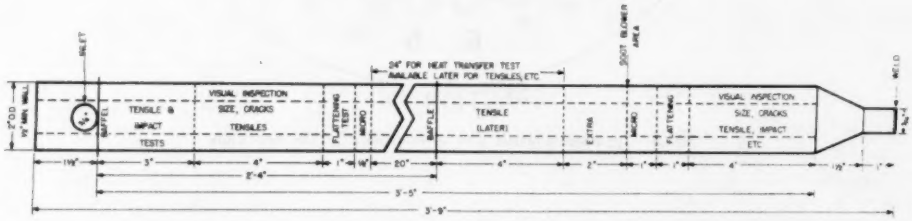

(b) Schematic diagram for location of test specimens after exposure

Fig. 4 Photograph of superheater element and sketch showing test specimen location

Table 2 Scaling characteristics of superheater-tube materials based on scale accumulation in tubes

A Height of scale deposit in tubes, in.

	Height of scale deposit in tubes			
	1350 F		1500 F	
Type alloy	Section B	Section C	Section B	Section C
304	*	*	?	$5\frac{1}{2}$
347	*	*	*	*
321	*	*	*	Slight
316	*	*	*	$\frac{1}{4}$
310	*	*	Tubes removed	
16-25-6	*	*	*	*
17-14 Cu-Mo	*	$3\frac{1}{8}$	*	*
15-15N	$8\frac{1}{2}$	$7\frac{1}{2}$	$9\frac{1}{4}$	$\frac{7}{8}$
Inconel	*	*	$\frac{3}{4}$	Slight
Incoloy	*	*	*	$1\frac{1}{2}$

*No measurable scale was detected by radiographic examination of tubes where no value is shown. In the radiographic examination, exposure was determined for 1-in. total thickness, 18-in. focal distance, 200 mg radium, aiming for film density of about 1.5.

B Analyses of the scale samples

Type alloy	Temp, deg F	Al	Mo	Cu	Si	Cr	Cb	Ti	Ni	Mn
15-15N	1200	0.01	0.04	0.05	0.03	0.22	*	0.01	0.90	0.60
	1350	0.01	0.38	0.06	0.01	0.63	*	0.01	2.90	0.90
	1500	0.02	0.60	0.15	0.15	12.50	0.35	0.03	8.50	0.94
304	1500	0.01	0.09	0.26	0.11	14.50	*	0.01	6.20	1.05
316	1500	0.02	0.85	0.18	0.13	19.00	*	0.01	8.70	1.30
17-14 Cu-Mo	1350	0.01	0.09	0.20	0.01	1.00	*	0.03	2.30	0.52

C Magnetic and microscopic examination

In all ten samples examined, the scale appeared homogeneous, black or gray-black in color, flaky, and hard. The samples were magnetic, indicating the main constituent present to be iron.

Mo + Si. The most heavily scaled appeared to be the 5-Cr Mo, $2\frac{1}{4}$-Cr 1-Mo, and Cr-Mo-V tubes. Evidently the nature of the scale formed, that is, whether it is dense and adherent or tends to be flaky, greatly affects the visual appearance. Microscopic examination showed the thickness of scale to range from 0.010 to 0.017 in. with the 9-Cr 1-Mo showing the least, and the $2\frac{1}{4}$-Cr 1-Mo tube the greatest thickness.

The only distinguishing feature of the tubes in the austenitic units was the fact that the 16-25-6 tube in the 1500-F unit was heavily scaled and pitted around the weld at the inlet end and also exhibited a number of slight blisters over its length. The pitting might have resulted from weld slag, incompletely removed. Microscopic examination showed the scale thickness on the outside of these tubes to be the order of 0.001 in. or less.

The inside surface of two representative ferritic tubes is shown in Fig. 7 and of two austenitic tubes in Fig. 8. Insofar as the ferritic tubes are concerned, the scaling on the inside surface resulting from steam attack was of the same order of magnitude as the air attack on the outside. Likewise, the scale formed must have been adherent for no appreciable amount of loose scale was found in any of these tubes.

While microscopic examination indicated the scale formation on the inside surface of the austenitic tubes to be of a low order of magnitude, it was found that certain of these tubes contained appreciable amounts of loose scale when the units were dismantled. Consequently an x-ray examination was made of the tubes in Section B and C to determine the height of the scale deposits. These results are summarized in Table 2. The tube showing the maximum amount of scale was 15-15N at both 1350 and 1500 F. The only other tube showing measurable scale at 1350 F was 17-14 Cu-Mo while at 1500 F the 18-8 tube in Section C scaled appreciably. The analyses of the scales, also given in Table 2, show the scale formed at 1500 F came from the tubes indicated and was not carried over from one tube to another. No ready association can be made with the scale formed at the other temperatures. Before the units were restarted for the second six-months' exposure, the scale was removed from Sections B and C through a drilled hole at the base of the tube containing scale.

Scale-thickness measurements made on both the air and steam side of two of the ferritic and two of the austenitic tubes are given in Fig. 9. This shows that there is no significant difference in the scaling resistance in steam and air at 1100 F between $2\frac{1}{4}$-Cr 1-Mo and 9-Cr 1-Mo, whereas at 1200 F there is a considerable difference between these two materials. This figure also shows type 321 is more resistant to scaling than 15-15N in both air and steam at 1200 to 1500 F.

Tensile Properties. Room-temperature and elevated-temperature tensile tests at the exposure temperatures were conducted on the original tubes and also after the six-months' exposure time. The results, for each of the individual steels, are contained in Tables 4 through 20 of the Appendix.

The exposure conditions had little influence on the tensile or yield-strength values at either room or elevated temperatures but did have an influence on the ductility values of certain of the steels, especially at room temperature after exposure at the elevated temperatures. This condition is illustrated by Fig. 10, which is based on the elongation values. The two steels showing the greatest loss in room-temperature ductility after exposure at elevated temperatures are type 310 and 16-25-6. The high-temperature exposure likewise reduced the elongation values at elevated temperatures of certain of the alloys, and especially Incoloy and 17-14 Cu-Mo at 1350 F and 17-14 Cu-Mo and type 310 at 1500 F.

Impact Resistance. The six-months' exposure time had a marked effect on the shock resistance of certain of the alloys, both at room temperature after exposure at elevated temperatures and at the elevated temperatures after exposure. This condition is shown in Fig. 11. The alloys showing the greatest decrease in room-temperature impact resistance after exposure at elevated temperatures were 16-25-6, type 310, 15-15N, and 17-14 Cu-Mo. These same alloys likewise showed the greatest loss in high-temperature impact resistance after the six-months' exposure. For both of these conditions, Incoloy showed its minimum resistance after the 1200-F exposure.

Flattening Characteristics. All of the tubes considered met the flattening requirements of ASTM Specification A213 in the origi-

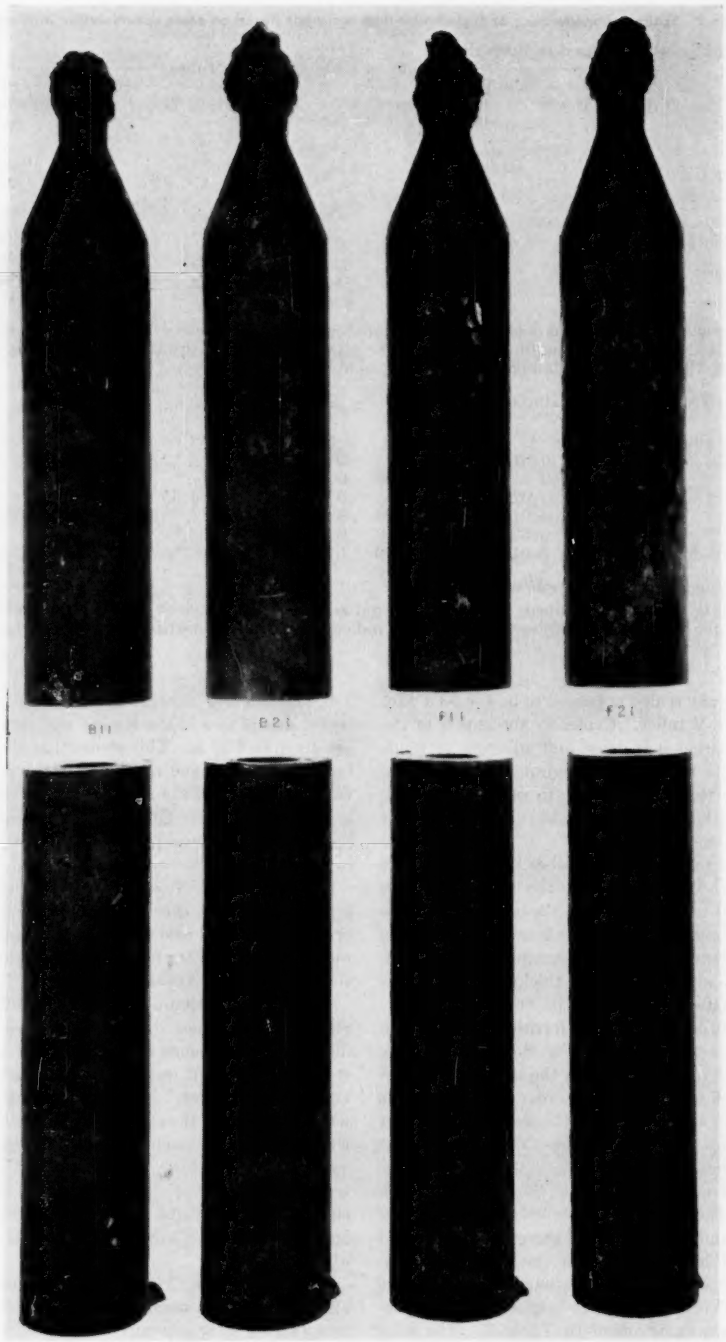

Fig. 5 Photograph showing outside surface of representative ferritic tubes after six-months' exposure at 1100 and 1200 F

(B11, B21, 5-Cr Mo Ti, after 1100 and 1200 F, respectively. F11, F21, 5-Cr Mo Si, after 1100 and 1200 F, respectively.)

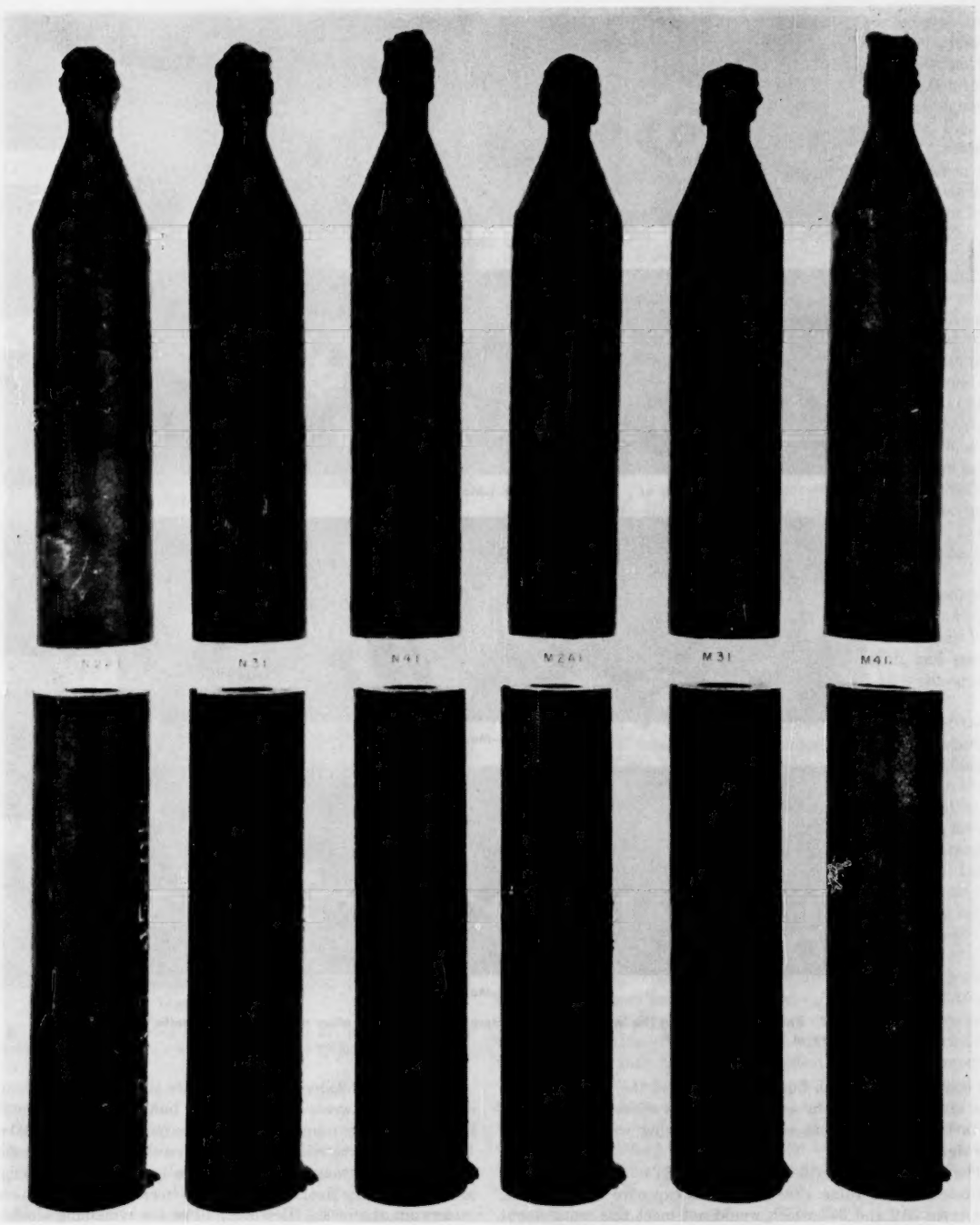

Fig. 6 Photograph showing outside surface of representative austenitic tubes after six-months' exposure at 1200, 1350, and 1500 F (M2, M3, M4, 16-25-6, after 1200, 1350, and 1500 F, respectively. N2, N3, N4, 17-14 Cu-Mo after 1200, 1350, and 1500 F, respectively.)

(a) $2^1/_4$-Cr 1-Mo, 1100 F

(b) $2^1/_4$-Cr 1-Mo, 1200 F

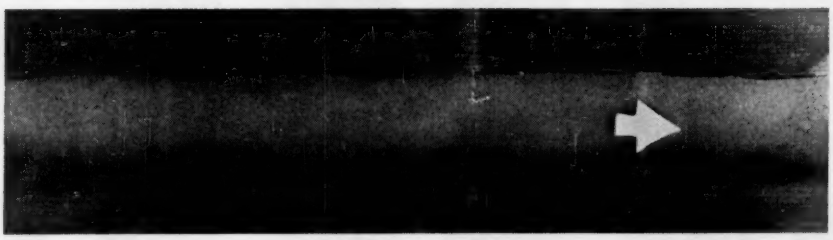

(c) 9-Cr 1-Mo, 1100 F

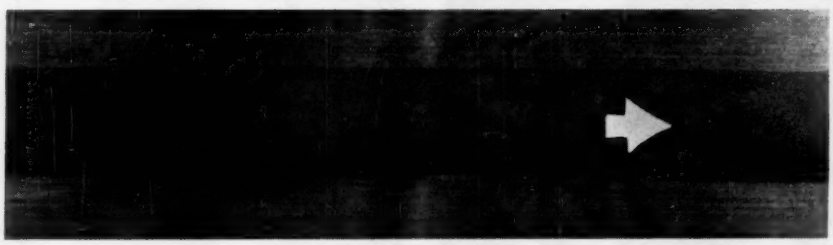

(d) 9-Cr 1-Mo, 1200 F

Fig. 7 Photograph showing the inside surface of representative ferritic alloy tubes after six-months' exposure at 1100 and 1200 F

nal condition and, with but few exceptions, the same was also true after the six-months' exposure at the various temperatures. In fact, most underwent complete flattening without showing any signs of cracking.

The exceptions were 16-25-6, which could not be flattened to the calculated H value after any of the exposure temperatures, and types 310 and 347 which would not meet this requirement after the 1500-F exposure. The silicon modification of 5-Cr Mo satisfactorily met the H value but could not be completely flattened without cracking.

Bulging During Exposure Tests. Measurements of the tubes after the exposure tests, as well as the calculated per cent deformation of the OD's are given in the figures of the Appendix and some are included in Table 3. Table 3 also includes the available creep (0.01 per cent per 1000 hr) and 100,000-hr rupture-strength values, as taken from the literature, for the ferritic steels at 1100 and 1200 F and the austenitic steels at 1350 and 1500 F.

The values of Table 3 would indicate that there is no definite relationship between the amount of bulging and the reported high-temperature properties. With the ferritic steels at 1100 and 1200 F a certain correlation exists in that the alloy with the maximum rupture strength underwent the least amount of bulging and at 1200 F the steel with the lowest creep and rupture strength underwent the most. However, all of the remaining steels did not align themselves in proper order. With the austenitic steels, the correlation was less definite.

The lack of a more definite correlation may be a result of several factors such as: (*a*) The magnitude of the values involved, (*b*) uncertainties with respect to the actual diameter of the original tubes, (*c*) possible scale effects influencing the readings, and (*d*) the high-temperature data used for comparison not being representative of the test specimens. A more definite correlation may exist after the second six-months' exposure.

Failures During Test. To date several tubes have failed by ruptur-

(a) Type TP321, 1200 F

(b) Type TP321, 1350 F

(c) Type TP321, 1500 F

(d) Type 15-15N, 1200 F

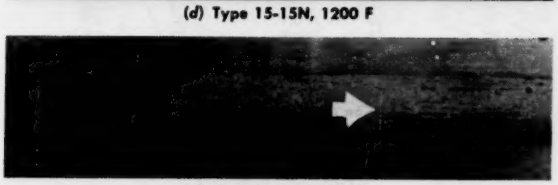

(e) Type 15-15N, 1350 F

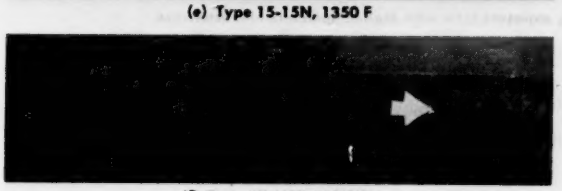

(f) Type 15-15N, 1500 F

Fig. 8 Photograph showing the inside surface of representative and austenitic alloy tubes after six-months' exposure at 1200, 1350, and 1500 F

ing, or excessive bulging, but all, with one exception, have been confined to the 1500-F test unit. Likewise there was one failure of a section of the type 316 connecting pipe Details with respect to these failures are given in Figs. 12 to 16 of the Appendix.

The one failure not in the 1500-F test unit was one of the 5-Cr Mo + Ti tubes tested at 1200 F. As shown in Fig. 12 this failure resulted from a marked defect on the ID of the tube and was not caused by this alloy having insufficient strength under the given test conditions. The room-temperature mechanical properties of the failed tube were identical to those of the original material. The remaining two tubes of this analysis are still under test.

Failure by cracking of one of the type 347 tubes occurred at 2178 hr and the other two tubes of this analysis were bulged to such an extent (about 7 per cent) that they were removed from the unit.

One of the type 310 tubes failed by cracking after about 3000 hr. From Fig. 13 it will be seen that a series of cracks occurred, that sigma was formed, and that there was a marked pick-up of nitrogen on the outer surface. Likewise the room-temperature physical properties were changed, with both the ductility and impact resistance being greatly reduced. The remaining two tubes of this analysis were also removed because of excessive bulging.

A type 321 tube failed, by cracking, after 6812 hr, Fig. 14. In sections removed from the actual failure, there was considerable cracking on both the OD and ID and, as in the case of the type 310 tube, marked nitrogen pick-up on the outer surface. The deformation to failure was 5.0 per cent and the room temperature properties were not appreciably influenced. The remaining two tubes are still under test.

A 17-14 Cu-Mo tube likewise failed by cracking after 6812 hr, Fig. 15. The deformation to failure was 3.8 per cent and room-temperature impact resistance was decreased. The nitrogen pick-up at the surface was not as pronounced as with the type 310 and 321 tubes. The remaining two tubes are still under test.

The Incoloy and Inconel alloy tubes were removed from the 1500-F unit because of excessive enlargement. One tube of each was reinstalled to verify the findings on these compositions.

A section of the type 316 connecting pipe failed, Fig. 16, after 6812 hr in a very ductile manner, its elongation to fracture being 39 8 per cent. The grain size was extremely fine and there is a question as to whether or not this pipe was heat-treated so as to develop maximum strength at elevated temperatures. Large amounts of the sigma phase were formed and there was a marked pick-up of nitrogen at the outer surface.

In addition to the preceding failures resulting from insufficient strength, or in one case to a defective tube, a rather unusual failure occurred in 16-25-6 as a result of the thermocouple's protective coating (Sauereisen cement) reacting with and eating through the tube wall. This hole was repaired by welding and this tube is still under test.

There appears to be no correlation between the time of these failures and the reported high-temperature strength characteristics given in Table 3. This probably would not be true if high-temperature data were available on the actual tubes used in these tests. The type 347 and 310 tubes in the 1500-F unit failed in approximately the same time. Yet type 347 has one of the lowest rupture strengths at 1500 F and type 310 about the same strength as type 316, yet none of the type 316 elements have failed. Likewise 17-14 Cu-Mo has the highest rupture strength and one of these tubes failed in 6812 hr, while none of the type 304 tubes have, even though the reported rupture strengh for type 304 is much lower.

The lack of agreement between the failures and the high-temperature data may result in part from differences in heat-treatment. Unfortunately, exact data are not available with respect to the heat-treatment given the tubes and it is now known that heat-treatment may have a marked effect on the high-temperature-strength characteristics. However, the microstructures of the tubes that have failed, with the exception of the type 316 connecting pipe, would indicate that a satisfactory temperature was used for solution treating. All the tubes were heat-treated in accordance with standard commercial practice for ASTM Specification A213.

Conclusions

The results from the visual and metallurgical examination after the first six-months' exposure permit the following conclusions:

1 Visual examination indicated differences in the appearance of the scale on the outside surface of the ferritic tubes after exposure at 1100 and 1200 F but microexamination indicated relatively slight differences in the amount of actual attack, especially at 1100 F. At 1200 F the measured depth of scale for these steels varied from 0.010 to 0.017 in. with 9-Cr 1-Mo showing the

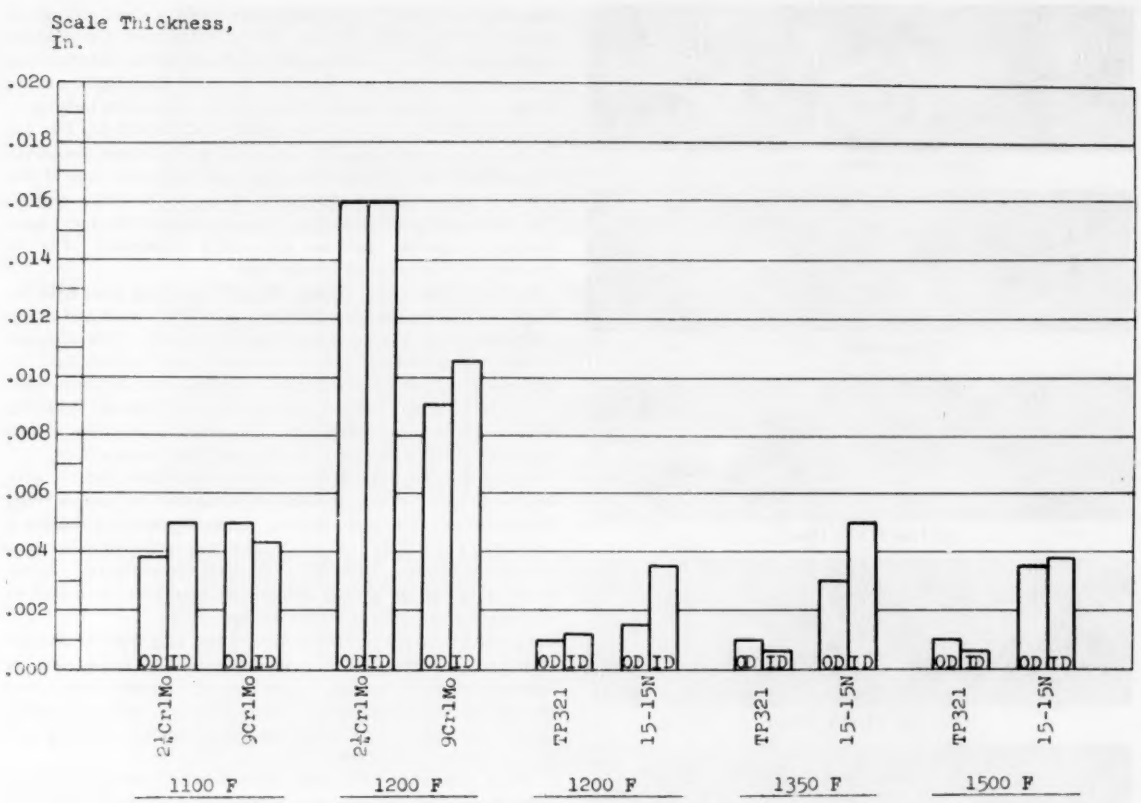

Fig. 9 Steam oxidation of some superheater materials after six-months' operation (ASME steam research)

Table 3 Comparison of maximum tube bulging during exposure tests with high-temperature characteristics

A Ferritic steels

	1100-F exposure tests			1200-F exposure tests		
	Max OD exp. %	Creep strength 0.01%/1000 hr	100,000-hr rupture strength	Max OD exp. %	Creep strength 0.01%/1000 hr	100,000-hr rupture strength
2¼-Cr 1-Mo	0.15	3600	8200	0.95	2150	4500
Cr-Mo-V	0.60	...	...	...	...	...
3-Cr Mo	0.80	3600	5400	1.30	1240	...
5-Cr Mo	0.90	3200	6700	1.50	1700	3000
5-Cr Mo+ Ti	0.60	3500	4000	3.80	850	1925
5-Cr Mo+Si	0.60	2600	5400	1.70	1600	3100
9-Cr 1-Mo	0.60	4100	7800	0.70	2100	4600

B Austenitic alloys

	1350-F exposure tests			1500-F exposure tests		
304	1.00	2150	3150	1.26	1450	1700
310	0.20	3500	3600	2.76	1250	1600
316	...	3500	5500	...	1800	1600
321	0.10	2500	2500	...	625	1250
347	0.40	3000	5000	7.00	625	1250
15-15N	...	...	10000	...	...	4600
17-14 Cu-Mo	0.30	...	9500	0.50	...	5500
16-25-6	0.50	...	6250	0.70	3000	3300
Incoloy	...	...	...	...	...	...
Inconel	...	...	...	...	...	...

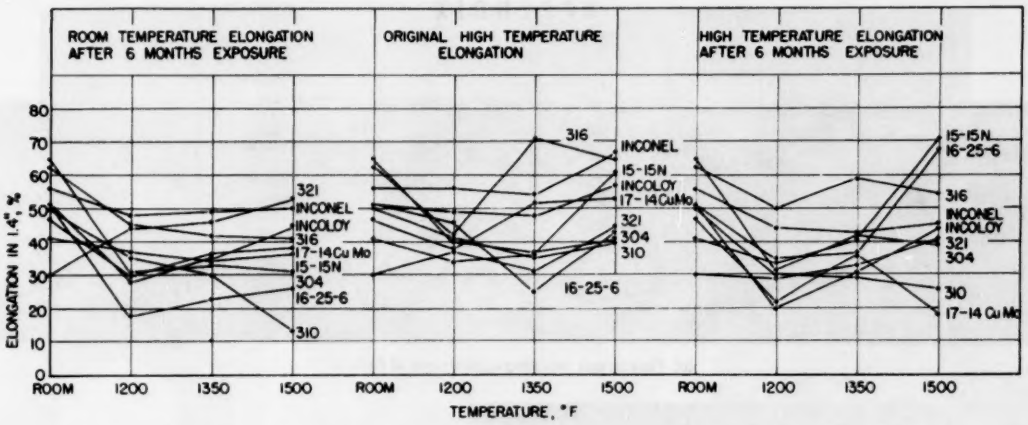

Fig. 10 Short time elongation values of austenitic steels before and after exposure at 1200, 1350, and 1500 F

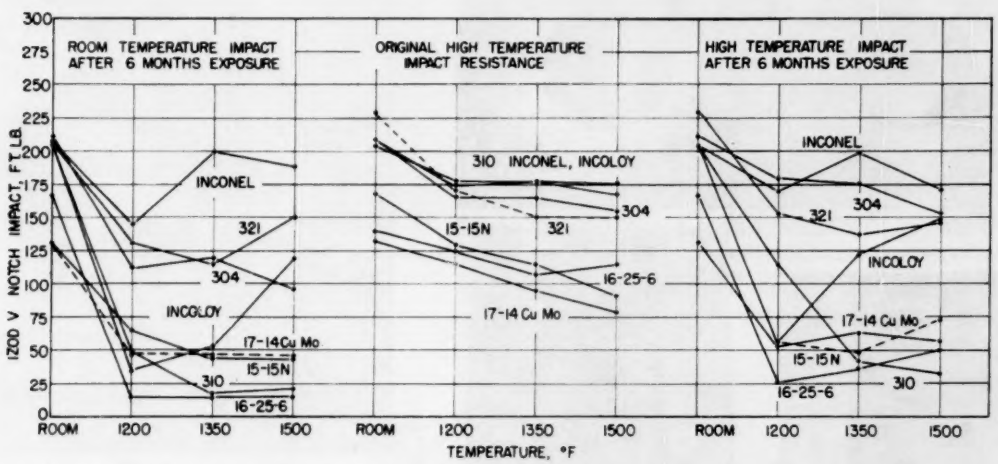

Fig. 11 Impact characteristics of austenitic steels before and after exposure at 1200, 1350, and 1500 F

least and $2^1/_4$-Cr 1-Mo the greatest amount of scaling. At both temperatures the scale thickness on the ID was comparable to that on the OD. This is in agreement with the known effect of increasing chromium content in improving the resistance to scaling in both air and steam, especially at temperatures in excess of 1100 F.

2 With the austenitic steels the scale on the OD was slight at each of the three temperatures. While visual appearance of the ID indicated little attack, certain of the tubes, especially 15-15N at 1350 and 1500 F, contained several inches of flaky scale, thus indicating appreciable attack by the steam.

3 The mechanical properties of the ferritic steels were not appreciably changed during exposure at 1100 and 1200 F. The same was also true of the austenitic steels with respect to their tensile and yield-strength values. However, with certain of the austenitic steels, a marked decrease occurred in the room-temperature-ductility and impact properties as a result of exposure at the elevated temperatures. The steels undergoing the greatest changes were 16-25-6, type 310, 15-15N, and 17-14 Cu-Mo.

4 A definite correlation was not found to exist between the high-temperature rupture properties and the degree of bulging or, in the case of the tubes that have rupture, in the rupture time.

5 To date failures have occurred in the 1500-F tests of type 347 and 310 and the remaining tubes of these analyses were removed because of excessive bulging. Incoloy and Inconel alloys were also removed because of excessive bulging. One tube of type 321 and 17-14 Cu-Mo have likewise failed but the two remaining tubes of each of these analyses are still under test.

6 All of the austenitic tubes that failed in the 1500-F test unit showed a marked nitrogen pick-up on the surface and this probably accounted for some, at least, of the shallow-OD cracking visible on the macro sections. There is a question if this same condition would occur in combustion gases.

These conclusions apply only to the given test conditions. With higher rates of steam flow through the tubes, or with combustion gases on the outside of the tubes, different results may have been obtained

APPENDIX

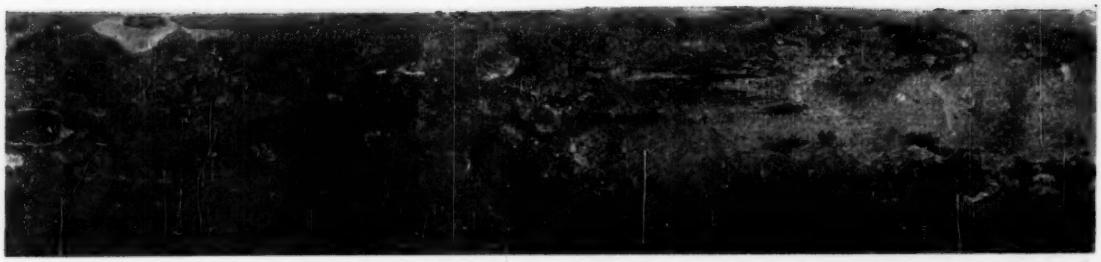

(a) Photograph showing appearance of failure

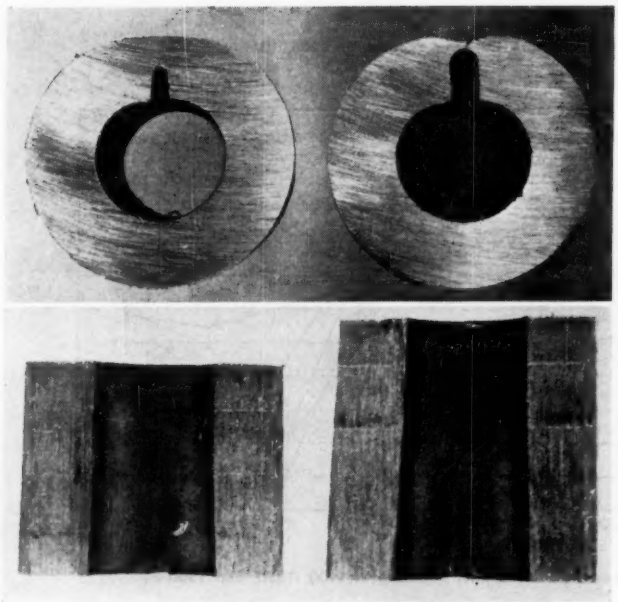

(b) Tube sections showing type failure

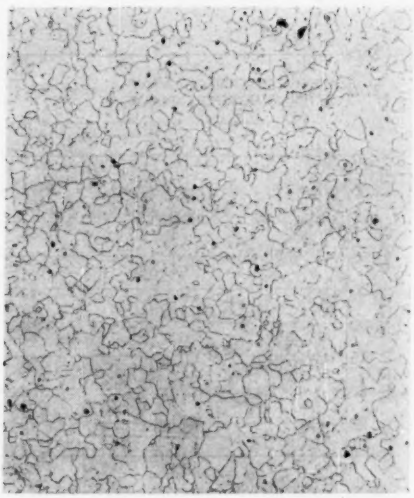

(c) General microstructure of tube, X100, nital etch

(d) Room temperature properties before and after failure

	Tensile strength, psi	Yield (0.2%), psi	Elongation in 1.5″, %	Reduction of area, %	Brinell hardness	Charpy V notch, ft-lb	Maximum OD expansion, %
Original tube	60,000	25,750	46	76	115	238, 236, 244	...
Failed tube	59,000	25,000	43	85	115	224, 237, 254	5.7

Fig. 12 Data on 5-CrMo Ti tube which failed in the 1200 F superheater unit

(a) Photograph showing appearance of the failure

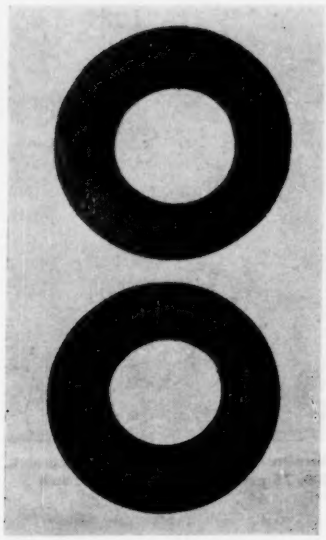

(b) Macrostructure showing extent of cracking

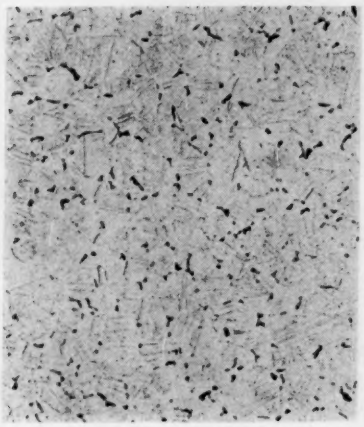

(c) Microstructure showing sigma formation, ×100

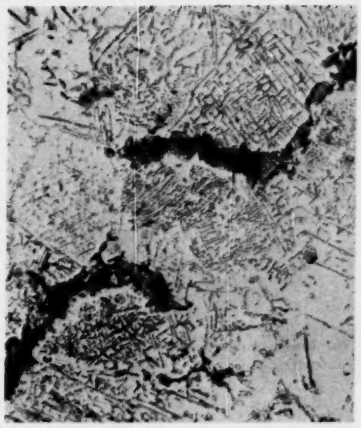

(d) Microstructure showing nitrogen pick-up at surface; nitrogen content 0.394 per cent, tube proper, 0.058 per cent, ×500, chromic acid, electrolytic etch

(e) Room temperature properties before and after failure

	Tensile strength, psi	Yield (0.2%), psi	Elongation in 1.5", %	Reduction of area, %	Brinell hardness	Charpy V notch, ft-lb	Maximum OD expansion, %
Original tube	84,500	32,750	50	74	128	206, 204, 206	...
Failed tube	82,000	35,000	33	31	143	20, 19, 18	9.75

Fig. 13 Data on 310 tube which failed after about 3000 hr at 1500 F

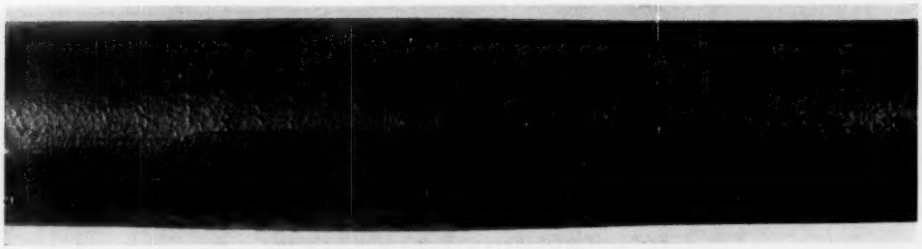

(a) Photograph showing appearance of the failure

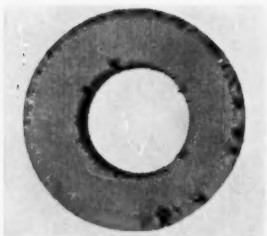

(b) Macrostructure showing extent of cracking

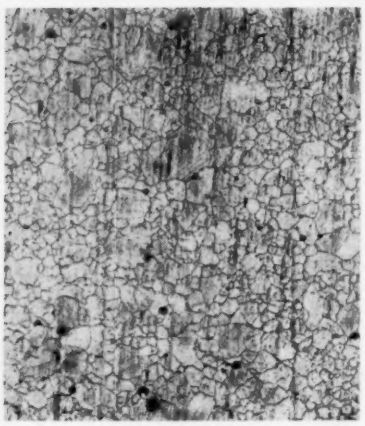

(c) Microstructure of failed tube GS 5/8 (4), ×100

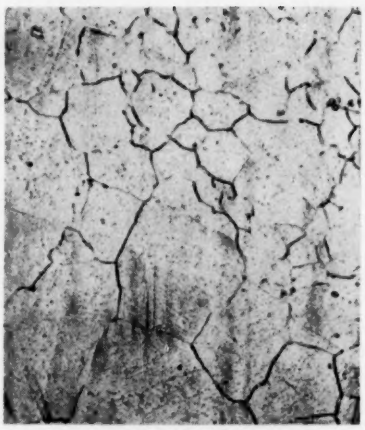

(d) Microstructure showing cold work in grains, ×1000, 75 per cent nitric electrolytic etch

(e) Nitrogen pick-up at surface

Original	−0.017%
After exposure	−0.210%

(f) Properties before and after failure

	Test temp.	Tensile strength, psi	Yield (0.2%), psi	Elongation in 1.5", %	Reduction of area, %	Brinell hardness	Charpy V notch, ft-lb	Maximum OD expansion, %
Original	Room							
Failed	Room	76,600	31,000	52.0	73.0	124	165, 216	5.0
Original	1500							
Failed	1500	22,000	14,000	41.0	39.0			

Fig. 14 Data on type 321 tube which failed after 6812 hr at 1500 F

(a) Photograph showing appearance of the failure

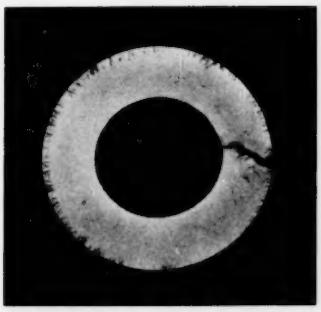

(b) Macrostructure showing extent of cracking, 0.10 per cent N_2 at surface

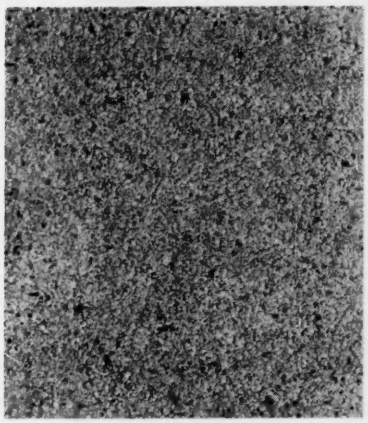

×100

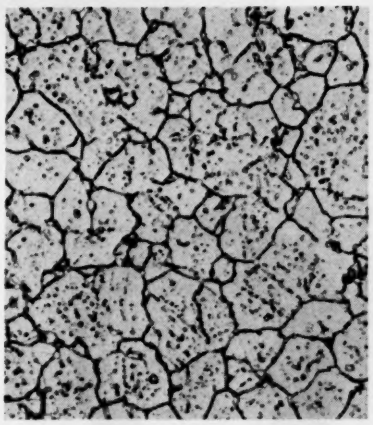

×1000

(c) Microstructure of failed tube, glyceregia etch

(d) Properties before and after failure

	Test temp.	Tensile strength, psi	Yield (0.2%), psi	Elongation in 1.5″, %	Reduction of area, %	Brinell hardness	Charpy V notch, ft-lbs	Maximum OD expansion, %
Original	Room	89,250	45,500	46.8	67.7	143	132	
Failed	Room	84,000	38,500	38.0	51.0	143	40, 36, 40	3.8
Original	1500	27,600	22,300	53.0	58.0		81, 80, 72	
Failed	1500	22,000	17,000	12.0	15.0			

Fig. 15 Data on 17-14 Cu Mo tube which failed after 6812 hr at 1500 F

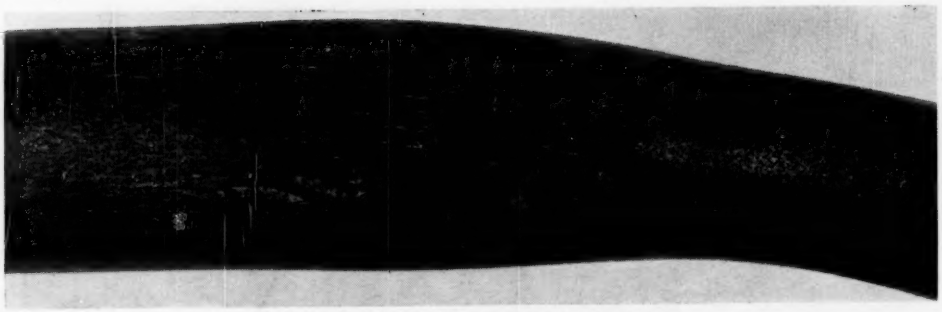

(a) Photograph showing appearance of the failure

(b) Microstructure showing type of failure

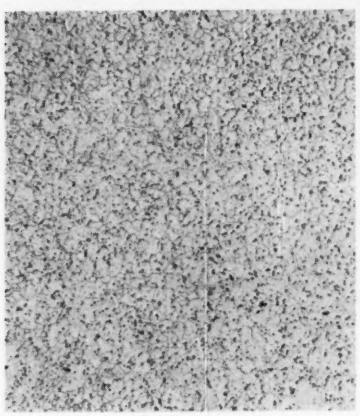

×100

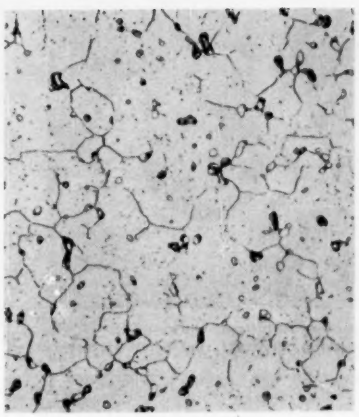

×1000

(c) Microstructure of failed tube; note appearance of sigma phase, 75 per cent nitric electrolytic etch

(d) Nitrogen pick-up at surface

Original	−0.035%
After exposure	−0.300%

(e) Properties before and after failure

	Test temp.	Tensile strength, psi	Yield (0.2%), psi	Elongation in 1.5″, %	Reduction of area, %	Brinell hardness	Charpy V notch, ft-lb	Maximum OD expansion, %
Original	Room							
Failed	Room	87,000	40,000	39.0	48.0	143	51, 61	39.8
Original	1500							
Failed	1500	26,000	16,500	67.0	66.0			

Fig. 16 Data on type 316 connecting pipe which failed after 6812 hr at 1500 F

Table 4 Characteristics of Cr, Mo, V before and after six-months' exposure at 1100 F

Chemical composition

C	Mn	P	S	Si	Cr	Mo	V
0.11	0.44	0.012	0.023	0.24	1.01	0.86	0.22

Heat-treatment	Grain size: Before exposure	Grain size: After exposure 1100 F	Carburized grain size
Annealed	7	7	9/8

Short-time tensile and impact properties

Test temperature		Tensile strength, psi	0.2% yield, psi	Elongation in 1.5", %	Reduction of area, %	Brinell hardness	Charpy V notch, ft-lb
Room	(1)	95,500	62,700	30		183	81
	(2)	78,500	56,700	30		163	
1100 F	(1)	48,900		31			62
	(2)	36,200		39			

(1) Unexposed, (2) 6 months at 1100 F.

Tube dimensions

Exposure temperature	Inlet end, in.: OD	Inlet end, in.: Wall	Outlet end, in.: OD	Outlet end, in.: Wall	Outlet end, in.: OD*	Max expansion, %
Unexposed	2.002/2.007					
1100 F	2.016/2.016					0.45

* OD at soot blower

Flattening characteristics

Exposure temperature	Height at which cracking occurred: Inlet end	Height at which cracking occurred: Outlet end	Calculated *H* value
Unexposed	No cracking	No cracking	
1100 F	No cracking	No cracking	

Scaling characteristics

Exposure temperature	Scale thickness: OD	Scale thickness: ID	Type attack
1100 F	0.007	0.007	General

Microstructures (etchant: Nital)

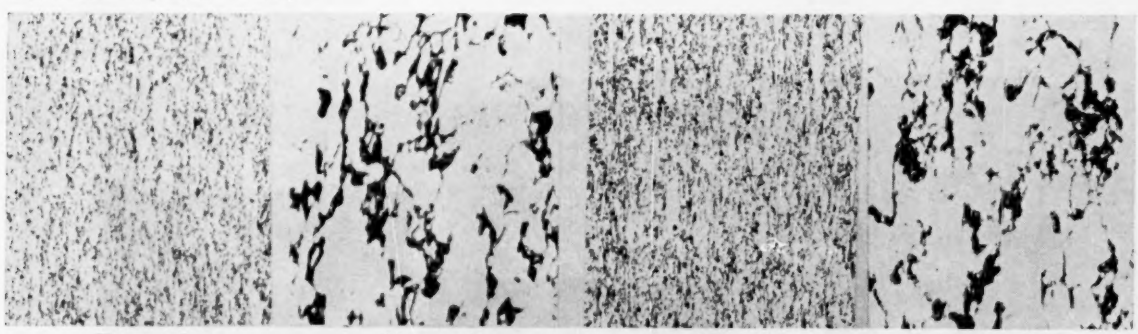

Unexposed ×100 D | Unexposed ×1000 D | 6 months, 1100 F ×100 D | 6 months, 1100 F ×1000 D

Table 5 Characteristics of 2 1/4-Cr 1-Mo before and after six-months' exposure at 1100 and 1200 F

Chemical composition

	C	Mn	S	P	Si	Cr	Mo
Before exposure	0.11	0.40	0.021	0.008	0.28	2.11	1.00
After exposure	0.10	0.39	0.018	0.009	0.29	2.12	1.05

Heat-treatment		Grain size after exposure			Decarburization			
		Original	1100 F	1200 F		Original	1100 F	1200 F
Annealed	Structural	7	6	6–7	ID	0	0.001	0
	McQuaid Ehn	6–7	6–7	6–7	OD	0	0.001	0.002

Short-time tensile, hardness, and impact properties

Test temperature		Tensile strength, psi	0.2% yield, psi	Elongation in 1.4", %	Reduction area, %	Brinell hardness	Charpy V notch, ft-lb
Room temperature	(1)	66,900	42,000	35.7	74.4	143	224, 195
	(2)[a]	65,200	33,300	35.8	82.7	145	181, 194
	(3)[a]	63,000	30,200	37.2	82.6	137	194, 193
1100 F	(1)	41,500	22,000	45.7	81	...	114, 98
	(2)	41,500	28,500	45.7	83.9	...	122, 130
1200 F	(1)	27,500	18,000	65.7	85.6	...	131, 130
	(3)	32,700	23,000	60	89.1	...	125, 112

(1) Unexposed, (2) six months at 1100 F, (3) six months at 1200 F.
[a] Standard 0.357-in. diam × 1.4-in. gage tensile specimens. Tensile specimens for the other tests were as shown in Fig. 1.

Tube dimensions

Exposure temperature	Outlet end, in. OD	Outlet end, in. Wall	Max % expansion
Unexposed	2.009/2.007	0.553/0.547	
1100 F	2.012/2.008	0.572/0.551	0.15
1200 F	2.023/2.028	0.570/0.558	0.95

Flattening characteristics

Exposure temperature	Height at which cracking occurred	Calculated H value
Unexposed	No cracking	1.68
1100 F	No cracking	1.69
1200 F	No cracking	1.70

Scaling characteristics

Exposure temperature	Scale thickness, in. OD	Scale thickness, in. ID	Type of attack
1100 F	0.005	0.005	General
1200 F	0.017	0.017	General

Microstructures (etchant: Picral)

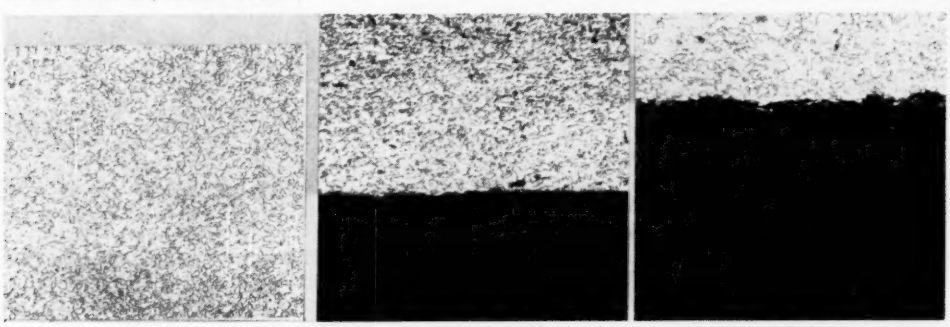

Unexposed ×100

6 months, 1100 F Inside surface ×100

6 months, 1200 F Inside surface ×100

Table 6 Characteristics of 3-Cr 1-Mo before and after six-months' exposure at 1100 and 1200

Chemical composition

C	Mn	P	S	Si	Cr	Mo
0.10	0.40	0.013	0.022	0.30	2.93	0.89

Heat-treatment	Grain Size			
		After exposure,		
Annealed	Before exposure	1100 F	1200 F	Carburized grain size
	8	9	9	9/8

Short-time tensile and impact properties

Test temperature	Tensile strength, psi	0.2% yield, psi	Elongation in 1.5″, %	Reduction of area, %	Brinell hardness	Charpy V notch, ft-lb
Room (1)	66,000	44,000	39		126	120 +
(2)	65,000	33,000	39		126	120 +
(3)	64,000	33,300	44		121	120 +
1100 F (1)	25,900		66			120 +
(2)	25,800		62			
1200 F (1)	18,300		83			120 +
(3)	17,400		78			

(1) Unexposed, (2) 6 months at 1100 F, (3) 6 months at 1200 F.

Tube dimensions

Exposure temperature	Inlet end, in.		Outlet end, in.			Max % expansion
	OD	Wall	OD	Wall	OD*	
Unexposed	2.001/2.006					
1100 F	2.016/2.020					0.7
1200 F	2.017/2.030					1.2

* OD at soot blower.

Flattening characteristics

Exposure temperature	Height at which cracking occurred		Calculated *H* value
	Inlet end	Outlet end	
Unexposed	No cracking	No cracking	
1100 F	No cracking	No cracking	
1200 F	No cracking	No cracking	

Scaling characteristics

Exposure temperature	Scale thickness, in.		Type attack
	OD	ID	
1100 F	0.008	0.008	General
1200 F	0.016	0.016	General

Microstructures (etchant: Nital)

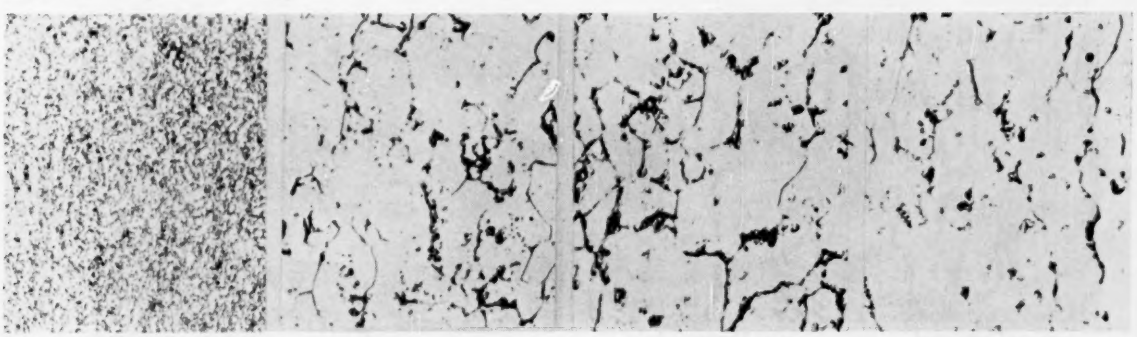

Unexposed ×100 D | Unexposed ×1000 D | 6 months, 1100 F ×1000 D | 6 months, 1200 F ×1000 D

Table 7 Characteristics of 5-Cr 1/2-Mo before and after six-months' exposure at 1100 and 1200 F

Chemical composition

C	Mn	P	S	Si	Cr	Mo
0.09	0.42	0.025	0.024	0.30	4.93	0.58

Heat-treatment	Grain size: Before exposure	After exposure: 1100 F	After exposure: 1200 F	Carburized grain size
Annealed	5/4	7/5	6/4	9/8

Short-time tensile and impact properties

Test temperature		Tensile strength, psi	0.2% yield, psi	Elongation in 1.5", %	Reduction of area, %	Brinell hardness	Charpy V notch, ft-lb
Room	(1)	68,500	35,500	37		140	120 +
	(2)	64,500	31,000	36		134	120 +
	(3)	61,000	29,500	38		126	120 +
1100 F	(1)	23,200		62			120 +
	(2)	23,900		65			
1200 F	(1)	15,700		75			120 +
	(3)	15,800		76			

(1) Unexposed, (2) 6 months at 1100 F, (3) 6 months at 1200 F.

Tube dimensions

Exposure temperature	Inlet end, in.: OD	Inlet end, in.: Wall	Outlet end, in.: OD	Outlet end, in.: Wall	OD*	Max % expansion
Unexposed	2.000/2.004					
1100 F	2.017/2.020					0.8
1200 F	2.028/2.032					1.4

* OD at soot blower.

Flattening characteristics

Exposure temperature	Height at which cracking occurred: Inlet end	Height at which cracking occurred: Outlet end	Calculated *H* Value
Unexposed	No cracking	No cracking	
1100 F	No cracking	No cracking	
1200 F	No cracking	No cracking	

Scaling characteristics

Exposure temperature	Scale thickness, in.: OD	Scale thickness, in.: ID	Type attack
1100 F	0.010	0.006	General
1200 F	0.015	0.017	General

Microstructures (etchant: Nital)

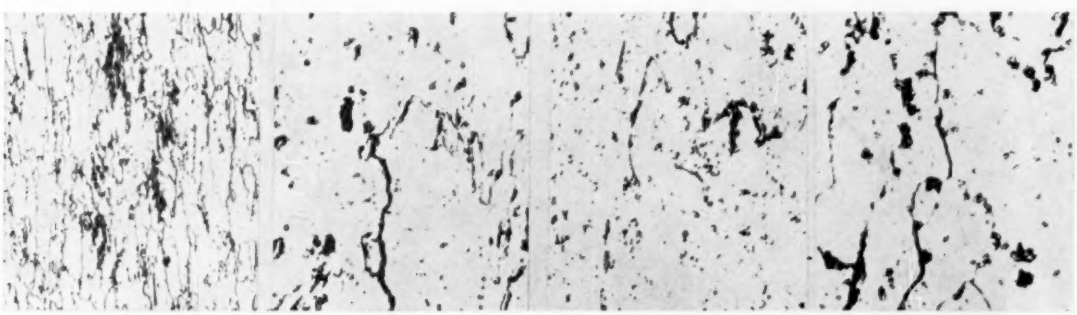

Unexposed ×100 D | Unexposed ×1000 D | 6 months, 1100 F ×1000 D | 6 months, 1200 F ×1000 D

Table 8 Characteristics of 5-Cr Mo + Ti before and after six-months' exposure at 1100 and 1200 F

Chemical composition

C	Mn	P	S	Si	Cr	Ni	Mo	Ti
0.06	0.46	0.019	0.015	0.25	5.02	0.20	0.51	0.57

Heat-treatment	Structural grain size after exposure			Carburized grain size
	Original	1100 F	1200 F	
Annealed	6/7 (8)	6/8	6/7 (8)	6/7

Short-time tensile, hardness, and impact properties

Test temperature	Tensile strength, psi	0.2% yield, psi	Elongation in 1.5", %	Reduction of area, %	Brinell hardness	Charpy V notch, ft-lb
Room (1)	59,750	25,750	45.7	75.2	115	138
(2)	58,300	26,000	42.5	80.9	116	136, 135, 121
(3)	57,900	27,500	42.8	81.0	114	118, 101, 111
1100 F (1)	25,500	14,350	60.0	76.0		99, 99, 95
(2)	25,650	15,000	63.0	87.9		143, 139, 143
1200 F (1)	17,950	11,450	74.0	93.0		89, 91, 93
(3)	18,300	12,500	75.1	91.0		145, 143, 214

(1) Unexposed, (2) after 6 months at 1100 F, (3) 6 months at 1200 F.

Tube dimensions

Exposure temperature	Inlet end, in.		Outlet end, in.			Max % expansion
	OD	Wall	OD	Wall	OD[a]	
Unexposed	1.998/2.002	0.497/0.503				
1100 F	2.008/2.014	0.549/0.560	2.004/2.008	0.550/0.564	2.005	0.6
1200 F	2.007/2.079	0.524/0.536	2.015/2.045	0.540/0.551	2.040	3.8

[a] OD at soot blower.

Flattening characteristics

Exposure temperature	Height at which cracking occurred, in.		Calculated *H* value, in.
	Inlet end	Outlet end	
Unexposed	1.14		1.64
1100 F	1.24	1.22	1.69
1200 F	1.13	1.14	1.73

Scaling characteristics

Exposure temperature	Scale thickness, in.		Type attack
	OD	ID	
1100 F	0.006	0.005	Intergranular, 1 grain
1200 F	0.015	0.018	Intergranular, 1½ grains

Microstructures (etchant: Nital)

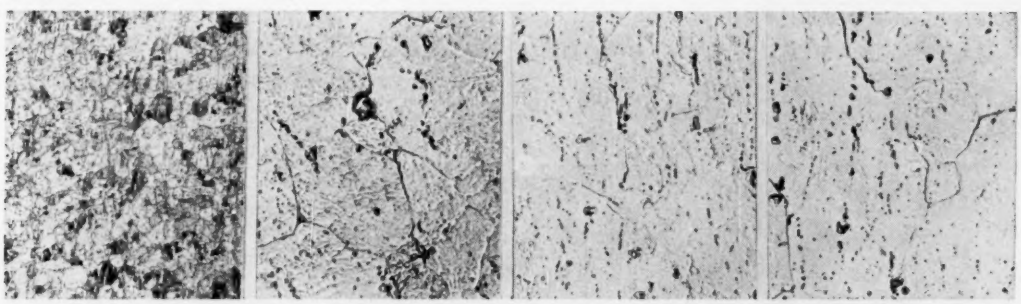

Unexposed ×100 D | Unexposed ×1000 D | 6 months, 1100 F ×1000 D | 6 months, 1200 F ×1000 D

Table 9 Characteristics of 5-Cr Mo + Si before and after six-months' exposure at 1100 and 1200 F

Chemical composition

C	Mn	P	S	Si	Cr	Ni	Mo
0.061	0.43	0.019	0.012	1.21	4.80	0.29	0.52

Heat-treatment	Structural grain size after exposure			Carburized grain size
Annealed	Original	1100 F	1200 F	
	6/7 (5)	8/7	8/7	6/7 (5)

Short-time tensile, hardness, and impact properties

Test temperature	Tensile strength, psi	0.2% yield, psi	Elongation in 1.5", %	Reduction of area, %	Brinell hardness	Charpy V notch, ft-lb
Room (1)	71,750	36,500	40.5	78.0	143	156
(2)	71,000	44,600	36.8	73.1	149	17, 12, 32
(3)	69,000	43,400	36.7	74.5	137	20, 17, 33
1100 F (1)	30,300	18,850	68.5	92.0		122, 124, 122
(2)	29,700	18,600	70.3	88.7		174, 183, 179
1200 F (1)	19,900	14,000	86.0	95.0		117, 116, 114
(3)	19,700	13,750	73.3	92.7		158.158, 160

(1) Unexposed, (2) after 6 months at 1100 F, (3) 6 months at 1200 F.

Tube dimensions

Exposure temperature	Inlet end, in.		Outlet end, in.			Max % expansion
	OD	Wall	OD	Wall	OD[a]	
Unexposed	2.001/2.007	0.501/0.510				
1100 F	2.010/2.020	0.555/0.567	2.008/2.013	0.554/0.568	2.010	0.6
1200 F	2.037/2.042	0.558/0.567	2.028/2.030	0.563/0.567	2.028	1.7

[a] OD at soot blower.

Flattening characteristics

Exposure temperature	Height at which cracking occurred, in.		Calculated *H* value, in.
	Inlet end	Outlet end	
Unexposed	No cracking		1.64
1100 F	1.28	1.62	1.67
1200 F	1.30	1.20	1.71

Scaling characteristics

Exposure temperature	Scale thickness, in.		Type attack
	OD	ID	
1100 F	0.005	0.007	Intergranular, 1 grain
1200 F	0.014	0.015	Intergranular, 2 grains

Microstructures (etchant: Nital)

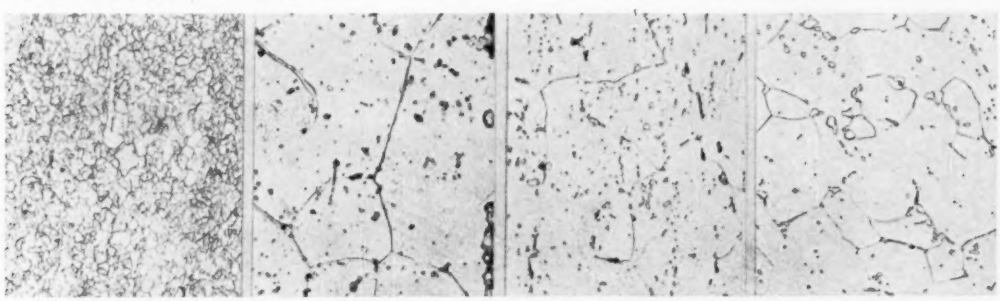

Unexposed ×100 D | Unexposed ×1000 D | 6 months, 1100 F ×1000 D | 6 months, 1200 F ×1000 D

Table 10 Characteristics of 9-Cr 1-Mo before and after six-months' exposure at 1100 and 1200 F

Chemical composition

	C	Mn	S	P	Si	Cr	Mo
Before exposure	0.11	0.42	0.021	0.009	0.35	8.63	0.90
After exposure	0.10	0.42	0.19	0.009	0.34	0.58	0.91

		Grain size after exposure			Decarburization			
Heat-treatment		Original	1100 F	1200 F		Original	1100 F	1200 F
Annealed	Structure	6–7	6–7	6–7	ID	0.002	0	0
	McQuaid Ehn		Not run		OD	0	0	0

Short-time tensile, hardness, and impact properties

Test temperature		Tensile strength, psi	0.2% yield, psi	Elongation in 1.4", %	Reduction of area, %	Brinell hardness	Charpy V notch, ft-lb
Room temperature	(1)	71,500	38,200	35.7	75	148	130, 165
	(2)[a]	72,100	37,600	31.4	82.4	155	104, 116
	(3)[a]	84,100	59,900	21.4	81.4	148	123, 127
1100 F	(1)	41,500	22,000	45.7	81	...	166, 170
	(2)	44,000	22,500	37.1	85	...	149, 146
1200 F	(1)	27,500	18,000	65.7	85.6	...	140, 142
	(3)	39,000	30,000	32.9	89.7	...	139, 129

(1) Unexposed, (2) six months at 1100 F, (3) six months at 1200 F.
[a] Standard 0.357 × 14-in. gage tensile specimens. The others were as shown in Fig. 1.

Tube dimensions

	Outlet end, in.		
Exposure temperature	OD	Wall	Max % expansion
Unexposed	2.002/2.006	0.553/0.559	...
1100 F	2.011/2.018	0.557/0.561	0.60
1200 F	2.016/2.020	0.556/0.564	0.70

Flattening characteristics

	Height at which cracking occurred	Calculated *H* value, in.
Unexposed temperature	No cracking	1.68
1100 F	No cracking	1.68
1200 F	No cracking	1.69

Scaling characteristics

	Scale thickness, in.		
Exposure temperature	ID	OD	Type of attack
1100 F	0.004	0.008	General
1200 F	0.010	0.004	General

Microstructures

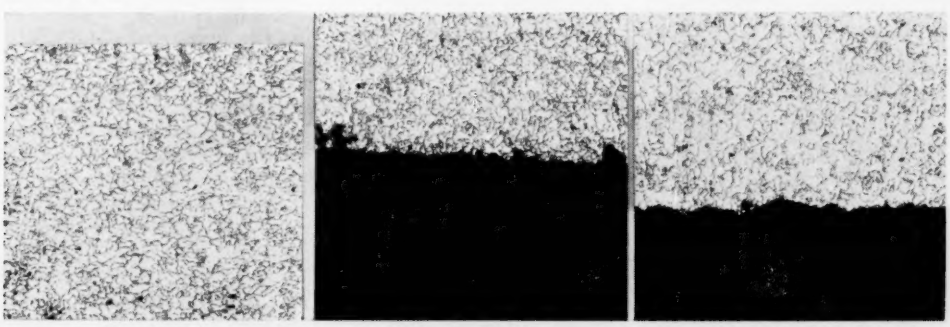

Unexposed
Etchant: HCl and Picral
×100

6 months, 1100 F
Inside surface
Etchant: Picral
×100

6 months, 1200 F
Inside surface
Etchant: Picral
×100

Table 11 Characteristics of TP 304 before and after six-months' exposure at 1200, 1350, and 1500 F

Chemical composition

C	Mn	P	S	Si	Cr	Ni
0.072	1.72	0.012	0.026	0.38	18.48	10.23

Heat-treatment	Structural grain size after exposure			
	Original	1200 F	1350 F	1500 F
Solution quenched, 2050 F	1/2(3, 5)	2/4(1, 5)	1/3(4)	3/5(2)

Short-time tensile, hardness, and impact properties

Test temperature		Tensile strength, psi	0.2% yield psi	Elongation in 1.5", %	Reduction of area, %	Brinell hardness	Charpy V notch, ft-lb
Room	(1)	83,500	34,750	65.0	76.0	127	213, 216, 207
	(2)	95,000	40,700	31.0	58.0	163	107, 119, 115
	(3)	91,200	36,300	33.0	62.0	156	120, 120, 122
	(4)	88,300	34,800	31.0	60.0	145	97, 94, 100
1200 F	(1)	46,000	17,000	40.0	58.0		162, 160, 169
	(2)	49,000	21,100	31.0	61.0		181, 181, 177
1350 F	(1)[a]	43,000	16,250	37.0	50.0		167, 164, 168
	(3)	37,900	16,000	42.0	62.0		178, 169, 181
1500 F	(1)	27,000	14,350	41.0	44.0		159, 150, 158
	(4)	41,000	15,800	39.0	65.0		162, 147, 147

(1) Unexposed, (2) after 6 months at 1200 F, (3) at 1350 F, (4) at 1500 F.
[a] 1300 F rather than 1350 F.

Tube dimensions

Exposure temperature	Inlet end, in.		Outlet end, in.		Max % expansion
	OD	Wall	OD	Wall	OD
Unexposed	1.977/1.978	0.526/0.560			
1200 F	1.996/1.998	0.553/0.558			1.00
1350 F	1.996/1.997	0.548/0.557			1.00
1500 F	1.997/2.003	0.533/0.549			1.26

Flattening results

Exposure temperature	Height at which cracking occurred		Calculated *H* value, in.
	Inlet end	Outlet end	
Unexposed	Satisfactory		1.62
1200 F	Satisfactory		1.62
1350 F	Satisfactory		1.62
1500 F	Satisfactory		1.62

Scaling characteristics

Exposure temperature	Scale thickness		Type attack
	OD	ID	
1200 F	Not reported		Assumed very slight
1350 F	Not reported		Assumed very slight
1500 F	Not reported		Assumed very slight

Microstructures (×1000 D)

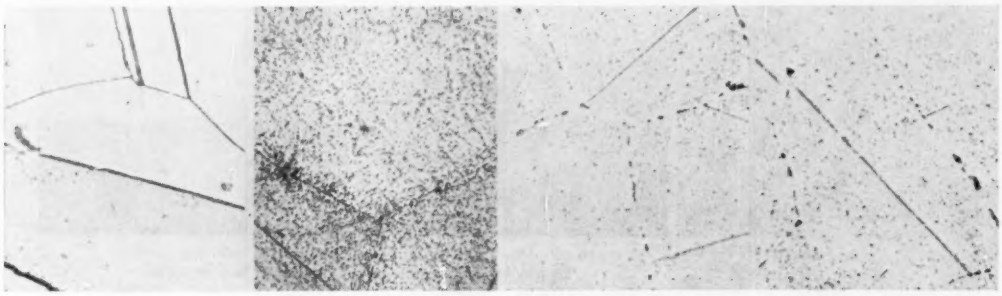

Unexposed
Etchant: Ferric chloride

6 months, 1200 F

6 months, 1350 F
Etchant: Electrolytic 10 per cent chromic acid

6 months, 1500 F

Table 12 Characteristics of TP-316 before and after six-months' exposure at 1200, 1350, and 1500 F

Chemical composition

C	Mn	P	S	Si	Ni	Cr	Mo
0.06	1.84	0.026	0.014	0.35	13.20	16.77	1.96

Heat-treatment	Grain size: Before exposure	After exposure: 1200 F	After exposure: 1350 F	After exposure: 1500 F
Solution annealed	4/3	1/5	1/5	1/5

Short-time tensile and impact properties

Test temperature		Tensile strength, psi	0.2% yield, psi	Elongation in 1.5", %	Reduction of area, %	Brinell hardness	Charpy V notch, ft-lb
Room	(1)	80,000	34,700	63		126	
	(2)	87,500	37,700	46		149	97
	(3)	91,000	38,000	41		152	49
	(4)	85,000	33,300	48		140	66
1200 F	(1)	44,200		42			120 +
	(2)	46,300		50			120 +
1350 F	(1)	30,300		72			120 +
	(3)	33,800		57			120 +
1500 F	(1)	17,500		57			120 +
	(4)	21,000		57			120 +

(1) Unexposed, (2) 6 months at 1200 F, (3) 6 months at 1350 F, (4) 6 months at 1500 F.

Tube dimensions

Exposure temperature	Inlet end, in.: OD	Inlet end, in.: Wall	Outlet end, in.: OD	Outlet end, in.: Wall	Outlet end, in.: OD*	Max % expansion
Unexposed	2.003/2.007					
1200 F	2.005/2.007					0.0
1350 F	2.005/2.009					0.1
1500 F	2.003/2.007					0.0

* OD at soot blower.

Flattening characteristics

Exposure temperature	Height at which cracking occurred: Inlet end	Height at which cracking occurred: Outlet end	Calculated *H* value
Unexposed	No cracking	No cracking	
1200 F	No cracking	No cracking	
1350 F	No cracking	No cracking	
1500 F	No cracking	No cracking	

Scaling characteristics

Exposure temperature	Scale Thickness: OD	Scale Thickness: ID	Type attack
1200 F	Very slight, not reported		
1350 F	Very slight, not reported		
1500 F	Very slight, not reported		

Microstructures (etchant: Oxalic, electrolytically, ×1000 D)

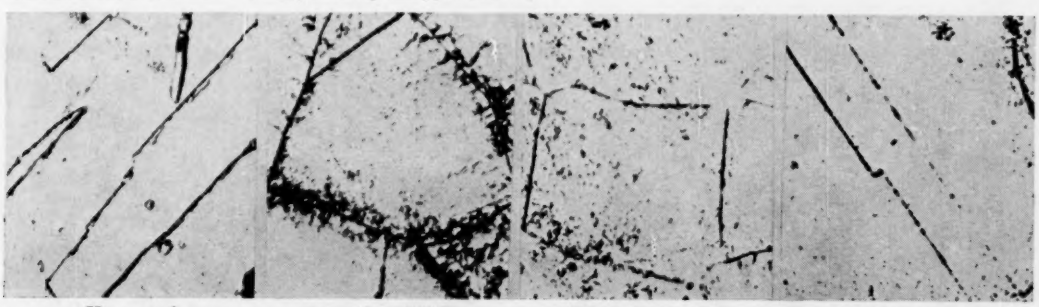

Unexposed | 6 months, 1200 F | 6 months, 1350 F | 6 months, 1500 F

Table 13 Characteristics of TP-321 before and after six-months' exposure at 1200, 1350, and 1500 F

Chemical composition

	C	Mn	S	P	Si	Cr	Ni	Ti
Before exposure	0.045	1.71	0.014	0.012	0.47	17.79	12.23	0.45
After exposure	0.044	1.76	0.011	0.010	0.46	17.80	12.12	0.46

		Grain size after exposure			
Heat-treatment		Original	1200 F	1350 F	1500 F
Solution annealed	Structural	5	5	5–6	5–6

Short-time tensile, hardness, and impact properties

Test temperature		Tensile strength, psi	0.2% yield, psi	Elongation in 1.4", %	Reduction of area, %	Brinell hardness	Charpy V notch, ft-lb
Room temperature	(1)	75,100	32,400	29.6	70.4	126	230, 230
	(2)[a]	81,500	39,900	44.3	80.4	145	130, 132
	(3)[a]	79,500	33,600	45.7	79.4	143	116, 115
	(4)[a]	75,900	29,100	52.9	80.8	137	150, 151
1200 F	(1)	62,000	26,200	37.1	49		177, 179
	(2)	57,000	34,000	28.6	63.4		155, 151
1350 F	(1)	37,500	18,000	31.4	15.4		153, 145
	(3)	45,300	24,100	32.9	42.4		135, 137
1500 F	(1)	28,000	17,000	44.3	32.5		147, 152
	(4)	33,500	22,500	41.4	42		149, 150

1 Unexposed, (2) six months at 1200 F, (3) six months at 1350 F, (4) six months at 1500 F.
[a] Standard 0.357-in. diam × 1.4-in. gage tensile specimens. The others were as shown in Fig. 1.

Tube dimensions

Exposure temperature	Outlet end, in. OD	Outlet end, in. ID	Max % expansion
Unexposed	2.009/2.012	0.517/0.533	...
1200 F	2.008/2.013	0.527/0.541	0.04
1350 F	2.008/2.014	0.517/0.533	0.1
1500 F	2.007/2.012	0.511/0.537	0

Flattening characteristics

Exposure temperature	Height at which cracking occurred	Calculated H value, in.
Unexposed	No cracking	1.63
1200 F	No cracking	1.63
1350 F	No cracking	1.63
1500 F	No cracking	1.63

Scaling characteristics

Exposure temperature	Scale thickness, in. OD	Scale thickness, in. ID	Type of attack
1200 F	Under 0.002		General
1350 F	Under 0.002		General
1500 F	Under 0.002		General

Microstructures (etchant: Aqua regia, ×100)

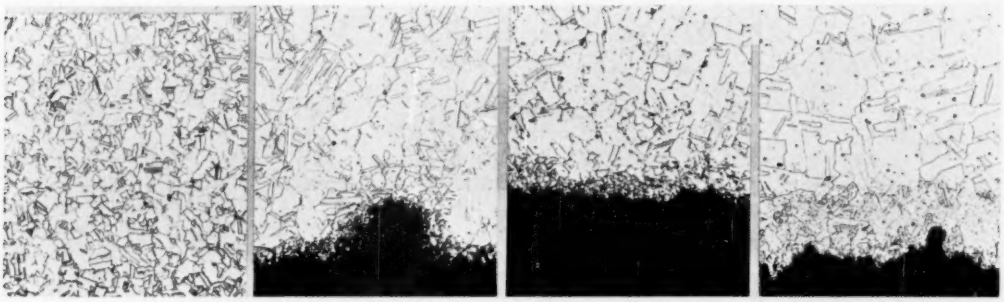

Unexposed

6 months, 1200 F
Inside surface

6 months, 1350 F
Inside surface

6 months, 1500 F
Inside surface

Table 14 Characteristics of TP-347 before and after six-months' exposure at 1200, 1350, and after 2200 hr at 1500 F

Chemical composition

C	Mn	P	S	Si	Cu	Ni	Cr	Cb	Ta
0.06	1.74	0.022	0.010	0.65	0.17	10.90	17.93	0.56	0.05

	Grain size			
	Before exposure	After exposure		
Heat-treatment		1200 F	1350 F	1500 F
Solution annealed	9/2	9/2	9/2	8/3

Short-time tensile and impact properties

Test temperature		Tensile strength, psi	0.2% yield, psi	Elongation in 1.5", %	Reduction of area, %	Brinnell hardness	Charpy V notch, ft-lb
Room	(1)					137	120 +
	(2)	89,500	41,000	42		156	67
	(3)	89,000	36,100	42		146	50
	(4)	83,000	34,300	50		140	64
1200 F	(1)	49,450		33	40.8		120 +
	(2)	44,500		35			120 +
1350 F	(1)	35,200		32	37.0		120 +
	(3)	28,500		66			120 +
1500 F	(1)	21,940		39	50.6		120 +
	(4)	16,000		60			120 +

(1) Unexposed, (2) 6 months at 1200 F, (3) 6 months at 1350 F, (4) 2200 hr at 1500 F.

Tube dimensions

Exposure temperature	Inlet end, in.		Outlet end, in.			Max % expansion
	OD	Wall	OD	Wall	OD*	
Unexposed	2.004/2.007	0.545/0.571				
1200 F	2.005/2.007					0.0
1350 F	2.005/2.007					0.0
1500 F	2.045/2.147		2.023/2.027			7.0

* OD at soot blower.

Flattening characteristics

Exposure temperature	Height at which cracking occurred, in.		Calculated *H* value, in.
	Inlet end	Outlet end	
Unexposed	No cracking	No cracking	1.65
1200 F	No cracking	No cracking	
1350 F	No cracking	No cracking	
1500 F	1.75	1.75	

Scaling characteristics

Exposure temperature	Scale thickness		Type attack
	OD	ID	
1200 F	Very slight,	not reported	
1350 F	Very slight,	not reported	
1500 F	Very slight,	not reported	

Microstructures (etchant: Nitric, electrolytically, ×1000 D)

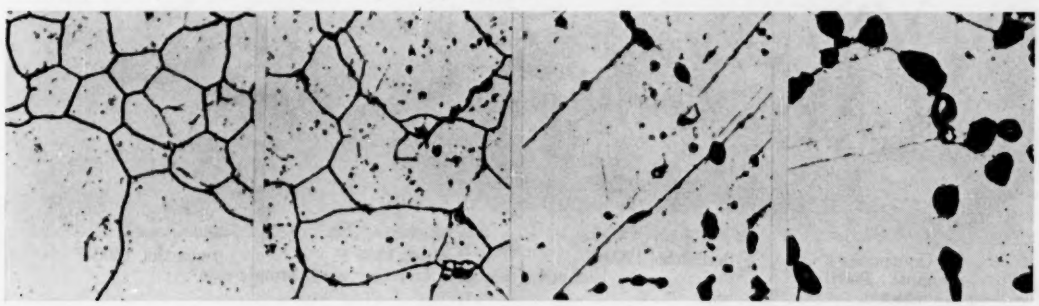

Unexposed | 6 months, 1200 F | 6 months, 1350 F | 2200 hr, 1500 F

Table 15 Characteristics of TP 310 before and after six-months' exposure at 1200, 1350, and 1500 F

Chemical composition

C	Mn	P	S	Si	Cr	Ni
0.072	1.55	0.007	0.018	0.25	24.56	21.42

Heat-treatment	Structural grain size after exposure			
	Original	1200 F	1350 F	1500 F
Solution quenched, 2075 F	3(2, 4)	3/6	4/6	4/6(3)

Short-time tensile, hardness, and impact properties

Test temperature		Tensile strength, psi	0.2% yield, psi	Elongation in 1.5", %	Reduction of area, %	Brinell hardness	Charpy V notch, ft-lb
Room	(1)	84,500	32,750	50.0	74.0	128	206, 204, 206
	(2)	94,000	45,800	35.0	51.0	163	45, 43, 58
	(3)	92,000	42,400	30.0	36.0	170	18, 17, 17
	(4)	70,300	37,500	13.0	15.0	156	24, 22, 21
1200 F	(1)	53,500	15,250	41.0	50.0		167, 176, 182
	(2)	56,000	26,150	30.0	52.0		112, 110, 127
1350 F	(1)[a]	49,000	15,800	35.0	44.0		180, 175, 178
	(3)	45,500	20,100	29.0	31.0		45, 38, 43
1500 F	(1)	34,500	14,000	41.0	41.0		162, 170, 165
	(4)	45,250	19,800	26.0	28.0		32, 26, 38

(1) Unexposed, (2) after 6 months at 1200 F, (3) at 1350 F, (4) after 3000 hr at 1500 F.
[a] 1300 F rather than 1350 F.

Tube dimensions

Exposure temperature	Inlet end, in.		Outlet end, in.			Max % expansion
	OD	Wall	OD	Wall	OD*	
Unexposed	1.993/1.998	0.527/0.547				...
1200 F	1.992/1.990	0.539/0.549				...
1350 F	1.998/2.000	0.522/0.540				0.20
1500 F	2.046/2.054	0.519/0.538				2.76

* OD at soot blower.

Flattening results

Exposure temperature	Height at which cracking occurred, in.		Calculated *H* value, in.
	Inlet end	Outlet end	
Unexposed	Satisfactory		1.62
1200 F	Satisfactory		1.62
1350 F	Fractured at 1.5		1.63
1500 F	Fractured at 1.75		1.65

Scaling characteristics

Exposure temperature	Scale thickness		Type attack
	OD	ID	
1200 F	Not reported		Assumed very slight
1350 F	Not reported		Assumed very slight
1500 F	Not reported		Assumed very slight

Microstructures (×1000 D)

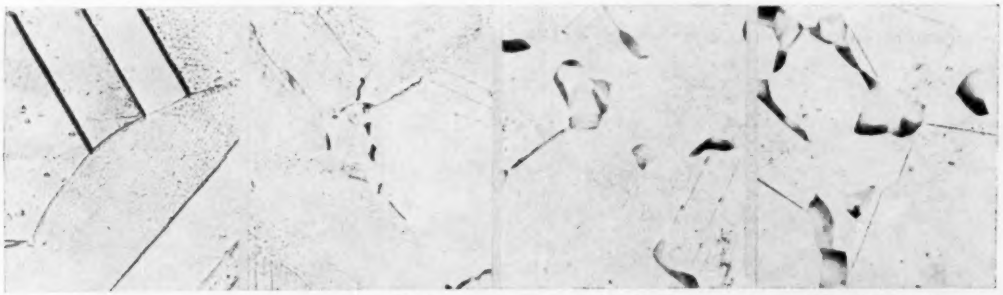

Unexposed
Etchant: Ferritic chloride

6 months, 1200 F

6 months, 1350 F
Etchant: Electrolytic 10 per cent chromic acid

6 months, 1500 F

Table 16 Characteristics of 16-25-6 before and after six-months' exposure at 1200, 1350, and 1500 F

Chemical composition

C	Mn	P	S	Si	Cr	Ni	Mo	N_2
0.053	1.73	0.020	0.010	0.93	15.70	25.09	5.34	0.18

Heat-treatment	Structural grain size after exposure			
Solution quenched	Original	1200 F	1350 F	1500 F
	5/4 (6, 3)	5/6 (4)	4/3 (2)	5/6 (4)

Short-time tensile, hardness, and impact properties

Test temperature		Tensile strength, psi	0.2% yield, psi	Elongation in 1.5″, %	Reduction of area, %	Brinell hardness	Charpy V notch, ft-lb
Room	(1)	109,400	49,000	52	67	166	167
	(2)	117,700	55,000	18	24	229	15, 15, 15
	(3)	118,300	55,000	23	28	229	14, 16, 14
	(4)	107,000	43,700	26	30	197	19, 17, 19
1200 F	(1)	76,800	29,750	46	48		131, 140, 117
	(2)	71,800	42,800	35	46		28, 27, 26
1350 F	(1)	55,900	28,250	25	29		104, 114, 125
	(3)	51,800	34,300	37	44		34, 37, 35
1500 F	(1)	44,800	27,500	43	45		103, 80, 88
	(4)	36,300	23,000	68	64		51, 50, 52

(1) Unexposed, (2) 6 months at 1200 F, (3) 6 months at 1350 F, (4) 6 months at 1500 F.

Tube dimensions

Exposure temperature	Inlet end, in.		Outlet end, in.			Max % expansion
	OD	Wall	OD	Wall	OD[a]	
Unexposed	1.987/8	0.502/7				
1200 F	1.995/6	0.505/8	1.995/6	0.503/8	1.995	0.4
1350 F	1.995/7	0.504/7	1.995/8	0.505/6	1.995	0.5
1500 F	2.000/2	0.503/9	1.997/8	0.503/5	1.998	0.7

[a] OD at soot blower.

Flattening characteristics

Exposure temperature	Height at which cracking occurred, in.		Calculated *H* value, in.
	Inlet end	Outlet end	
Unexposed	1.34		1.60
1200 F	1.84	1.88	1.60
1350 F	1.82	1.81	1.62
1500 F	Fractured	1.83	1.62

Scaling characteristics

Exposure temperature	Scale thickness, in.		Type attack
	OD	ID	
1200 F	0.0004	0.0015	General
1350 F	0.0005	0.0010	General
1500 F	0.0010	0.0016	General

Microstructures (etchant: Glyceregia, ×1000 D)

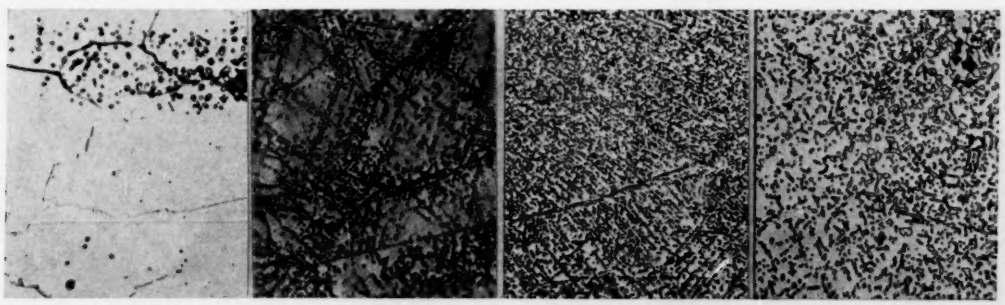

Unexposed | 6 months, 1200 F | 6 months, 1350 F | 6 months 1500 F

Table 17 Characteristics of 17-14 Cu-Mo before and after six-months' exposure at 1200, 1350, and 1500 F

Chemical composition

C	Mn	P	S	Si	Cr	Ni	Mo	Cu	Cb	Ti
0.128	0.76	0.028	0.014	0.25	15.93	14.54	2.60	2.81	0.53	0.19

Heat-treatment	Structural grain size after exposure			
Solution quenched	Original	1200 F	1350 F	1500 F
	7/8	8	8(7)	8(6)

Short-time tensile, hardness, and impact properties

Test temperature		Tensile strength, psi	0.2% yield, psi	Elongation in 1.5", %	Reduction of area, %	Brinell hardness	Charpy V notch, ft-lb
Room	(1)	89,250	45,500	46.8	67.7	143	132
	(2)	100,500	49,000	30.0	43.0	197	47, 47, 47
	(3)	94,800	42,500	36.0	51.0	179	46, 45, 43
	(4)	86,800	38,000	38.0	48.5	156	49, 48, 55
1200 F	(1)	57,900	30,900	38.0	51.0	...	120, 112, 116
	(2)	57,000	35,900	20.0	30.3	...	53, 58, 63
1350 F	(1)	39,000	26,800	52.0	53.5	...	95, 102, 89
	(3)	40,800	26,250	37.0	39.5	...	64, 62, 64
1500 F	(1)	27,600	22,300	53.0	58.0	...	81, 80, 72
	(4)	26,000	18,500	17.5	20.0	...	54, 52, 55

(1) Unexposed, (2) 6 months at 1200 F, (3) 6 months at 1350 F, (4) 6 months at 1500 F.

Tube dimensions

Exposure temperature	Inlet end, in.		Outlet end, in.			Max % expansion
	OD	Wall	OD	Wall	OD*	
Unexposed	2.003/2.005	0.502/0.507				
1200 F	2.003/2.005	0.522/0.552	2.002/2.004	0.532/0.542	2.004	0.0
1350 F	2.008/2.011	0.529/0.542	2.005/2.009	0.520/0.552	2.007	0.3
1500 F	2.013/2.015	0.529/0.536	2.003/2.012	0.525/0.540	2.012	0.5

* OD at soot blower.

Flattening characteristics

Exposure temperature	Height at which cracking occurred, in.		Calculated *H* value, in.
	Inlet end	Outlet end	
Unexposed	No cracking		1.64
1200 F	1.26	1.30	1.61
1350 F	No cracking	No cracking	1.64
1500 F	No cracking	1.43	1.66

Scaling characteristics

Exposure temperature	Scale thickness, in.		Type attack
	OD	ID	
1200 F	0.0002	0.0020	General
1350 F	0.0003	0.0020	General, pits 0.002 in. deep
1500 F	0.0003	0.0020	General, pits 0.002 in. deep

Microstructures (etchant: Glyceregia, ×1000 D)

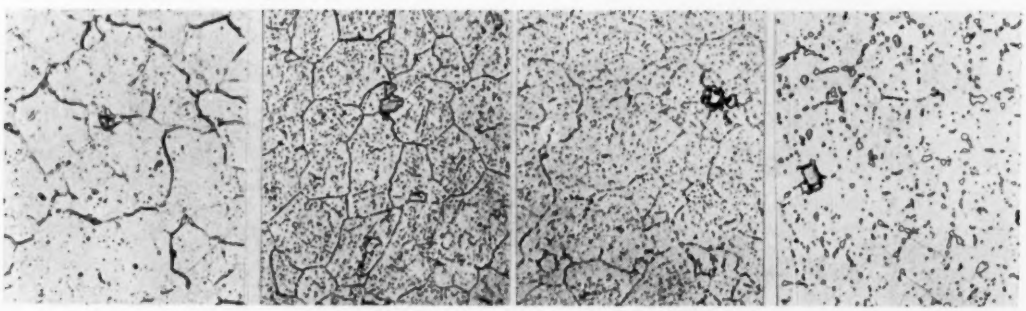

Unexposed | 6 months, 1200 F | 6 months, 1350 F | 6 months, 1500 F

Table 18 Characteristics of Croloy 15-15N before and after six-months' exposure at 1200, 1350, and 1500 F

Chemical composition

	C	Mn	S	P	Si	Cr	Ni	Mo	Cb-Ta	W
Before exposure	0.12	1.27	0.013	0.010	0.89	14.98	15.42	1.45	1.22	1.24
After exposure	0.12	1.26	0.016	0.010	0.87	15.14	15.40	1.45	1.12	1.27

		Grain size after exposure			
Heat-treatment	Structural	Original	1200 F	1300 F	1500 F
Solution annealed		6	6–7	6–7	5–6

Short-time tensile, hardness, and impact properties

Test temperature		Tensile strength, psi	0.2% yield, psi	Elongation in 1.4", %	Reduction of area, %	Brinell hardness	Charpy V notch, ft-lb
Room temperature	(1)	86,700	45,300	41.0	59	148	137, 134
	(2)[a]	93,400	40,100	37.2	75.8	161	65, 63
	(3)[a]	91,900	40,800	34.3	74.6	175	43, 41
	(4)[a]	90,600	35,800	37.2	74.8	155	48, 51
1200 F	(1)	50,500	18,500	34.2	49.5		122, 127
	(2)	64,000	36,500	34.3	27.9		66, 61
1350 F	(1)	47,000	25,000	35.7	35.1		113, 108
	(3)	50,000	30,000	41.4	65.1		46, 47
1500 F	(1)	36,500	23,500	61.4	55.1		120, 113
	(4)	37,200	26,200	71.4	60.7		70, 74

(1) Unexposed, (2) 6 months at 1200 F, (3) 6 months at 1350 F, (4) 6 months at 1500 F.
[a] Standard 0.357 in. × 1.4-in. gage tensile specimens. All others as shown in Fig. 1.

Tube dimensions

Exposure temperature	Outlet end, in. OD	Outlet end, in. ID	Max % expansion
Unexposed	2.000/2.007	0.525/0.548	
1200 F	2.000/2.003	0.531/0.553	None (0.19% reduction in size)
1350 F	2.000/2.002	0.521/0.556	None (0.25% reduction in size)
1500 F	1.983/1.985	0.513/0.552	None (1.1% reduction in size)

Flattening characteristics

Exposure temperature	Height at which cracking occurred, in.	Calculated *H* value, in.
Unexposed	No cracking	1.63
1200 F	No cracking	1.64
1350 F	1.50	1.53
1500 F	No cracking	1.52

Scaling characteristics

Exposure temperature	Scale thickness, in. OD	Scale thickness, in. ID	Type attack
1200 F	Under 0.002		
1350 F	Under 0.002	0.005	
1500 F	Under 0.002	0.006	General with pronounced exfoliation

Microstructures (etchant: Aqua regia, ×100)

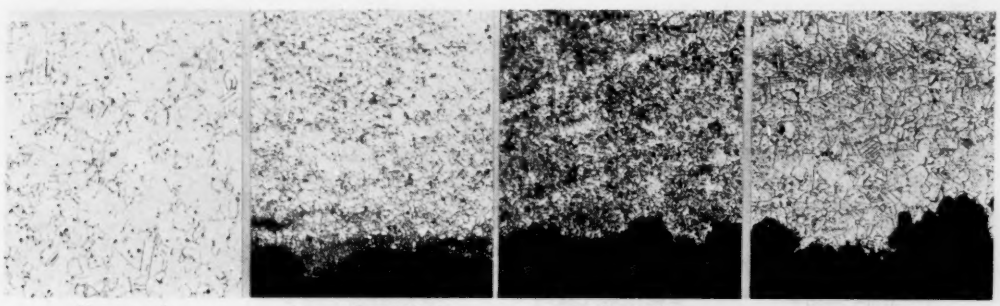

Unexposed

6 months, 1200 F
Inside surface

6 months, 1350 F
Inside surface

6 months, 1500 F
Inside surface

Table 19 Characteristics of Inconel alloy before and after six-months' exposure at 1200, 1350, and 1550 F

Chemical composition

C	Mn	P	S	Si	Cr	Ni
0.04	0.24	...	0.007	0.26	15.70	75.57

Heat-treatment	Structural grain size after exposure			
Solution quenched, 2050 F	Original	1200 F	1350 F	1500 F
	1/4 (6)	1/3 (4, 5)	1/3 (4, 5)	1/4 (5)

Short-time tensile, hardness, and impact properties

Test temperature		Tensile strength, psi	0.2% yield, psi	Elongation in 1.5", %	Reduction of area, %	Brinell hardness	Charpy V notch, ft-lb
Room	(1)	84,500	24,500	56.0	66.0	128	207, 202, 218
	(2)	89,400	28,600	48.0	65.0	132	144, 146, 141
	(3)	88,700	27,100	49.0	64.0	126	184, 217, 200
	(4)	86,000	26,200	50.0	68.0	121	184, 192, 187
1200 F	(1)	64,900	15,800	56.0	63.0		174, 171, 170
	(2)	59,500	17,350	44.0	56.0		181, 165, 162
1350 F	(1)[a]	61,000	15,500	54.0	58.0		168, 184, 172
	(3)	61,350	15,400	42.0	47.0		202, 175, 219
1500 F	(1)	42,750	14,500	67.0	74.0		167, 174, 170
	(4)	51,500	14,500	45.0	42.0		167, 170, 162

(1) Unexposed, (2) after 6 months at 1200 F, (3) at 1350 F, (4) at 1500 F.
[a] 1300 F rather than 1350 F.

Tube dimensions

Exposure temperature	Inlet end, in.		Outlet end, in.			Max % expansion
	OD	Wall	OD	Wall	OD*	
Unexposed	2.004/2.006	0.498/0.507				...
1200 F	2.002/2.004	0.488/0.517				...
1350 F	2.000/2.002	0.489/0.523				...
1500 F	2.033/2.033	0.486/0.503				1.40

* OD at soot blower.

Flattening results

Exposure temperature	Height at which cracking occurred, in.		Calculated *H* value, in.
	Inlet end	Outlet end	
Unexposed	Satisfactory		1.60
1200 F	Satisfactory		1.60
1350 F	Satisfactory		1.60
1500 F	Satisfactory		1.62

Scaling characteristics

Exposure temperature	Scale thickness, in.		Type attack
	OD	ID	
1200 F	Not reported		Assumed very slight
1350 F	Not reported		Assumed very slight
1500 F	Not reported		Assumed very slight

Microstructures (×1000 D)

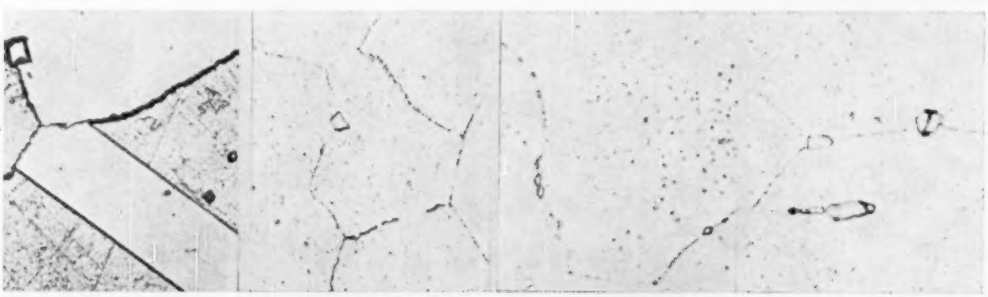

Unexposed
Etchant: Ferric chloride

6 months, 1200 F

6 months, 1350 F
Etchant: Glyceregia

6 months, 1500 F

Table 20 Characteristics of Incoloy alloy before and after six-months' exposure at 1200, 1350, and 1500 F

Chemical composition

C	Mn	P	S	Si	Cr	Ni
0.05	0.79	...	0.007	0.55	20.69	34.66

Heat-treatment	Structural grain size after exposure			
	Original	1200 F	1350 F	1500 F
Solution quenched, 2050 F	Duplexed 3/8	2/5, 6/8	2/5 (6, 7)	2/6

Short-time tensile, hardness, and impact properties

Test temperature		Tensile strength, psi	0.2% yield, psi	Elongation in 1.5″, %	Reduction of area, %	Brinell hardness	Charpy V notch, ft-lb
Room	(1)	82,500	28,500	51.0	68.0	112	206, 202, 214
	(2)	111,350	57,000	28.0	36.0	190	38, 32, 32
	(3)	96,400	40,000	35.0	45.0	154	49, 50, 59
	(4)	84,900	34,300	45.0	66.0	130	129, 112, 116
1200 F	(1)	60,500	16,500	49.0	69.0		183, 187, 174
	(2)	83,750	50,800	20.0	34.0		57, 56, 61
1350 F	(1)[a]	54,900	16,500	48.0	66.0		169, 181, 178
	(3)	68,750	28,000	30.0	48.0		91, 179, 98
1500 F	(1)	36,500	15,500	57.0	68.0		180, 173, 174
	(4)	49,200	18,900	44.0	48.0		110, 176, 158

(1) Unexposed, (2) after 6 months at 1200 F, (3) at 1350 F, (4) at 1500 F.
[a] 1300 F rather than 1350 F.

Tube dimensions

Exposure temperature	Inlet end, in.		Outlet end, in.			Max % expansion
	OD	Wall	OD	Wall	OD*	
Unexposed	0.001/2.012	0.493/0.503				...
1200 F	2.002/2.003	0.499/0.507				...
1350 F	2.003/2.004	0.495/0.510				...
1500 F	2.056/2.061	0.465/0.496				3.00

* OD at soot blower.

Flattening results

Exposure temperature	Height at which cracking occurred, in.		Calculated *H* value, in.
	Inlet end	Outlet end	
Unexposed	Satisfactory		1.60
1200 F	ID cracking at 1.81		1.60
1350 F	Satisfactory		1.60
1500 F	Satisfactory		1.62

Scaling characteristics

Exposure temperature	Scale thickness, in.		Type attack
	OD	ID	
1200 F	Not reported		Assumed very slight
1350 F	Not reported		Assumed very slight
1500 F	Not reported		Assumed very slight

Microstructures (×1000 D)

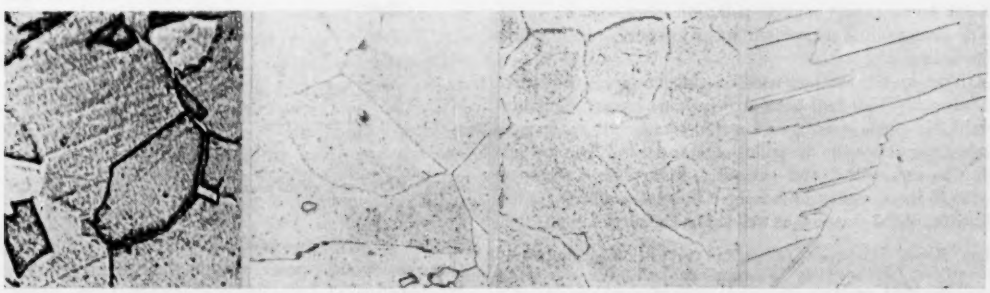

Unexposed
Etchant: Ferric chloride

6 months, 1200 F

6 months, 1350 F
Etchant: Glyceregia

6 months, 1500 F

Blast-Furnace-Gas Cleaning for Iron and Ferromanganese Production

J. S. MACKAY
J. F. KEARNS
Pittsburgh Coke & Chemical Company, Pittsburgh, Pa.

A process for removing the superfine smokes from ferromanganese blast-furnace gases having low investment and low operating cost is described. This method solves both the air and stream-pollution problems. The ferro blast-furnace gas is cleaned from 10 to 15 grains per cu ft to less than 0.01 grains per cu ft by a wet-washing procedure in a Pease Anthony venturi scrubber. The alkali cyanide stream-pollution problem is solved by the control of pH and complete recycle of the liquors so that the cyanide is stripped by the incoming gas and is subsequently burnt in the stoves or boilerhouse. The liquor is separated from solids in a Dorr thickener. The solids are removed in the underflow as a thick slurry which is either returned to the furnace or dumped in a pit in the ore yard. The overflow is pumped back to the venturi. The chemistry and physical equipment of the process are described.

THE REMOVAL of the dense-fine fume which occurs in the production of ferromanganese in the blast furnace is much different from that in an iron blast furnace. C. A. Bishop, et al.,[1] have very adequately described the problem and the make-up of the fume. As they have stated, the solids present in the gas are 80 per cent between 0.1 and 1.0 micron. At one time, this was discharged to the atmosphere as a dense fume. This was not only obnoxious but was economically wasteful since the fuel value of the gas was not used. This fume is largely condensed vapors which were volatilized in the high-temperature part of the furnace and condensed in the cooler zone as a smoke. One of the groups of materials not made in quantity in the blast-furnace operation but which is produced in the ferromanganese furnace due to a combination of higher temperature and different chemistry is the alkali-metal cyanides. This poses the second problem. Wet-washing procedures are more efficient in removing fine fumes but cyanide wastes cannot be disposed of in the Ohio River. The solution worked out by Bishop, et al.,[1] was electrostatic precipitation with subsequent burning of the dust and briqueting. This process involves large investment and high maintenance and is considered less efficient in removing fine fumes. For these reasons and others, Pittsburgh Coke & Chemical decided to solve the problem, if possible, by a wet-wash system. This has been successfully done and will be described. If wet washing is used, the problem becomes one of river pollution more than air pollution. The river-pollution problem was solved in order to solve the air-pollution problem.

In addition to the method used at the Duquesne Works of United States Steel,[2] it had been shown that a wet-washing system combining a gas washer and a Thiesen disintegrator gave satisfactory gas under the air-pollution standards. The cyanide problem was not solved and the solid slurry was difficult to handle due to its tendency to cement. This latter quality is due to the fineness of the material as well as the chemical composition. Not only is the plugging problem existent in the aqueous solutions but also in the lines containing the wet gas. The Thiesen disintegrator rotating bars would be coated with a very hard cement-like material. For this reason two disintegrators were deemed necessary.

The process involves very low investment, has very low maintenance charges, and has been eminently successful in solving both the air and stream-pollution problems. In brief, the process involves passing the gases from the normal dust collector through a Pease Anthony venturi scrubber to a gas main feeding to either the stoves or boiler house. The wash water of the venturi scrubber goes to the Dorr thickener where the solids are discharged as a sludge either to the skips or to the ore yard and the overflow effluent is recycled to the venturi. This will be described in more detail later.

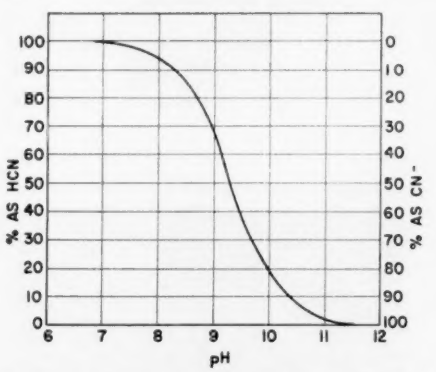

Fig. 1 HCN has a vapor pressure and is removable; $M^+ CN^- = HCN + MOH$

A study of the two methods used for cleaning the gas showed that the advantages were certainly on the side of wet-scrubbing if the plugging and cyanide-pollution problems could be solved. The alkali cyanides are formed in the furnace by fixation of nitrogen from the air in the hot zone. These are condensed in the cooler part of the furnace to a smoke and essentially are nonvolatile from there on. When they are wet by water, they dissolve and partially decompose to HCN if the pH is at the proper level. The more acidic the solution, the more the decomposition. Fig. 1 shows the degree of decomposition with pH. Pure HCN boils at 27 C, but is readily soluble in water. The vapor pressure is suf-

[1] Bishop, Brisse, Thompson, Liebel, and Swaney, "Cleaning Ferromanganese Blast Furnace Gas," Yearbook of the American Iron and Steel Institute, 1951, pp. 459–475.

[2] C. H. Good, "Ferromanganese Gas Cleaning at Duquesne Works," Blast Furnace, Coke Oven, and Raw Material 1954 Proceedings, AIME, pp. 169–178.

Presented at the Pittsburgh Bicentennial Conference of the ASME Pittsburgh Section on Pollution Problems and Their Solution, April 20–21, 1959.

NOTE: Statements and opinions advanced in papers are to be understood as individual expressions of their authors and not those of the Society. Manuscript received at ASME Headquarters, May 8, 1959.

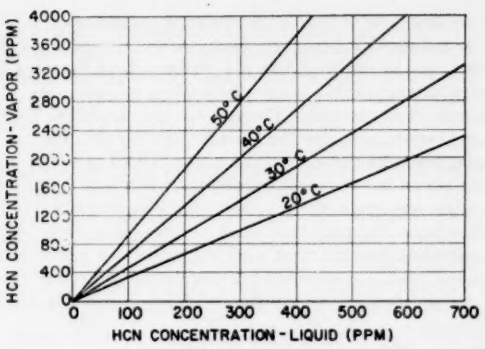

Fig. 2 Equilibrium data for HCN-water-air system at 20, 30, 40, and 50 C

ficiently high to be removed by aeration, preferably with acidic gases so that pH is kept at the lower levels. The solids in the gas are largely alkaline and one would presume the liquor to be highly alkaline. However, there is considerably more carbon dioxide than total alkali so if proper absorption is allowed the pH could be acidic enough for HCN stripping. This could not be done simultaneously with solution of the cyanide but if the liquor could be cycled back to the scrubbers a large part of the HCN would be removed in the gases. The vapor pressures of various concentrations of HCN in water are shown in Fig. 2. It was known that recycle of these liquors was nearly impossible and that even on iron-blast-furnace-gas wash water, attempts at recycle had been unsuccessful. On examining the analysis of river water and the time available for treatment of the water in the Dorr thickener, it was felt that the Dorr thickener effluent could be prepared to be at least as good as that obtained from the river. On investigation of the reasons for failure of the recycle on blast-furnace water, it was found that at least in one case the liquor was pumped to a spray-pond cooling system and then back to the gas washer. The plugging occurred at the elbows on the return line. This plugging could well have been due to supersaturation in the air-cooling pond. As a matter of fact, it was found possible to recirculate when the sprays were shut off. At the pH desired for cyanide removal from the liquor, calcium-carbonate solubility is roughly at its minimum. One of the very obvious ways in which cement formation could start in a wet system was by increasing the calcium solubility either with more acid or more alkaline conditions and then reducing the solubility by changing the pH. In many cases, this would happen at the points where plugging could be the worst problem. If the water was completely recycled some cooling advantage obtained in the use of fresh water would be lost. As a matter of fact, it is obvious that almost all cooling would have to be by evaporation. Calculation shows that this was the major method of cooling anyway and an equilibrium liquor temperature should be arrived at around 150 F.

The first proposed system consisted of feeding the gas into a stripped-gas washing tower and spraying with approximately 2500 gpm of water. Sprays were also installed at every piping bend. After passing through the washing tower, gas would then be fed into a rotary Thiesen disintegrator where it would be sprayed again with about 250 gpm of water. The gas leaving the disintegrators was expected to be exceptionally clean. The disintegrator would clean the gas no matter what the dust loading, whereas an electrostatic precipitator efficiency is based upon the dust loading fed into it. The water discharging from the cooling tower and the disintegrator goes to the Dorr thickener. It was planned to remove the cyanide before discharging the liquor to the river by chlorination. The Wallace & Tiernan method of continuous chlorination in which the cyanide is oxidized to cyanate was to be used. This chlorination might be before the Dorr thickener so that it could be used for the retention tank, or on the effluent after the thickener, in which case a retention tank had to be added. The State Health authorities of Pennsylvania will not allow chlorination only to cyanate which is the normal procedure elsewhere. They require full chlorination to N_2 and CO_2. Furthermore, they would not accept the continuous-chlorination process of Wallace & Tiernan but insisted on batch chlorination in which all the liquor of one lake is tested free before discharge to the river. They would consider proof of a continuous process but required at least a long run on a pilot scale before acceptance. This would automatically require a batch system anyway. Roughly, the cost rose from $6 to $15 per ton ferromanganese and it was decided that either the water would have to be partially recycled so that only part would be chlorinated, or it would be necessary to operate on complete recycle.

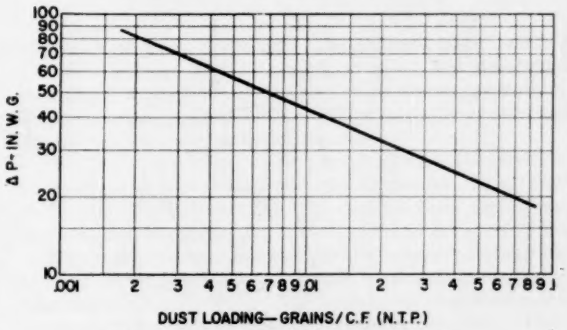

Fig. 3 Summary of blast-furnace venturi data

It was decided to operate on complete recycle. At the same time, another change was made. It appeared for several reasons that the use of a Pease Anthony venturi scrubber in place of water sprays in the gas washer would be desirable. There was plenty of pressure for the specified pressure drop to give a guaranteed cleanliness of 0.03 grains per cu ft on basic iron and 0.08 grains per cu ft on ferromanganese. This required only 600 gpm of water as compared to 2500 in the old system. Fig. 3 shows the guarantee of solid content of the gas effluent from the Pease Anthony scrubber. At the same time, it was decided to combine the two furnace-gas and liquor systems from A and B furnaces so that a venturi was to be put on both furnace gases with both liquors going to the same Dorr thickener, and the effluent recycled back to each venturi. The gas was to go to a common main and through the Thiesen disintegrators to the stoves or directly to the boilerhouse. In the previous system, a new Dorr thickener had to be supplied to handle the amount of liquor for the two furnaces. There are two advantages to the revised system. One, the gas from the ferromanganese unit would be diluted before going through the disintegrator. And second, the cyanide would be stripped with two furnace gases rather than one. The one disadvantage was that the cyanide content would be considerably higher due to the lower amount of water. Again, of course, dilution from the other furnace would be helpful. Of course, a shut down on both furnaces was being risked if the system did not work. The amount of water required for the sprays in the disintegrator was decreased from 250 to 150 gpm. The old gas washers or coolers were retained as knockout chambers for the gas after the venturi. The venturi was modified as shown in Fig. 4 so as to better handle any tendency for solid plugging.

The whole system as finally designed is shown in Fig. 5. Water sprays to both of the gas washers had been included so that if necessary solution could be pumped to there as well to the venturi to get CO_2 absorption for pH control. Obviously, while solid

pickup is excellent in a venturi scrubber, gas absorption would be very small because of contact time. Gas stripping from a solution did not require this contact time, although again pumping Dorr effluent to the gas washers would be helpful in lowering the cyanide content somewhat more.

It is this design, shown in Fig. 5, that has been used successfully. The gas at the top of the blast furnace is cooled from 900+ to 600 to 700 F by water sprays. This gas passes from the furnace to the dust catcher and from the dust catcher into the venturi scrubber where it is sprayed with 600 gpm of recycle water. The pressure drop was from 30 to 70 in. of water and the velocity through the throat of the venturi ranged from 250 to 400 fps. This is the reason for the exceptionally good cleaning obtained. This gas then goes to the old gas washer or cooling tower with the hurdles and packing removed. As mentioned, water may or may not be added in sprays in this gas washer. Both furnaces have identical arrangement. The gas goes into a common main and a portion of it is channeled through the disintegrators for final cleaning before going into the blast-furnace stoves. The gas discharging from the disintegrators ran from 0.0005 to 0.0001 grains of solid per cu ft. In fact it was hardly measurable. The scrubbing water from both furnaces feeds to the Dorr thickener. The overflow water from the Dorr thickener flows to a sump which is maintained at constant level with make-up water and from here is pumped back to each venturi or can also be pumped to the gas washers and to the disintegrators. Make-up water is required

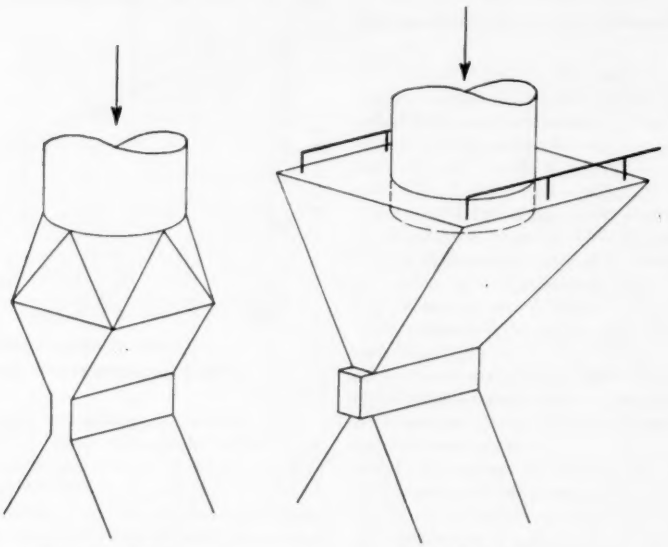

Conventional design P. C. & C. design

Fig. 4 Venturi redesign

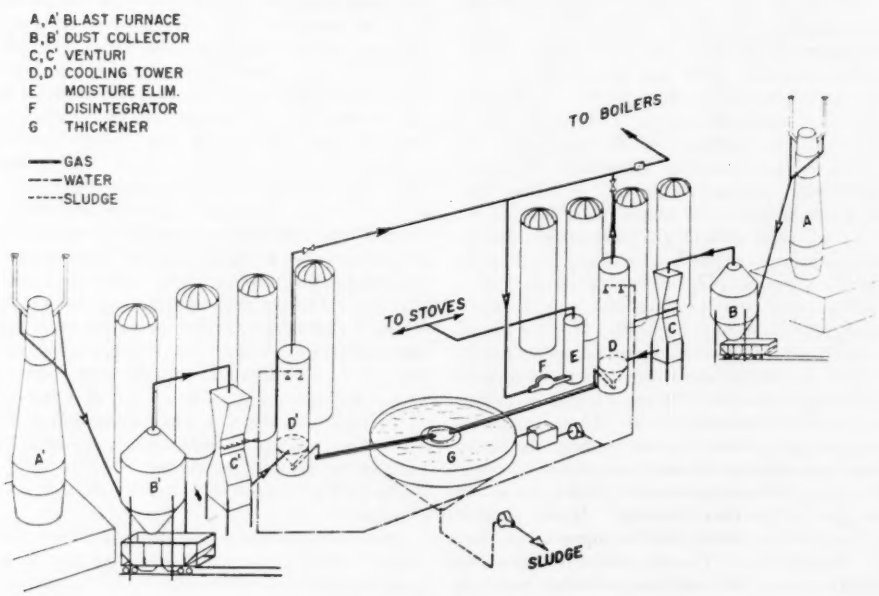

Fig. 5 Gas cleaning system

to replace the evaporation losses and that removed in the Dorr underflow concentrate. The pump capacity at the bottom of the thickener was higher than desired to maintain a reasonably thick underflow if discharged directly so part of this was recycled to the top feed of the Dorr. A bypass from this fed to either the skips of both furnaces or into a pit in the ore yard. The only change contemplated in this system is a filter for the Dorr thickener sludge.

This system was installed in the summer of 1957 and went into operation in the fall of 1957 with both furnaces on basic iron. No problems were experienced except that there was some difficulty in initial periods in getting adequate settling in the Dorr thickener. The pH steadied out to 9 to 9.5 and the gas cleaning was excellent. This was an excellent time to run a control experiment to determine the efficiency of the cyanide stripping in order to know what the hazards could be around the Dorr thickener and at the various sumps and how efficient the cyanide stripping could be. One ton of sodium cyanide was pumped into the A flume as an aqueous solution such that the HCN equivalent was about 3 lb per min. The effluent from the Dorr thickener (capacity of 300,000 gal) rose to 220 ppm of HCN in 7 hr. The atmosphere was tested at all likely points. Concentration was less than 15 ppm. Industrial atmosphere limit is 20 ppm. High concentrations existed in closed sumps. The cyanide was rapidly removed at the venturi, the total content dropped rapidly after addition of sodium cyanide stopped and was down to 50 ppm in 5 hr. The maximum removal rate was 1.5 lb HCN per min, whereas the addition was 3 lb per min so that maximum equilibrium concentration had not been reached. It was found that atmospheric dilution of the cyanide in the atmosphere was very rapid. For example, on opening a closed sump containing the effluent from the Dorr thickener, the cyanide concentration at foot level was 60 ppm. This became 15 at waist level and 5 ppm at head level when standing in a direct steam flow rising from the sump. The Dorr thickener had been surrounded with an 8-ft wall of transite siding. The HCN concentration inside this wall on the bridge over the lake was approximately 3 ppm and was essentially undetectable at the roof of the wall. This experiment provided confidence in going ahead with the ferromanganese run so far as personnel danger and cyanide stripping was concerned.

Also during this 3-month period of operation in which the two furnaces were on complete recycle for several-week periods, no plugging of the return lines, the sprays, nor the throats of the venturi scrubbers was noticed.

Operation started on spiegeleisen which is very similar to that of ferromanganese and also gives high cyanides. At this time, B furnace was also operating. Cyanides rose very rapidly in the Dorr thickener and leveled out at about 200 ppm of cyanide. Toxicity measurements in the general areas fitted very closely with the earlier experiment described. No trouble was noticed in the recycle and the pressure drop across the venturi showed no problem. The gas was cleaned out of the venturi scrubber to less than 0.01 grains per cu ft. At this time, the disintegrator was used for the gas going to the stoves. Ferromanganese was started and again no problems resulted, but the cyanide in the Dorr thickener did rise to from 250 to 400 ppm. There was a slow increase in pressure drop across the venturi on A furnace which was on ferromanganese. There was none, however, at B furnace showing that the build-up was not due to the recycle water since this was identical for each venturi, but rather to the dust-laden gas hitting the sprays. There was no particular difficulty in cleaning out the venturi when the pressure drop rose above 70 in. of water. The results on the ferromanganese gas are shown in Fig. 6. The soluble solids rose to 1.8 per cent. These salts were 94 per cent K and Na carbonates and chlorides. The solids content of the Dorr overflow kept in good control after the

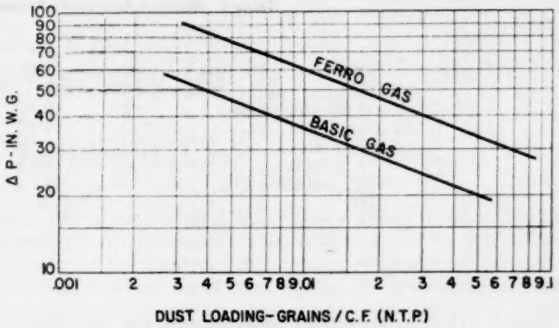

Fig. 6 Summary of blast-furnace venturi data

start-up when again it was high. The pH maintained itself in a 9.0 to 10.5 range so that cyanide stripping was maintained throughout without having to pump water to the gas washers. The system has been used continuously for the past year and a half though only part-time on ferromanganese.

Prior to the installation of the present system, the blast-furnace stoves had to be cleaned out every six months. In the total of the past year and a half, a stove has not been cleaned and small checker openings have been installed to get some 30 per cent more efficient hot-blast heat for the furnace operations and to allow higher temperatures resulting in substantial savings in coke and production costs. The boilerhouse blast-furnace gas burners formerly required monthly maintenance cleaning. These burners have not been cleaned for over a year and a half. All maintenance charges have certainly been at a minimum.

The heat balance came out as predicted and the water out of the venturi is at 150 F, the gas slightly above this, and roughly 15-F cooling is obtained in the cycle in the Dorr thickener. The water fed back to the venturi is at 135 F. There is one disadvantage in that rather wet gas has to be taken into the gas mains. Actually there is no trouble in handling this gas either for stove underfiring or for boilers. A fair amount of condensation is obtained in the drip legs in the lines to the burners. This water contains some HCN since it is in equilibrium with the gas and the water can be recirculated to the Dorr thickener. The disintegrator worked equally well on recycle water or Ohio River water. As a matter of fact, it worked better on recycle water because it was unnecessary to filter. Actually the use of disintegrators has been stopped and again there was no trouble with the ferromanganese gas. During the two periods of eight-weeks operation there was no plugging in recycle lines. There was never any trouble on the B-furnace system in the venturi. Some build-up did occur in the venturi on A furnace. We are not sure that this might not have been due to a few periods when recycle water was lost for short periods.

In the second long run, it was decided to operate on one furnace alone. This was partly necessitated by the shutdown of the other furnace. In this case, the pH of the overflow water gradually rose to 12 and the cyanide level rose to above 1500 ppm. While this would be a very dangerous level of cyanide at lower pH's it caused no problems at all in this case. The reason is explained in Fig. 1 which shows that the potassium cyanide was not decomposed and there would be essentially no free HCN in the solution. Thus the vapor pressure would be essentially zero. However, it was not desired to continue this and the alternative mentioned earlier was adopted. Water was pumped to the gas washer so that carbon-dioxide absorption would occur. In a matter of a few hours, the pH dropped to 10.5 and the cyanide dropped to its original level of 600 ppm.

The material balance for the one furnace system is shown in

Table 1 Material-flow single-furnace operations, furnace A, in lb per min

Material	Venturi gas In	Venturi gas Out	Water In	Water Out	Dorr Thickener discharge Underflow	Dorr Thickener discharge Overflow
Water	440	840	5000	4600	666	3500
Total filtrable solids	54	0.07	0.8	54	54	0.8
Total solids	...	0.07	68	(144)	58	68
CN total	...	...	3.2	4.4	0.3	3.2
soluble	...	...	3.2	3.9	0.3	3.2
CO_2 (including CO_3)	454	441	17	31.2	10	17
NH_3	...	...	1.14	1.32	0.13	1.14
Ca	...	...	...	10.5	8.4	...
K	...	...	21	25	2.8	21
Na	...	...	2.8	4	0.4	2.8

Table 1. Unfortunately the cyanide content was not obtained either in the entering or outlet gas so the production rate is not available at this time. This was run on hourly composites over an 8-hr period. The soluble salts had been at equilibrium for some time. The balance is not very good in places but it does give a reasonable picture of what is going on.

In a balance run on the two-furnace system, the gas from A furnace contained 60 lb of dust per min and B furnace 20 lb per min. Solution to B venturi had 250 ppm of cyanide and came out at 100 ppm. The drip legs have contained from 60 to 80 ppm of cyanide showing that good equilibrium is attained.

In the two-furnace system, water never had to be pumped to the gas washers. All the data will be gathered together and full details published on solid flows, rates, material balances, solids build-up, and so forth, in a later publication. This would be out of place in a discussion of air pollution.

Thus it is known that the process can operate with very low atmospheric pollution, no river pollution, essentially no personnel hazard, and very low maintenance. It is also known that this can be done with the lowest investment commensurate with any gas-treatment system. It is not known what problems would result from having gas coolers so that variable temperatures of a liquid system would exist. It is not known how long the process could run without a cleanout. Certainly, observation has shown that it could be considerably over the eight-weeks period and there is no point at which it would be difficult to remove even the hardest solids.

United States Patent No. 2,877,086 has been issued covering the process as described.

Influence Coefficients for Open-Crown Hemispheres

G. D. GALLETLY

Mechanical and Electrical Engineering Department, Emeryville Research Center, Shell Development Company, Emeryville, Calif. Assoc. Mem. ASME

Stresses and deflections of hemispherical shells with nozzle openings lying on the axis of symmetry may be determined accurately and rapidly with the aid of the tables given in the paper. The tables give the influence coefficients (i.e., stresses and deflections obtained with unit applied loads) for the edge and interior points for various types of edge bending load. The radius-thickness ratios of the hemispherical shells considered varied from 15 to 250; the total central angle of the opening varied from twenty to one hundred degrees.

An illustration of the utility of the coefficients is given by considering a hemisphere-cylinder intersection problem.

Introduction

HEMISPHERICAL SHELLS with crown openings (see Fig. 1) are frequently used in a number of industries as portions of a complete pressure vessel. In order to design these vessels properly at their point of attachment with the cylindrical nozzle it is necessary to undertake a bending analysis of both the open-crown hemisphere and the cylinder. The reason for this is, of course, because the pressure loading will cause the two parts of the vessel to undergo different elastic displacements (and rotations if the pressure is not uniform). Since both cylinder and open-crown hemisphere must fit together eventually, this means that axisymmetric edge moments and edge transverse shears will be produced at their common junction. These edge moments and shears then cause bending in the cylinder and hemisphere. The analysis of the bending of the cylinder is well-known and offers little difficulty (Timoshenko [8]).[1] The bending analysis of the open-crown hemisphere, however, is not so easy.

In order to determine the unknown edge moments and shears acting at a junction the designer would like to have available the edge influence coefficients (by edge influence coefficient is meant the displacement or rotation at an edge due to a unit moment or shear applied at the edge or the far edge). If these are available for the various shells meeting at a junction, then the formulation of the compatibility equations is relatively simple. Solving the compatibility equations then yields the unknown edge moments and shears. The final stress distributions can then be quickly determined if the interior influence coefficients are also available.

The problem of determining the edge influence coefficients for hemispheres with crown openings has been investigated before by Galletly [3]. In that work he selected a specific hemispherical shell (radius-thickness ratio of 90.5, total central opening of 21 deg) and compared the results obtained by different methods for calculating the edge influence coefficients. The criterion of accuracy used in that investigation was a solution due to Love [6] which involves associated Legendre functions of complex degree. It was found that an approximate Geckeler-type solution gave errors in the edge influence coefficients of about 15 per cent; the use of the approximation $\cot \phi \approx 1/\phi$ (which yields a solution in terms of Kelvin functions of zero order) was better in that it gave errors of only 5 per cent.

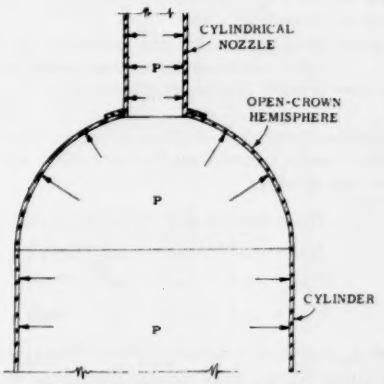

Fig. 1 Open-crown hemisphere used as a pressure vessel head

While the work cited is of value, it is of limited application since only one shell geometry and size of opening was investigated. Also, interior influence coefficients were not considered. It would, of course, be possible to consider various shell geometries and determine the ranges over which the $\cot \phi \approx 1/\phi$ approximation gave good results. However, it was felt to be more profitable to calculate the influence coefficients by numerical integration of the differential equations of equilibrium. In this way no approximations need be made and the influence coefficients are immediately available without having to resort to consulting other tabulations to calculate them.

Purpose and Scope of the Present Work. The aim of the present investigation was to determine the edge and interior influence coefficients for open-crown hemispheres subjected to edge bending moments and edge shearing forces. The coefficients were obtained by numerically integrating the classical small-deflection differential equations of equilibrium (given in the Appendix) on a high-speed digital computer. The ranges of the parameters covered were as follows:

$$r/h = 15, 25, 50, 75, 100, 125, 150, 200, 250$$
$$\phi_2 = 50, 40, 30, 20, 10 \text{ deg}$$

where

r = radius of hemisphere
h = thickness of hemisphere
ϕ_2 = semiangle subtended by the opening (see Fig. 2)

The governing differential equations were rendered dimensionless as were the edge bending loads and the influence coefficients. Thus the results given apply to many more shells than just those investigated.

[1] Numbers in brackets designate References at end of paper.

Contributed by the Power Division and presented at the Semi-Annual Meeting, St. Louis, Mo., June 14–18, 1959, of THE AMERICAN SOCIETY OF MECHANICAL ENGINEERS.

NOTE: Statements and opinions advanced in papers are to be understood as individual expressions of their authors and not those of the Society. Manuscript received at ASME Headquarters, February 5, 1959. Paper No. 59—SA-4.

Methods Used to Determine the Influence Coefficients

From equations (37), (38), and (39) in the Appendix it can be shown that the meridional bending moment M_ϕ and the horizontal shearing force H_ϕ (see Fig. 2) may be expressed as follows:

$$M_\phi = -\frac{1}{12(1-\nu^2)(r/h)^2} \{A[\nu f(x_1) - \mu^2 r f(y_1)] + B[\nu f(y_1) + \mu^2 r f(x_1)] + C[\nu f(x_2) - \mu^2 r f(y_2)] + D[\nu f(y_2) + \mu^2 r f(x_2)]\} \quad (1)$$

$$rH_\phi = \frac{1}{\sin\phi}[Ax_1 + By_1 + Cx_2 + Dy_2] \quad (2)$$

where

$$\left.\begin{aligned} A, B, C, D &= \text{constants chosen to satisfy the boundary conditions} \\ \nu &= \text{Poisson's ratio} \\ \mu^2 r &= [12(1-\nu^2)(r/h)^2 - \nu^2]^{1/2} \\ \phi &= \text{co-latitude angle} \\ x_1 \ldots y_2 &= \text{linearly independent solutions of the homogeneous differential equations} \\ f(\ldots) &= d/d\phi(\ldots) + \nu\cot\phi\,(\ldots) \end{aligned}\right\} \quad (3)$$

The boundary conditions of the problem are shown in Fig. 2. Using these boundary conditions in conjunction with the equations given one obtains:

$$\left.\begin{aligned} rH_{\phi_0} &= a_{11}A + a_{12}B + a_{13}C + a_{14}D \\ M_{\phi_0} &= a_{21}A + a_{22}B + a_{23}C + a_{24}D \\ rH_{\phi_2} &= a_{31}A + a_{32}B + a_{33}C + a_{34}D \\ M_{\phi_2} &= a_{41}A + a_{42}B + a_{43}C + a_{44}D \end{aligned}\right\} \quad (4)$$

where the a_{ij} represent numerical values. The system of equations (4) can be written more conveniently in the matrix form

$$\{x\} = [a]\{y\} \quad (5)$$

where the vector x represents the edge moments and shears, y the constants $A \ldots D$, and the square matrix a represents the a_{ij}.

Solving equation (5) in the usual way one finds for the constants $A \ldots D$:

$$\{y\} = [a^{-1}]\{x\} \quad (6)$$

Equation (6) gives the constants $A \ldots D$ in terms of the edge moments and shears acting at both edges, i.e., $\phi = 90$ deg and $\phi = \phi_2$. To determine the influence coefficients for any particular loading, say a unit moment at $\phi = \phi_2$, the following procedure is adopted:

(i) M_{ϕ_0}, H_{ϕ_0}, and H_{ϕ_2} are set equal to zero in equation (6). This then determines the values of the constants $A \ldots D$ which are consistent with the applied loading of $M_{\phi_2} = 1$.

(ii) The results of step (i) are then used in conjunction with equations (37) to (40) and the numerical integration results. This then determines the required influence coefficients.

The coefficients for the other edge loadings are found in a similar manner.

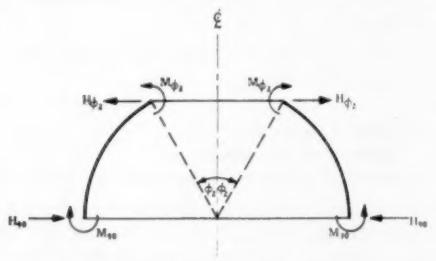

Fig. 2 Boundary conditions of problem

Edge Loadings Considered and the Quantities Tabulated

In order to avoid using a specific value of r the quantities tabulated for various values of r/h were:

$$Er^2V,\ Er\delta,\ rN_\theta, \text{ and } M_\phi$$

where

- V = angle of rotation of a tangent to a meridian (+ when the positive semitangent turns inward)
- N_θ = circumferential direct stress resultant (+ when tensile)
- M_ϕ = meridional bending stress resultant (+ when producing tension on inner surface)
- δ = horizontal displacement (+ outward)
- r = radius of hemisphere
- E = Young's modulus

The other stress resultants N_ϕ and M_θ are usually not the controlling ones and, hence, have not been given.

A not unexpected result was also found for the influence coefficients. This was that the influence coefficients at the edge away from the edge where the loading was applied were insignificant. That is to say, an edge effect existed. Even in the worst case ($r/h = 15$, $\phi_2 = 50$ deg) the influence coefficients at the distant edge were less than 10 per cent of those where the loading was applied. Thus, in the tabulation of the influence coefficients (Tables 1 to 3), it was assumed that there was no interaction between the two edges.

The tables list first the influence coefficients at $\phi = 90$, 85, and 80 deg due to edge loadings at $\phi = 90$ deg. The two edge loadings considered are shown in Fig. 3(*a*). The first lines in the influence coefficient tabulation correspond to the rH_ϕ-loading, the second lines to the M_ϕ-loading.

The coefficients due to edge loadings at the various ϕ_2-angles are tabulated next. In each case the influence coefficients are given for $\phi = \phi_2$, $\phi_2 + 5$, $\phi_2 + 10$ deg due to edge loadings at ϕ_2. The two edge loadings considered for the crown opening are shown in Fig. 3(*b*). As was the case for $\phi = 90$ deg, the first lines in the tabulation correspond to rH_ϕ-loadings, the second lines to M_ϕ-loadings.[2]

[2] An illustration of the accuracy of the numerical results is afforded by computing the edge influence coefficients for a shell with $r/h = 200$, $\phi_2 = 10$ deg. For this case, the cot $\phi = 1/\phi$ approximate method (Galletly, [3]) should be quite good. The results obtained were

For $rH_{\phi 2} = 1$, $Er\delta = 237.04$ and $Er^2V = 20{,}735$
For $M_{\phi 2} = 1$, $Er\delta = 20{,}735$ and $Er^2V = 4{,}381{,}600$

The discrepancy between these values and those in Table 3 (for $r/h = 200$, $\phi_2 = 10$ deg) is less than 2 per cent.

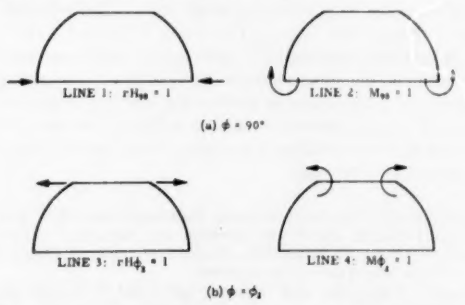

Fig. 3 Axisymmetric edge loadings considered in influence coefficient tabulations

Table 1 Influence coefficients at and near the edge for r/h = 15, 25, and 50

	r/h = 15				r/h = 25				r/h = 50			
	Er^2V	$Er\delta$	rN_θ	M_ϕ	Er^2V	$Er\delta$	rN_θ	M_ϕ	Er^2V	$Er\delta$	rN_θ	M_ϕ
$\phi_1 \rightarrow 90$	747.11	−149.36	−9.9573	...	2072.3	−321.35	−12.854	...	8271.3	−908.64	−18.173	...
	−7421.4	747.11	49.807	1.0000	−26555	2072.3	82.892	1.0000	−150135	8271.3	165.43	1.0000
85	643.77	−87.609	−5.8711	−.05484	1633.8	−155.07	−6.2310	−.04731	5300.1	−288.39	−5.7898	−.03554
	−4371.7	236.96	15.786	.86167	−12849	379.80	15.147	.78810	−47655	−19.083	−.53755	.64095
80	444.91	−40.500	−2.7388	−.06472	908.11	−45.592	−1.8436	−.04597	1674.0	1.5298	.04219	−.02269
	−2027.1	−33.450	−2.4345	.59625	−3767.4	−301.75	−12.458	.43756	611.49	−1682.9	−34.376	.20288
$\phi_2 \rightarrow 50$	549.03	91.837	7.7995	...	1538.9	195.60	10.021	...	6203.9	547.42	14.099	...
	7145.1	549.03	47.781	1.0000	25800	1538.9	80.356	1.0000	147185	6203.9	161.97	1.0000
55	461.70	54.435	4.3796	.04000	1183.3	95.381	4.6282	.03469	3874.3	175.20	4.2773	.02616
	4057.9	160.38	13.583	.81739	12040	244.22	12.697	.74947	45085	−158.80	−2.7099	.61114
60	311.28	25.270	1.9501	.04567	641.72	27.736	1.2990	.03260	1196.9	−3.4910	−.05519	.01616
	1821.2	−48.996	−3.2737	.54179	3420.9	−284.77	−12.555	.39902	−520.66	−1440.5	−32.672	.18543
$\phi_2 \rightarrow 40$	450.82	65.782	6.5928	...	1269.6	139.60	8.4571	...	5151.7	389.41	11.886	...
	6998.2	450.82	46.757	1.0000	25430	1269.6	79.008	1.0000	145850	5151.7	160.29	1.0000
45	375.60	39.080	3.6235	.03266	966.64	68.340	3.8302	.02846	3185.4	125.06	3.5362	.02154
	3907.0	128.09	12.808	.79681	11682	188.95	11.756	.73248	44040	−180.11	−3.4688	.59842
50	251.20	18.189	1.5873	.03688	519.39	19.980	1.0637	.02645	978.04	−2.9473	−.04716	.01316
	1726.9	−45.771	−3.2901	.51791	3267.7	−252.85	−12.371	.38389	−459.59	−1253.1	−31.885	.17876
$\phi_2 \rightarrow 30$	337.33	40.833	5.1846	...	360.99	86.217	6.6375	...	3937.6	239.21	9.3083	...
	6782.3	337.33	44.976	1.0000	24870	960.99	76.879	1.0000	143705	3937.6	157.50	1.0000
35	277.26	24.333	2.7597	.02419	721.64	42.395	2.9159	.02130	2400.4	77.231	2.6905	.01625
	3695.3	90.666	11.521	.76449	11168	128.61	10.418	.70556	42474	−192.36	−4.4763	.57891
40	183.53	11.440	1.1889	.02690	384.08	12.488	.79729	.01948	732.13	−2.0602	−.03317	.00977
	1604.3	−42.111	−3.4577	.48429	3085.2	−212.18	−12.099	.36118	−356.17	−1020.8	−30.645	.16924
$\phi_2 \rightarrow 20$	212.75	20.047	3.6257	...	620.01	41.879	4.6159	...	2594.7	115.00	6.4427	...
	6370.3	212.75	41.470	1.0000	23755	620.01	72.511	1.0000	139430	2594.7	151.73	1.0000
25	171.06	11.949	1.8131	.01483	455.06	20.709	1.9162	.01340	1544.6	37.503	1.7697	.01044
	3320.5	51.265	9.3909	.70208	10230	66.481	8.2617	.65432	39649	−190.56	−5.9178	.54258
30	111.89	5.7366	.76303	.01614	239.52	6.2719	.51754	.01198	468.58	−.97054	−.01150	.00614
	1407.0	−35.207	−3.5583	.42494	2777.9	−159.59	−11.354	.32182	−156.18	−743.89	−28.292	.15324
$\phi_2 \rightarrow 10$	82.838	6.0164	2.0143	...	258.23	12.079	2.4870	...	1157.5	32.002	3.3903	...
	5227.1	82.838	31.802	1.0000	20460	258.23	59.483	1.0000	126220	1157.5	133.31	1.0000
15	63.730	3.4683	.82808	.00510	180.78	5.9416	.87518	.00509	655.14	10.697	.81565	.00433
	2407.0	14.358	5.2581	.53643	7853.1	10.799	4.1939	.51656	32387	−155.71	−7.7619	.44550
20	41.495	1.7714	.33688	.00552	94.898	2.0191	.24116	.00446	201.68	.05774	.01899	.00248
	971.75	−21.310	−2.9826	.29129	2075.0	−88.390	−8.7733	.23218	291.80	−407.96	−22.109	.11741

NOTE: The first line (of the 2-line groups) in this and the following tables corresponds to a loading perpendicular to the axis of symmetry ($rH_\phi = 1$); the second line corresponds to a moment loading ($M_\phi = 1$). See Fig. 3.

Table 2 Influence coefficients at and near the edge for $r/h = 75$, 100, and 125

	$r/h = 75$				$r/h = 100$				$r/h = 125$			
	Er^2V	$Er\delta$	rN_θ	M_ϕ	Er^2V	$Er\delta$	rN_θ	M_ϕ	Er^2V	$Er\delta$	rN_θ	M_ϕ
	18603	−1669.5	−22.259	...	33065	−2570.4	−25.704	...	51658	−3592.4	−28.739	...
$\phi_1 \rightarrow 90$	−413760	18603	248.04	1.0000	−849410	33065	330.65	1.0000	−1483900	51658	413.27	1.0000
	9801.6	−356.79	−4.7727	−.02813	14398	−364.18	−3.6517	−.02287	18622	−320.36	−2.5679	−.01890
85	−88324	−1801.9	−24.300	.52705	−120000	−4966.2	−50.050	.43561	−131595	−9335.1	−75.171	.36063
	1517.0	84.692	1.1566	−.01208	550.83	166.97	1.7034	−.00650	−921.16	232.43	1.8942	−.00338
80	21936	−3399.4	−46.183	.08192	56858	−4866.9	−49.534	.01694	98430	−5814.0	−47.303	−.01763
	14012	1001.1	17.232	...	24967	1537.1	19.872	...	39070	2144.0	22.198	...
$\phi_2 \rightarrow 50$	407195	14012	243.89	1.0000	837810	24967	325.92	1.0000	1465850	39070	408.02	1.0000
	7192.8	214.90	3.5125	.02074	10591	217.35	2.6763	.01687	13720	188.71	1.8708	.01395
55	83913	−1662.3	−25.666	.50311	114310	−4254.9	−50.431	.41608	125610	−7792.0	−74.534	.34458
	1097.7	−56.642	−.84916	.00862	419.66	−108.62	−1.2358	.00465	−622.78	−149.61	−1.3679	.00242
60	−20061	−2848.9	−43.385	.07461	−52209	−4038.3	−46.288	.01495	−90587	−4793.2	−44.055	−.01680
	11662	710.91	14.516	...	20806	1090.4	16.733	...	32586	1519.8	18.685	...
$\phi_2 \rightarrow 40$	404250	11662	241.91	1.0000	832645	20806	323.68	1.0000	1457850	32586	405.56	1.0000
	5926.7	152.98	2.9014	.01710	8737.7	154.26	2.2083	.01393	11330	133.35	1.5412	.01152
45	82152	−1485.3	−26.065	.49312	112075	−3714.4	−50.416	.40804	123310	−6743.5	−74.106	.33804
	902.88	−41.519	−.69568	.00703	354.51	−79.143	−1.0113	.00379	−492.94	−108.75	−1.1190	.00197
50	−19305	−2464.2	−42.221	.07195	−50398	−3483.7	−44.994	.01432	−87577	−4127.7	−42.793	−.01639
	8948.9	435.61	11.356	...	16001	667.09	13.082	...	25097	928.85	14.602	...
$\phi_2 \rightarrow 30$	399550	8948.9	238.64	1.0000	824430	16001	320.02	1.0000	1445200	25097	401.55	1.0000
	4483.0	94.159	2.2060	.01294	6623.9	94.591	1.6774	.01055	8602.2	81.318	1.1689	.00874
35	79545	−1255.3	−26.504	.47795	108800	−304.84	−50.228	.39593	119980	−5472.5	−73.299	.32824
	683.55	−26.385	−.51900	.00524	280.33	−50.059	−.75579	.00284	−348.48	−68.656	−.83680	.00148
40	−18193	−1994.8	−40.476	.06824	−47777	−2812.1	−43.096	.01350	−83257	−3325.8	−40.967	−.01574
	5947.9	208.48	7.8453	...	10687	318.40	9.0274	...	16815	442.51	10.068	...
$\phi_2 \rightarrow 20$	390195	5947.9	231.87	1.0000	808130	10687	312.45	1.0000	1420100	16815	393.30	1.0000
	2908.9	45.538	1.4515	.00838	4319.2	45.541	1.1038	.00686	5628.3	38.890	.76911	.00570
25	74898	−970.36	−26.860	.45012	103045	−2263.0	−49.432	.37394	114240	−3998.0	−71.396	.31060
	448.05	−13.109	−.32400	.00333	199.91	−24.930	−.47761	.00181	−195.13	−34.219	−.53126	.00095
30	−16271	−1445.5	−37.351	.06223	−43320	−2033.1	−39.792	.01236	−75972	−2401.1	−37.847	−.01447
	2732.6	57.190	4.0957	...	4993.6	86.637	4.6937	...	7945.5	119.76	5.2217	...
$\phi_2 \rightarrow 10$	360945	2732.6	209.81	1.0000	756950	4993.6	287.56	1.0000	1341250	7945.5	366.04	1.0000
	1269.7	12.982	.67509	.00359	1917.9	12.993	.51848	.00299	2529.5	11.116	.36623	.00251
15	63046	−602.13	−25.682	.37674	88573	−1324.4	−45.211	.31669	100125	−2285.2	−64.354	.26520
	207.75	−3.4634	−.11915	.00139	114.96	−6.9718	−.19032	.00078	−44.887	−9.7761	−.21796	.00042
20	−11896	−798.46	−29.650	.04936	−33222	−1129.9	−31.935	.01046	−59568	−1340.4	−30.616	−.01106

Table 3 Influence coefficients at and near the edge for r/h = 150, 200, and 250

	r/h = 150				r/h = 200				r/h = 250			
	Er^2V	$Er\delta$	rN_θ	M_ϕ	Er^2V	$Er\delta$	rN_θ	M_ϕ	Er^2V	$Er\delta$	rN_θ	M_ϕ
$\phi_1 \rightarrow 90$	74382	−4722.4	−31.483	...	132220	−7270.8	−36.354	...	206585	−10161	−40.646	...
	−2340800	74382	495.88	1.0000	−4805350	132220	661.11	1.0000	−8394700	206585	826.34	1.0000
85	22177	−235.60	−1.5715	−.01580	26665	20.511	.10842	−.01128	27299	343.79	1.3857	−.00819
	−115490	−14677	−98.426	.29830	16424	−27335	−137.39	.20179	289030	−41224	−165.70	.13226
80	−2605.6	275.99	1.8728	−.00157	−5765.4	301.29	1.5319	.00007	−7884.3	266.52	1.0833	.00056
	139870	−6169.5	−41.806	−.03488	202940	−5323.0	−27.023	−.04353	223915	−3107.5	−12.597	−.03813
$\phi_2 \rightarrow 50$	56323	2814.4	24.300	...	100285	4324.5	28.033	...	156860	6035.4	31.321	...
	2314900	56323	490.17	1.0000	4759500	100285	654.57	1.0000	8323350	156860	819.07	1.0000
55	16362	135.33	1.1319	.01166	19718	−23.476	−.11127	.00833	20235	−222.27	−1.0544	.00605
	110470	−12088	−96.811	.28508	−15234	−22208	−134.06	−.19283	−275845	−33255	−161.03	.12630
60	−1820.5	−176.60	−1.3490	.00113	−4075.9	−191.42	−1.1001	−.00005	−5597.2	−168.49	−.77634	−.00040
	−128925	−5060.5	−38.831	−.03264	−187460	−4321.7	−24.959	−.04050	−207150	−2474.2	−11.502	−.03543
$\phi_2 \rightarrow 40$	47005	1993.9	20.450	...	83764	3061.4	23.583	...	131090	4270.2	26.343	...
	2303500	47005	487.51	1.0000	4739400	83764	651.57	1.0000	8292150	131090	815.76	1.0000
45	13521	94.800	.92949	.00963	16313	−19.335	−.09909	.00688	16761	−161.83	−.87902	.00500
	108615	−10415	−95.991	.27972	−14494	−19044	−132.57	.18925	−270230	−28449	−159.02	.12394
50	−1468.9	−128.19	−1.1033	.00092	−3310.5	−138.72	−.89939	−.00004	−4556.2	−121.96	−.63457	−.00033
	−124765	−4351.7	−37.696	−.03172	−181640	−3705.3	−24.195	−.03933	−200900	−2108.4	−11.114	−.03441
$\phi_2 \rightarrow 30$	36240	1217.7	15.975	...	64671	1867.4	18.414	...	101305	2602.7	20.562	...
	2285400	36240	483.19	1.0000	4707700	64671	646.70	1.0000	8243100	101305	810.42	1.0000
35	10278	57.170	.70278	.00731	12426	−13.910	−.08071	.00523	12793	−102.37	−.67452	.00381
	106000	−8401.8	−94.608	.27175	−13170	−15270	−130.20	.18396	−261610	−22739	−155.92	.12050
40	−1075.5	−80.841	−.82535	.00069	−2452.6	−87.356	−.67311	−.00003	−3388.8	−76.725	−.47503	−.00024
	−118820	−3501.0	−36.071	−.03036	−173395	−2970.9	−23.123	−.03763	−192080	−1677.9	−10.584	−.03294
$\phi_2 \rightarrow 20$	24335	579.28	11.009	...	43559	886.61	12.679	...	68368	1234.0	14.150	...
	2249700	24335	474.33	1.0000	4645350	43559	636.78	1.0000	8146900	68368	799.58	1.0000
25	6742.9	26.968	.46214	.00478	8188.0	−7.8832	−.05397	.00343	8466.1	−51.089	−.44520	.00250
	101635	−6086.3	−91.689	.25749	−10285	−10965	−125.59	.17460	−245590	−16256	−150.08	.11446
30	−655.99	−40.308	−.52535	.00045	−1536.1	−43.571	−.42974	−.00001	−2140.8	−38.272	.30389	.00015
	−108865	−2524.3	−33.335	−.02795	−159690	−2134.8	−21.364	−.03475	−177540	−1194.9	−9.7479	−.03047
$\phi_2 \rightarrow 10$	11592	156.16	5.6996	...	20975	237.69	6.5485	...	33157	329.60	7.2967	...
	2137550	11592	445.02	1.0000	4449900	20975	603.95	1.0000	7846300	33157	763.77	1.0000
15	3059.3	7.7442	.22577	.00212	3773.2	−2.1262	−.01179	.00154	3960.3	−14.370	−.19293	.00113
	91409	−3436.8	−82.132	.22119	−1359.9	−6118.6	−111.99	.15126	−202880	−9019.7	−133.68	.09972
20	−237.53	−11.653	−.21903	.00021	−616.30	−12.771	−.18258	...	−886.18	−11.321	−.13075	−.00006
	−865.71	−1413.7	−27.129	−.02215	−129340	−1199.2	−17.539	−.02811	−145640	−668.56	−8.0553	−.02491

Influence Coefficients Due to Uniform Internal Pressure

From equation (34) in the Appendix it can be seen that the differential equations of equilibrium for hemispherical shells subjected to edge bending loads and uniform pressure are homogeneous, i.e., there is no term on the right-hand side involving the pressure. This means that the membrane equations give the stress resultants and deformations due to uniform pressure. Thus, due to uniform internal pressure, the influence coefficients are:

$$\left.\begin{aligned} V &= 0 \\ rN_\phi &= pr^2/2 \\ rN_\theta &= pr^2/2 \\ Er\delta &= pr^2/2\,(r/h)\,(1-\nu)\sin\phi \\ M_\phi &= 0 \\ M_\theta &= 0 \end{aligned}\right\} \tag{7}$$

where

N_ϕ = meridional direct stress resultant (+ when tensile)
M_θ = circumferential bending stress resultant (+ when producing tension on inner surface)
p = uniform internal pressure

and the other symbols are as defined previously.

Effect of Vertical Line Loadings

The influence coefficients given in Tables 1 to 3 are for uniformly distributed bending moments and horizontal shearing forces applied at the edges. The coefficients due to uniform pressure have just been discussed in the preceding section. Another loading case of interest is depicted in Fig. 4(*a*), i.e., uniformly distributed concentrated vertical loads applied around the edges. In this section, one method of solving this problem is given.

The vertical load V at $\phi = \alpha$ may be regarded as being the resultant of two other loadings. One of these, $V \cot \alpha$, is assumed to act horizontally. The other loading, $V/\sin \alpha$, is assumed to act along the tangent at $\phi = \alpha$. It is easily verified that these two loadings have a resultant equal to V acting vertically. The problem shown in Fig. 4 can then be solved if means are available for solving the two partial problems shown in Figs. 4(*b* and *c*).

The problem shown in Fig. 4(*b*) can easily be solved with the aid of Tables 1 to 3. That in Fig. 4(*c*) has the following solution:

$$N_\phi = -N_\theta = -\frac{V \sin \alpha}{\sin^2 \phi} \tag{8}$$

$$Eh\delta = \frac{Vr \sin \alpha}{\sin \phi}(1+\nu) \tag{9}$$

$$V = M_\phi = M_\theta = 0 \tag{10}$$

The fact that V and $dV/d\phi$ are zero, and hence M_ϕ and M_θ, can be checked by inserting the relevant quantities in the following compatibility equation relating the middle surface strains, ϵ_ϕ and ϵ_θ, and the rotation V:

$$V = (\epsilon_\phi - \epsilon_\theta)\cot\phi - r_2/r_1\, d/d\phi(\epsilon_\theta) \tag{11}$$

where

$$\left.\begin{aligned} \epsilon_\phi &= 1/Eh[N_\phi - \nu N_\theta] \\ \epsilon_\theta &= 1/Eh[N_\theta - \nu N_\phi] \\ r_2 &= r_1 = r \text{ for a hemisphere} \end{aligned}\right\} \tag{12}$$

Illustrative Example: Hemisphere-Cylinder Intersection

As an illustration of the use of the influence coefficients the problem of the intersection of a cylinder with a hemisphere will be considered (see Fig. 5). It will be assumed that the opening in the hemisphere subtends an angle of 2α at the center of the hemisphere and the unknown stress resultants at $\phi = \alpha$ will be denoted by:

Q_α = transverse shearing force/unit length
M_α = meridional bending moment/unit length
N_α = meridional direct force/unit length

The following relation between Q_α and N_α also holds:

$$N_\alpha = -Q_\alpha \cot \alpha + \frac{pr}{2} \tag{13}$$

To determine the edge forces acting on the ends of the cylinder N_α and Q_α are resolved horizontally and vertically. Thus,

Horizontally outward: $Q_\alpha \sin \alpha - N_\alpha \cos \alpha$ (14)

$$= Q_\alpha \sin \alpha + Q_\alpha \cos \alpha \cot \alpha - \frac{pr}{2}\cos\alpha \text{ [from equation (13)]}$$

$$= \frac{Q_\alpha}{\sin \alpha} - \frac{pr}{2}\cos\alpha$$

$$= H_\alpha - \frac{pR}{2}\cot\alpha \tag{15}$$

where H_α is the horizontal shearing force.

Vertically upward: $Q_\alpha \cos \alpha + N_\alpha \sin \alpha$ (16)

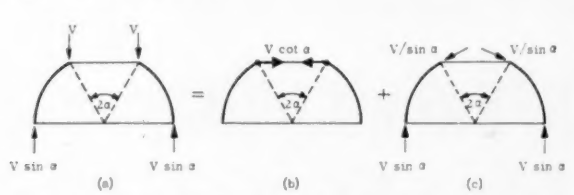

Fig. 4 Resolution of axisymmetric vertical edge loadings into auxiliary loadings

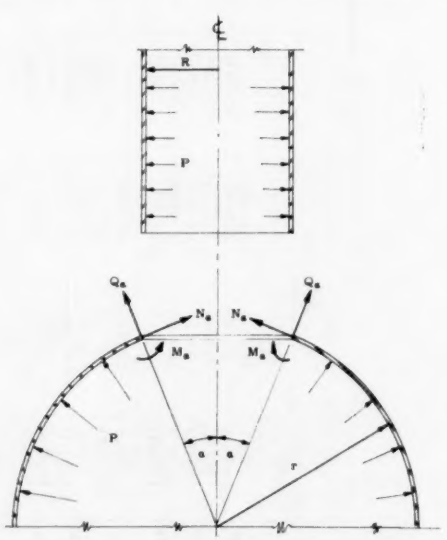

Fig. 5 Hemisphere-cylinder intersection. Edge forces and moments on open-crown hemisphere.

$$= Q_\alpha \cos \alpha - Q_\alpha \cos \alpha + \frac{pr}{2} \sin \alpha \quad \text{[from equation (13)]}$$

$$= \frac{pR}{2} \tag{17}$$

Thus the vertical forces on the cylinder and hemisphere balance each other. A horizontal force of magnitude $H_\alpha - pR/2 \cot \alpha$ has, however, to be applied inward at the cylinder ends to satisfy horizontal force equilibrium requirements. To satisfy moment equilibrium requirements a moment M_α must also be applied to the cylinder ends. The final force system (H_α and M_α still unknown, however) acting on the cylinder and hemisphere is as shown in Fig. 6.

The magnitude of M_α and H_α are determined by demanding that the final displacements and rotations (due to internal pressure and edge bending loads) of both cylinder and open-crown hemisphere be alike.

The edge influence coefficients for a cylinder are (Roark, 1943): Due to uniform internal pressure p:

$$Eh_c\delta_c^{\,p} = \frac{pR^2}{2}(2 - \nu); \quad V_c^{\,p} = 0 \tag{18}$$

Due to uniformly distributed unit shears perpendicular to the axis of symmetry at the end of the cylinder:

$$\delta_c^{\,H} = \frac{1}{2D\beta^3}; \quad V_c^{\,H} = \frac{1}{2D\beta^2} \tag{19}$$

Due to uniformly distributed unit moments at the end of the cylinder:

$$\delta_c^{\,M} = \frac{1}{2D\beta^2}; \quad V_c^{\,M} = \frac{1}{\beta D} \tag{20}$$

where

$$\left.\begin{aligned} R &= \text{mean radius of cylinder} \\ h_c &= \text{thickness of cylinder} \\ \beta^4 &= \frac{3(1-\nu^2)}{R^2h_c^2} \\ D &= \frac{Eh_c^3}{12(1-\nu^2)} \end{aligned}\right\} \tag{21}$$

and the superscripts p, H, and M denote internal pressure, shears, and moments, respectively.

Using these relations the total displacement and rotation of the cylinder at its junction with the hemisphere is given by:

$$\delta_c = \frac{pR^2}{2Eh_c}(2 - \nu) - \left(H_\alpha - \frac{pR}{2}\cot\alpha\right)\frac{1}{2D\beta^3} + \frac{M_\alpha}{2D\beta^2} \tag{22}$$

$$V_c = \left(H_\alpha - \frac{pR}{2}\cot\alpha\right)\frac{1}{2D\beta^2} - \frac{M_\alpha}{\beta D} \tag{23}$$

In these equations δ was taken positive outward and V positive when the tangent rotated counterclockwise on the left.

The displacement and rotation of the open-crown hemisphere due to the H_α and M_α can be obtained from Tables 1 to 3. Thus, relations are obtained of the form (assuming no interaction between the edges of the hemisphere at $\phi = \alpha$ and $\phi = 90$ deg):

$$Er^2V_h = (\ )rH_\alpha + (\ )M_\alpha \tag{24}$$

$$Er\delta_h = (\ )rH_\alpha + (\ )M_\alpha \tag{25}$$

where the parentheses indicate numerical values of the edge influence coefficients and the subscript h denotes the hemisphere at

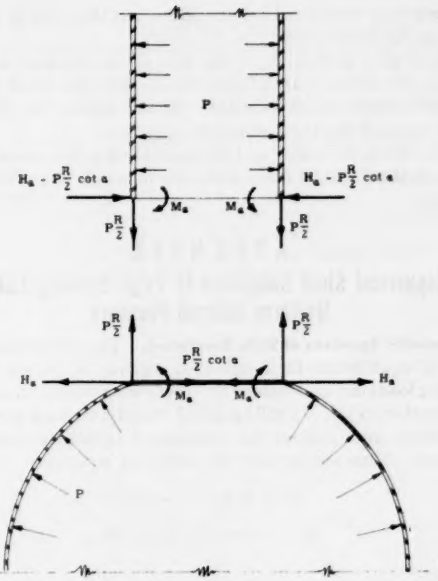

Fig. 6 Shears, forces, and moments acting at cylinder-hemisphere intersection

$\phi = \alpha$. The displacement and rotation of the hemisphere due to uniform internal pressure are obtained from equation (7). Thus the total displacement and rotation of the hemisphere at $\phi = \alpha$ are given by

$$Er^2V_h = (\ )rH_\alpha + (\ )M_\alpha \tag{26}$$

$$Er\delta_h = \frac{pr^2}{2}\left(\frac{r}{h}\right)(1 - \nu)\sin\alpha + (\ )rH_\alpha + (\ )M_\alpha \tag{27}$$

As the cylinder and hemisphere must eventually fit together at their common junction, the following compatibility equations must be satisfied:

$$\left.\begin{aligned} \delta_c &= \delta_h \\ V_c &= V_h \end{aligned}\right\} \tag{28}$$

From equations (22), (23), (26), (27), and (28) two simultaneous equations for H_α and M_α are obtained. Having solved these equations it is then a simple matter to obtain the stress distribution in the vicinity of the edge of the hemisphere by using the influence coefficients given in Tables 1 to 3. The stress distribution throughout the cylinder can also easily be found using the tables given in Timoshenko.

Discussion of the Differential Equations Used in the Analysis. The differential equations used to calculate the influence coefficients, i.e., equation (35) is based on classical small-deflection theory. The assumptions made in that theory and its limitations should be remembered when using the influence coefficients. In particular, the following points should be checked at the end of an analysis:

(*a*) That the shell deflections are small in comparison to the shell thickness.

(*b*) That no portions of the shell are inelastic.

(*c*) That the direct forces N_θ and N_ϕ are small in comparison with their critical compressive values.

For thick shells, i.e., those in which the shell thickness is not small in comparison to the principal radii of curvature, it is probable that shear deformations are important. These latter

have not been considered herein. However, they will be investigated in the near future.

With regard to item (*b*), if the final stress distribution in the shell should be substantially inelastic, then the limit load of the shell should be investigated. In this connection, the work of Drucker and Shield [2] should be of value.

Creep effects have also not been considered in the present work, although there will be many instances in which they will be important.

APPENDIX

Hemispherical Shell Subjected to Edge Bending Loads and Uniform Internal Pressure

Differential Equations of Static Equilibrium. The differential equations of equilibrium for a spherical segment subjected to edge bending loads can be obtained by specializing the equations given in Timoshenko [8]. It will be found that if a uniform pressure is also taken into account the differential equations remain unchanged. Thus one obtains the following equations:

$$L(U) + \nu/r\, U = EhV \tag{29}$$

$$L(V) - \nu/r\, V = -U/D \tag{30}$$

where

U = rQ_ϕ
Q_ϕ = transverse shearing force/unit length
V = angle of rotation of a tangent to a meridian
D = flexural rigidity of the shell = $Eh^3/12(1 - \nu^2)$ (31)
E = Young's modulus
h = thickness of the hemisphere
r = radius of the hemisphere
ν = Poisson's ratio

and

$$L(\ldots) = 1/r[(\ldots)'' + \cot\phi(\ldots)' - \cot^2\phi(\ldots)]$$

and the primes denote differentiation with respect to the colatitude angle ϕ.

Introducing now the dependent variable Z defined by

$$Z = U + kV \tag{32}$$

where

$$k = -D/r(\nu \pm i\mu^2 r)$$
$$\mu^2 r = [12(1 - \nu^2)(r/h)^2 - \nu^2]^{1/2} \tag{33}$$

the two equations (29) and (30) can be reduced to the following single complex, second-order, ordinary linear differential equation:

$$L(Z) \mp i\mu^2 Z = 0 \tag{34}$$

where

$$i = \sqrt{-1}$$

The minus sign in equation (34) is obtained if the positive sign is taken for k in equation (33), and vice versa.

If the two linearly independent solutions of

$$L(Z) - i\mu^2 Z = 0 \tag{35}$$

are

$$Z_1 = x_1 + iy_1$$
$$Z_2 = x_2 + iy_2 \tag{36}$$

then it can be shown (Burrows [1], Galletly [4]) that the solutions for U and V (where $Z = U + kV$) may be written as:

$$U = Ax_1 + By_1 + Cx_2 + Dy_2 \tag{37}$$

$$EhrV = A(\nu x_1 - \mu^2 r y_1) + B(\nu y_1 + \mu^2 r x_1) + C(\nu x_2 - \mu^2 r y_2) + D(\nu y_2 + \mu^2 r x_2) \tag{38}$$

Knowing U and V the stress resultants can be found from the relations:

$$\left.\begin{aligned} N_\phi &= -U\cot\phi/r + pr/2 \\ N_\theta &= -U'/r + pr/2 \\ M_\phi &= -D/r(V' + \nu V\cot\phi) \\ M_\theta &= -D/r\,(V\cot\phi + \nu V') \\ Q_\phi &= U/r \\ H_\phi &= Q_\phi/\sin\phi \end{aligned}\right\} \tag{39}$$

where

N_ϕ = meridional direct stress resultant (+ when tensile)[3]
N_θ = circumferential direct stress resultant (+ when tensile)
M_ϕ = meridional bending stress resultant (+ when producing tension on inner surface)
M_θ = circumferential bending stress resultant (+ when producing tension on inner surface)
Q_ϕ = transverse shearing force (+ when directed toward the center of the hemisphere for the larger value of ϕ)
H_ϕ = horizontal shearing force (+ in the same sense as Q_ϕ). With no load acting on the shell, the relation $N_\phi = -Q_\phi\cot\phi$ holds. H_ϕ is the horizontal resultant of N_ϕ and Q_ϕ. The vertical resultant is, of course, zero.

The horizontal displacement of a point on the shell δ (+ outward) can be found from the relation:

$$Eh\delta = r\sin\phi(N_\theta - \nu N_\phi) \tag{40}$$

Solution of the Differential Equations of Equilibrium. Equation (35) is a linear, complex, homogeneous, ordinary differential equation of the second order. As the equation is complex the complete solution will contain [as shown by equation (37)] four linearly independent solutions. These solutions were obtained by substituting $Z = x + iy$ in equation (35) and equating real and imaginary parts. One obtains:

$$\left.\begin{aligned} x'' &= -x'\cot\phi + x\cot^2\phi - \mu^2 ry \\ y'' &= -y'\cot\phi + y\cot^2\phi + \mu^2 rx \end{aligned}\right\} \tag{41}$$

By substituting

$$\left.\begin{aligned} x' &= u_1, \quad x = u_2 \\ y' &= u_3, \quad y = u_4 \end{aligned}\right\} \tag{42}$$

the two second-order equations (42) can be reduced to the following four simultaneous first-order differential equations:

$$\left.\begin{aligned} u_1' &= -u_1\cot\phi + u_2\cot^2\phi - \mu^2 r u_4 \\ u_2' &= u_1 \\ u_3' &= -u_3\cot\phi + u_4\cot^2\phi + \mu^2 r u_2 \\ u_4' &= u_3 \end{aligned}\right\} \tag{43}$$

The four equations (43) were integrated on a high-speed digital computer using the Runge-Kutta integration method. The step length used was $1/2$ degree. The integration process was commenced at $\phi = 90$ deg using the following initial values:

	x	x'	y	y'
1st solution	1	0	0	0
2nd solution	0	1	0	0

[3] The N's, M's, H's, etc., are per unit length.

As the shell has two edges the problem is really a two-point boundary value problem. However, as the differential equations are linear, it is only necessary to assign initial values at one point (Milne, [5]).

Once the numerical solutions have been obtained, the influence coefficients are determined by using equations (37) to (40).

References

1 W. R. Burrows, "Pressure Vessel Heads Under Internal Pressure. Part I—General Considerations," Pressure Vessel Research Committee, New York, N. Y., Design Division Paper, 1950.

2 D. C. Drucker and R. T. Shield, "Limit Analysis of Symmetrically Loaded Thin Shells of Revolution," Division of Applied Mathematics, Brown University, Providence, R. I., Tech. Rept. No. 25, 1957.

3 G. D. Galletly, "Influence Coefficients for Hemispherical Shells With Small Openings at the Vertex," *Journal of Applied Mechanics*, vol. 22, TRANS. ASME, vol. 77, 1955, p. 20.

4 G. D. Galletly, "Torispherical Shells—A Caution to Designers," *Journal of Engineering for Industry*, TRANS. ASME, series B, vol. 81, 1959, p. 51.

5 W. E. Milne, "Numerical Solutions of Differential Equations," John Wiley & Sons, Inc., New York, N. Y., 1953.

6 A. E. H. Love, "The Mathematical Theory of Elasticity," Dover Publications, New York, N. Y., 1944.

7 R. J. Roark, "Formulas for Stress and Strain," McGraw-Hill Book Company, Inc., New York, N. Y., 1943.

8 S. Timoshenko, "Theory of Plates and Shells," McGraw-Hill Book Company, Inc., New York, N. Y., 1940.

ERRATA

Journal of Engineering for Power, Trans. ASME, series A, vol. 81, July, 1959

Three errors have been brought to our attention by Escher Wyss Ltd. They occur in the special issue on gas turbines. They are as follows:

Page 321, Table 9 Gas turbines in naval propulsion applications. The manufacturer of JN 10, 10,000 hp should be Mitsui (not Escher Wyss).

Page 322, paragraph entitled 10,000-shp Prototype Closed-Cycle Plant. The first sentence should read: "A closed-cycle propulsion plant, utilizing air as the working fluid, is under construction by Mitsui" (not Escher Wyss).

Page 326, Table 13 Characteristics of marine gas turbines installed or building. The manufacturer of EW JN 10, 10,000 hp should be Mitsui (not Mitsubishi).

Journal of ENGINEERING FOR POWER

Information for Authors

• Manuscripts should be submitted in final form to the Editor. Each manuscript must be accompanied by a statement that it has not been published elsewhere nor has it been submitted for publication elsewhere. A paper which would occupy more than 8 pages of the Journal may be returned to the author for abridgment.

• The author should state his business connection, the title of his position, and his mailing address. A short abstract (50 to 100 words) should be included on the first page immediately preceding the introductory paragraph of the paper.

Three copies of the manuscript are required. One of these must be a carefully prepared printer's copy, typed in double spacing, on one side of the page only, with wide margins, on $8^1/_2$ by 11-in. opaque white paper. Mimeographed manuscripts, if prepared with exceptional care, can be accepted provided they are completely edited.

• As far as possible, all mathematical expressions should be typewritten. Greek letters and other symbols not available on the typewriter should be carefully inserted in ink. Care should be taken to distinguish between capital and lowercase letter, between zero (0) and the letter (*O*), between the numeral (1) and the letter (*l*), etc. A letter representing a vector cannot be printed with an arrow above or below it. The letter should be underscored with a single wavy line, wherever it appears in the text, to designate boldface type.

• A list of symbols carefully marked for the use of the editor (thus: κ, Greek l.c. kappa), if it has not been included in the body of the paper, should accompany the manuscript on a separate page.

• Before preparing a manuscript the author should study printed articles in the Journal, with special attention to the form and style of mathematical expressions, tables, footnotes, references, and abstract. Numbers that identify mathematical expressions should be enclosed in parentheses. Numbers that identify references at the end of the paper should be enclosed in brackets. Care should be taken to arrange all tables and mathematical expressions in such a way that they will fit into a single column when set in type. Equations that might extend beyond the width of one column (fractions that should not be broken or long expressions enclosed in parentheses) should be rephrased to go on two or more lines within column width. Fractional powers are preferred to root signs and should always be used in more elaborate formulas. The solidus should be used instead of the horizontal line for fractions wherever possible.

• A normal paper should not exceed 8 pages in the Journal. It is about 8000 words or 20 double-spaced typewritten pages exclusive of drawings. A Technical Brief should not exceed 750 words or about one page in the Journal inclusive of drawings.

• Originals and two copies of figures must accompany the manuscript. Line drawings should not be larger than $8^1/_2 \times 11$ in. and should be planned for reduction to column width. Lettering should be large enough to be clearly legible when the illustration is reduced. The originals of line drawings must be in India ink on white or pale blue tracing paper or tracing cloth. Photographs of equipment or test specimens must be glossy prints and should be used sparingly. Captions for figures should be typed double-spaced and included as the last page of the manuscript. The figure number and author's name should be written in the margin or on the back of each illustration.

• Titles of papers should be brief.

• Authors can obtain copies of the ASME Manual MS-4, "An ASME Paper," from the Editor and are urged to do so before drafting their papers in final form.

• Papers published in Journals of the Transactions of the ASME must be presented at a Meeting, either in person or by title.

• An author is entitled to 25 preprints free of charge (in the case of two authors, 15 each; three or more authors, 10 each). Larger quantities of preprints or reprints can be ordered from Editorial Department, The American Society of Mechanical Engineers, 29 West 39th Street, New York 18, N. Y. Quotations will be sent on request.

Please address all communications to:

Editor, ASME,

29 West 39th Street,

New York 18, N. Y.

ASME Publications Committee